

https://dspace.org/

Structural, electrical and electronic properties of diamond like carbon (DLC) and carbon-based materials

Mpingi, Wilfred Mbiombi

2014-03-05
http://hdl.handle.net10539/14032

Downloaded from a DSpace repository. https://dspace.org/

Structural, Electrical and Electronic Properties of Diamond like Carbon (DLC) and Carbon-Based Materials

Wilfred Mbiombi Mpingi

A dissertation submitted to the Faculty of Science, University of the Witwatersrand, Johannesburg, in fulfilment to the requirements of the degree of Master of Science.

Johannesburg 2013

DECLARATION

I declare that this dissertation is my own unaided work except where I have explicitly indicated otherwise. It is being submitted for the degree of Master of Science at the University of the Witwatersrand, Johannesburg. It has not been submitted before for any degree or examination in any other University.

Signed

_____

Date

_____

ABSTRACT

In this work, we have used the diamond-like carbon (DLC) also known as hydrogenated amorphous carbon (a-C:H), silicon doped DLC (a-C:H:Si) thin films deposited by the plasma enhanced chemical vapour deposition (PECVD) process on silicon substrate and studied their structural, electrical and electronic properties. The DLCs films were prepared at different applied bias voltage (V_b) starting from 100V to 600V; whereas the silicon is doped with DLC thin films using tetramethysilane (TMS) as a precursor at different standard centimetre cube per minute (sccm). In addition nitrogen doped amorphous carbon (a-C:N_x) thin films prepared by pulsed laser deposition (PLD) process and studied their different properties. Different nitrogen concentration (at.%) of a-C:N_x thin films were deposited on silicon substrate using nitrogen-gas as a precursor. The thicknesses of all thin films were ~150±15 nm controlled and monitored during deposition process. Raman spectroscopy of these thin films was measured by using two different laser excitation wavelengths *viz* 488 nm and 647 nm respectively. The microstructure and electronic properties of these samples were investigated by Raman spectroscopy and the electrical property was studied by current-voltage (I-V) characteristics. Finally, a correlation among the electrical properties, electronic properties and micro-structure properties were established based on their sp^3 and sp^2 concentration in the thin film structure.

Dedicated to my parents philippe Kimyinpu and Nelly Bilela, and my wife Ikonzo Madangi Mathy, and children Kerene, Tigo and Elada for their love, patience, emotional and spiritual support. I love you all.

ACKNOWLEDGMENTS

My deepest gratitude goes to my supervisor Professor Sekhar Chandra Ray for his guidance and support and for all the knowledge I have gained from him. Thank you very much. I am also very grateful to Dr Zivayi Chiguvare for his support and caring advice during the course of my studies. I am also deeply grateful to Rudolph Erasmus for helping me get the Raman data as well as for insightful discussions on several aspects of my work.

I would like to thank and acknowledge the former and the new head school of physics Prof Joao Rodrigues and Prof John Carter for supporting me to do my masters. All technicians of School of Physics for their daily help support and good mood. I thank to Emmanuel nshingabigwi for his assistance and advice in writing the present thesis. Dr Zivayi Chiguvare is thanked again for helping me to get I-V characteristic data in the laboratory at School of Physics. I would also like to thank our collaborators for providing us all the samples.

I am also deeply grateful to the DST/NRF Centre of Excellence in Strong Materials and School of Physics for the financial support without which my work at WITS might not have been so smooth. Thank you very much. I would also like to thank my friends and fellow postgraduate students for making my stay at WITS a memorable one.

I thank God, who is a provider by his grace and mercy, makes all things possible.

TABLE OF CONTENTS

DECLARATION 2
ABSTRACT 3
ACKNOWLEDGMENTS 5
TABLE OF CONTENTS 6
LIST OF FIGURES 9

Chapter 1 15
1. Introduction 15
1.1 Diamond like carbon 15
1.2 Objectives of the present study 18

Chapter 2 19
Literature Review 19
2.1 General Review 19
2.2 Deposition methods 21
2.2.1 Ion Beam Deposition Methods 23
2.2.2 Sputtering Process 24
2.2.3 Cathodic vacuum arc System 24
2.2.4 Plasma Enhance Chemical Vapour Deposition Methods (PECVD) 25
2.2.5 Pulsed laser deposition (PLD) process 28
2.3 Deposition Mechanism 28
2.3.1 Hydrogenated amorphous carbon (a-C: H) 30
2.4. Atomic structure and characterisation 33
2.4.1. Bonding configuration 33
2.4.2 Raman spectroscopy 34
2.4.3 Hydrogen content 37
2.5 Electronic structure 38
2.5.1 The σ and π states 38

2.5.2 Cluster model 38
2.5.3 Network calculations 39
2.5.4 Optical gap 41
2.6 The Doping of DLC 43
2.7 Electrical properties 44
2.8. Mechanical property of DLC 45
2.8.1. Elastic properties 46

Chapter 3 47
Experimental Details 47
3.1. Raman Experimental Arrangement 47
3.1.1 Introduction 47
3.1.2 Experimental Apparatus 47
3.1.2.1 The Laser 47
3.1.2.2 The Raman Spectrograph 50
3.2 I-V characteristics of DLC films by 4140B p.A Meter/DC voltage Source. 52
3.2.1 Description of the instrument 52
3.2.2 Measurement of I-V Characteristics 54

Chapter 4 55
Results and Discussion 55
4.1 Introduction 55
4.1.1 Raman spectroscopy of diamond like carbon (DLC) 56
4.1.2 Raman spectroscopy of Silicon doped Diamond Like Carbon (DLC:Si) 69
4.1.3 Nitrogen Doped amorphous carbon (a-CNx) 77
4.2 Electrical properties of diamond like carbon (DLC) and amorphous carbon (a-C) films... 85
4.2.1 Voltage-Current (V-I) relationships of Diamond like carbon (DLC) thin films 85
4.2.2. I-V Characteristic of Silicon doped DLC (DLC:Si) 88
4.2.3 I-V characteristic of nitrogen doped amorphous carbon (a-CNx) films. 91

Chapter 5 95
Conclusion and proposed future work 95
REFERENCES 97

LIST OF FIGURES

Figure 2.1 Ternary phase diagram of bonding in amorphous carbon-hydrogen alloys 22

Figure 2.2 Schematics of various deposition systems for DLC 23

Figure 2.3 Component processes in the growth mechanism of a-C:H 32

Figure 2.4 Schematic DOS of a carbon showing σ and π states 35

Figure 3.1 A transition schemes for an Ar^+ laser. The first collision ionises the neutral argon and the next pumps it to an excited state (from the Operational Manual for the Spectra Physics 2020/2025 Ion Laser). 49

Figure 3.2 *Schematic diagram of a gas laser* 50

Figure 3.3 Schematic diagram of the Raman Spectrograph showing the beam trajectory. (From the Instruction Manual for the Jobin-Yvon T64000 Raman spectrograph) 52

Figure 3.4 Mode l4140B and supplied Accessories (From manual HP4140B p.A. Meter/D.C Voltage Source) 54

Figure 4.1.1.1 Raman Spectra of DLC films deposited at different bias voltage [LASER excitation wavelength λ_{exc} = 488 nm] 58

Figure 4.1.1.2 Deconvoluted into D-Peak and G-peak of Raman Spectra of DLC films deposited at different bias voltage: (a) 100 V, (b) 300 V, (c) 400 V and (d) 600 V [λ_{exc}= 488 nm] 59

Figure 4.1.1.3 Raman Spectra of DLC films deposited at different bias voltage [λ_{exc}=647 nm] 62

Figure 4.1.1.4 Deconvoluted into D-Peak and G-peak of Raman Spectra of DLC films deposited at different bias voltage: (a) 100 V, (b) 300 V, (c) 400 V and (d) 600 V [λ_{exc}= 647 nm] 63

Figure 4.1.1.5 Variation of the Raman $I_{(D)}/I_{(G)}$ ratio of DLC thin films with sp^3-content at LASER excitation wavelength λ_{exc} = 488 nm 64

Figure 4.1.1.6 Variation of G-peak position shift of DLC thin films with sp^3-content at LASER excitation wavelength λ_{exc} = 488 nm 64

Figure 4.1.1.7 Variation of $I(_D)/I(_G)$ ratio of DLC thin films with optical gap 65

Figure 4.1.1.8 Variation of Tauc gap of DLC thin films with sp^2-fraction 66

Figure 4.1.1.9 sp^3 fractions in function of density for different simulations of a-C networks. 67

Figure 4.1.1.10 sp^3 fractions in function of stress for different ta-C and a-C:H films. 68

Figure 4.1.2.1 Raman Spectra of silicon doped DLC (DLC:Si) films deposited at different TMS flow rate with bias voltage 400 V [LASER excitation wavelength λ_{exc} = 488 nm] 69

Figure 4.1.2.2 Deconvoluted into D-Peak and G-peak of Raman Spectra of DLC:Si films deposited at constant bias voltage (V_B= 400 V) and at different TMS flow rate (a) 5 sccm, (b) 20 sccm, (c) 30 sccm and (d) 40 sccm [λ_{exc}= 488nm] 70

Figure 4.1.2.3 Raman Spectra of silicon doped DLC (DLC:Si) films deposited at different TMS flow rate with bias voltage 400 V [λ_{exc} = 647 nm] 72

Figure 4.1.2.4 Deconvoluted into D-Peak and G-peak of Raman Spectra of DLC:Si films deposited at constant bias voltage (V_B= 400 V) and at different TMS flow rate (a) 5 sccm, (b) 20 sccm, (c) 30 sccm and (d) 40 sccm [λ_{exc}= 647 nm] 73

Fig. 4.1.2.5 (I_D/I_G) ratio (obtained from the D-Peak and G-peak area) with tetramethysilane (TMS) flow rate with excitation Laser wavelength λ_{exc} = 488 nm and λ_{exc} = 647 nm 75

Fig. 4.1.3.1 Raman spectra of different at% N-doped amorphous carbon (a-CNx) obtained at the LASER excitation wavelength λ_{exc} = 488 nm 77

Figure 4.1.3.2 Deconvoluted into D-Peak and G-peak of Raman Spectra of a-CN_x films deposited at different nitrogen concentration (at %) (a) 0at%, (b) 4 at%, (c) 9 at% and (d) 14 at% [λ_{exc}= 488 nm] 78

Fig. 4.1.3.3 Raman spectra of different at% N-doped amorphous carbon (a-CNx) obtained at the LASER excitation wavelength λ = 647nm 81

Figure 4.1.3.4 Deconvoluted into D-Peak and G-peak of Raman Spectra of a-CN_x films deposited at different nitrogen concentration (at %) (a) 0 at%, (b) 4 at %, (c) 9 at % and (d) 14 at % [λ_{exc}= 647 nm] 82

Fig. 4.1.3.5 (I_D/I_G) ratio (obtained from the D-Peak and G-peak area) with nitrogen concentration (at %) with excitation Laser wavelength λ_{exc} = 488 nm and λ_{exc} = 647 nm 83

Fig.4.2.1.1 I-V characteristics of Au/DLC/Au structure for various bias voltage deposited DLC thin films (V vs I) 85

Fig.4.2.1.2 I-V characteristics of Au/DLC/Au structure for various bias voltage deposited DLC thin films (V vs I) 85

Fig.4.2.1.3 I-V characteristics of Au/DLC/Au structure for various bias voltage deposited DLC thin films [(V) vs ln (I)] 86

Fig.4.2.1.4 I-V characteristics of Au/DLC/Au structure for various bias voltage deposited DLC thin films [ln(V) vs ln (I)] 88

Fig.4.2.2.1 I-V characteristics of Au/DLC/Au structure for various bias voltage deposited DLC:Si thin films (V vs I) 88

Fig.4.2.2.2 I-V characteristics of Au/DLC/Au structure for various bias voltage deposited DLC:Si thin films (V vs I) 88

Fig.4.2.2.3 I-V characteristics of Au/DLC/Au structure for various bias voltage deposited DLC:Si thin films [(V) vs ln (I)] 89

Fig.4.2.2.4 I-V characteristics of Au/DLC/Au structure for various bias voltage deposited DLC:Si thin films [ln(V) vs ln (I)] 89

Fig.4.2.3.1 I-V characteristics of Au/DLC/Au structure for various bias voltage deposited DLC:Si thin films (V vs I) 91

Fig.4.2.3.2 I-V characteristics of Au/DLC/Au structure for various bias voltage deposited DLC:Si thin films [(V) vs ln(I)] 92

Fig.4.2.3.3 I-V characteristics of Au/DLC/Au structure for various bias voltage deposited DLC:Si thin films [(V) vs ln(I)] 92

Page

List of tables

Table 1 (a) DLC films deposited at different bias voltage (V_B) and (b) DLC films deposited at different TMS flow rate at constant bias voltage (400 V). [C_2H_2=20 sccm, Ar^+=10 sccm)] 57

Table 2 Results obtained after deconvolution into two Gaussian peaks *viz* D-peak and G-peak using a LASER excitation energy of wavelength (λ_{ex}) = 488 nm 60

Table 3: Results obtained after decomposition into two Gaussian peaks *viz* D-peak and G-peak when LASER excitation energy of wavelength (λ_{ex}) = 647 nm 63

Table.4 Different parameters of DLC thin films obtained from the Raman spectra when excitation LASER wavelength λ_{ex} = 488 nm. 68

Table 5: Results obtained after decomposition Raman spectra of DLC:Si films into D-peak and G-peak when LASER excitation energy of wavelength (λ_{ex}) = 488 nm. 71

Table 6: Results obtained after decomposition Raman spectra of DLC:Si films into D-peak and G-peak when LASER excitation energy of wavelength (λ_{ex}) = 647 nm. 74

Table 7: Raman band Parameters obtained after deconvolution of Raman spectra of nitrogenated amorphous carbon films at different N-at% when excitation wavelength is λ_{ex}= 488nm. 80

Table 8: Raman band Parameters obtained after deconvolution of Raman spectra of nitrogenated amorphous carbon films at different N-at% when excitation wavelength is λ_{ex}= 647 nm. 81

Nomenclature

a-C:H-N: hydrogenated nitride amorphous carbon

a-C:H-F: hydrogenated flowrinated amorphous carbon

CH_2: Olefinic

CH_4: methane

C_2H_2: ethyne (acetylene)

C_2H_4: ethene

C_6H_6: benzene

C_3H_8: propane

D.C: direct current

IR: infra-red

rf : radio frequency

SCCM: standard centimetre cubic per minute.

Si-C:H: hydrogenated silicon carbon

RDF: radius distribution function

Chapter 1

1. Introduction

Carbon is a chemical element having chemical symbol **C**. This element is the sixth in the periodic table with atomic mass number twelve. A huge variety of crystalline and disordered structures such as diamond, graphene, amorphous carbon, fullerene and graphite have been attributed to the three hybridizations, namely sp^2,sp^3 and sp^1 of carbon[1]. Diamond consists of carbon atoms with four valence electrons forming in sp^3 a tetrahedral with. neighboring carbon atoms. This hybridization forms the strong σ-bond. The three valence electrons of graphite lie in sp^2 orbitals which forms σ-bonds in a plane while the fourth electron sp^2 lies perpendicular to the σ-bond in the p_π orbital plane. This π orbital forms a weaker π bond with a π orbital on one or more neighboring atoms. Carbon composed by four sp^1 valence electrons, two of the four valence electrons form σ-orbitals, each σ-bonds directed following the X axis and the other two electrons form π bonds in the Y and Z directions [1].

1.1 Diamond like carbon

Diamond-like carbon (DLC) films are similar to diamond with a high fraction of sp^3 hybridized carbon atoms. They can also contain a large amount of hydrogen depending on the deposition conditions. These films are classified among the amorphous carbon that can contain diamond crystallites. These materials do not qualify to be called diamond except if it is proven in three-dimensional crystalline lattice of diamond. Diamond-like films with free hydrogen content can be prepared by variety of technique that are: carbon ion beam deposition, ion - assisted sputtering from graphite or by laser ablation of graphite. Diamond-like Carbon films with high

content of hydrogen are prepared by chemical vapor deposition. The hydrogen content is often more than 25 atomic %. The deposition variables used to prepare the samples are (low) total pressure, hydrogen partial pressure, nature of the precursor and plasma ionization. Radio frequency, microwaves or Ar ions are those activating the plasma. [2]. DLC has some wonderful properties comparative to diamond. These are : - high hardness (~ 20-80 GPa), - high elastic modulus (~200-800 GPa) and - chemical inertness. In addition, it has found widespread commercial applications, such as elastic modulus due to their - low friction coefficients, - high wear resistance, - chemical inertness, - a relatively high optical gap, and - high electrical resistivity. Besides the low capital intensive DLC production methods enhance its scope and yet enabling a hardness benchmarch close to that of diamond feasibility to numerous applications. The ratio of sp^3 to sp^2 bonding is determined by the methods of deposition if the sp^3 bonds fraction reaches a high level (more than 90%), then DLC is called as tetrahedral amorphous carbon (ta-C). Among the different deposition processes / techniques the plasma enhanced chemical vapor deposition (PECVD) is prominently used to produce a-C:H (DLC) contain sp^3 bonding with lesser hydrogen content. Thus high plasma density (PECVD) reactors are used to produce DLC with more sp^3 bonds and less hydrogen content [3].

In this work, we have studied DLC (a-C:H) and silicon doped DLC (a-C:H:Si) films grown by PECVD process. DLC thin films were prepared at different applied bias voltage (V_b) starting from 100V to 600V, in step of 100 Volts the silicon doped DLC were prepared using tetramethysilane (TMS) as a precursor at different flow rates (sccm), with thicknesses of 150 nm on Silicon (004) [4]. We have also studied a-C and nitrogen doped (N: 9-17 at.%) a-C (a-CN_x) with thickness ~50-105 nm. Both N-doped and undoped a-C films were prepared by the pulsed

laser deposition process on Silicon substrate . However, different properties of these films have already been studied [5].

The samples prepared at different voltages (V_b), the chamber was full of Ar ion atmosphere and using an acethylene (C_2H_2) vapour precursor in an argon ion. The augmentation of V_b was followed by increasing and decreasing the contents of sp^3 and sp^2 bond carbon atoms respectively [6]. The C K-edge XANES,VB-PES and Fourier transform infrared (FTIR) spectra will be proposed to study the electronic structure, mechanical properties and bonding structure of silicon doped a-C:H(Si) thin films [7]. X-ray absorption near-edge structure (XANES) and valence-band photoelectron spectroscopy (PES) will be also proposed to investigate the electronic properties of amorphous carbon nitride [8].

In this present work, we have used all the above samples to investigate the microstructure and electronic properties using Raman spectroscopy measurements, based on the sp^3 and sp^2 content present in the thin film structure. The correlation of the Raman spectroscopy measurement with the electrical properties of DLC thin films. Microstructure and electronic characteristics have been studied by using Raman spectroscopy with the help of two different laser excitation energies namely 488 nm and 647 nm. The electrical properties have studied by the I-V characteristic data obtained from the 4140B p.A Meter/DC Voltage Source The main objectives of this present work are listed below:

1.2 Objectives of the present study

This work investigates the electronic, electrical and structural properties of under various deposition condition and doping processes.

The objectives of the present research are itemized as follows:

(i) to investigate the electronic and microstructure of DLC thin films

(ii) to study the electrical properties

(iii) to probe the mechanical properties

(iv) these properties are greatly influence by microstructure thus there is a correlation between electrical, mechanical properties and electronic or microstructure properties of these samples.

Chapter 2

Literature Review

2.1 General Review

The second part of the last century has seen an extensive and intensive research interests on diamond and diamond-like carbon (DLC) structures. In this situation, the revolution in the applications of diamond began when synthetic diamond was produced [9-11]. Due to its extreme hardness, both natural and synthetic diamonds were used first as a cutting tool and at abrasive materials. Since then, the commercial interest on Chemical Vapour Deposited (CVD) diamond films has been driven by its potential application in electronics, coatings, optics and acoustics [12].

In 1971 Aisenberg and Chabot [13] established that the ion beam method can be used for the synthesis of thin carbonaceous films also called diamond-like carbon as some of the film properties resembled of those of diamond. From that time, many methods were reported for the synthesized thin DLC films [14-16]. It has been shown that, it is possible to produce DLC thin films having high hardness [17], good thermal conductivity [12], low thermal expansion, low coefficient of friction and high chemical stability and resistance [18]. Further more highly transparent DLC films suitable transmission could be synthesized by infrared [12]. For its

physical properties, DLC thin films were considered as material, which may be applied for some kind of both passive and active electronics elements.

The term "*diamond-like*" is frequently applied to many sort of non crystalline or amorphous carbonaceous films. DLC consists not only of the amorphous carbons (a-C) but also of hydrogenated alloys ,a-C:H. Later also known as hydrogenated amorphous carbon. Using the ternary phase diagram of Fig.2.1 the various compositions of amorphous C:H alloys on a ternary can be displayed. these forms appear in the right hand which is characterised by interconnecting C-C networks [19]. Deposition methods have been improved to generate a-Cs with rising degrees of sp^3 bonding. In this regard thin films deposition ranges from sp^2 bonding to some way towards sp^3 bonding. If the fraction of sp^3-bonding exceeds 70 % of sp^3 bonding carbon is termed as tetrahedral amorphous carbon (ta-C) and their properties entirely differ from those a-C [20]. A range of deposition methods, such as plasma enhanced chemical vapour deposition (PECVD) [21], have been used to prepare ta-Cs. It is seen from Fig.2.1 that the fraction of sp^3 bonding of carbon material is obvious not so large, and its hydrogen fraction is rather wide. Thus, a more sp^3-bonded material with less hydrogen which can be generated by high plasma density (PECVD) reactors is called hydrogenated tetrahedral amorphous carbon (ta-C:H) [22]. The properties of carbon based materials could be improved through doping by silicon (Si), nitrogen (N), different metal atoms (Fe, Co, Ni,---) and fluorine (F). The resulting materials are denoted as Si-C:H, a-C:H-N, Me-C:H and a-C:H-F.

The principal structural difference between the diamond (natural or synthetic) and the diamond-like systems is the presence and the amount(sometime up to 60 %) of sp^2 bonding The relation between the amount of graphitic sp^2 and aliphatic sp^3 bonding is one of the most important features of DLC, which influences the physical properties of DLC films [23-27].

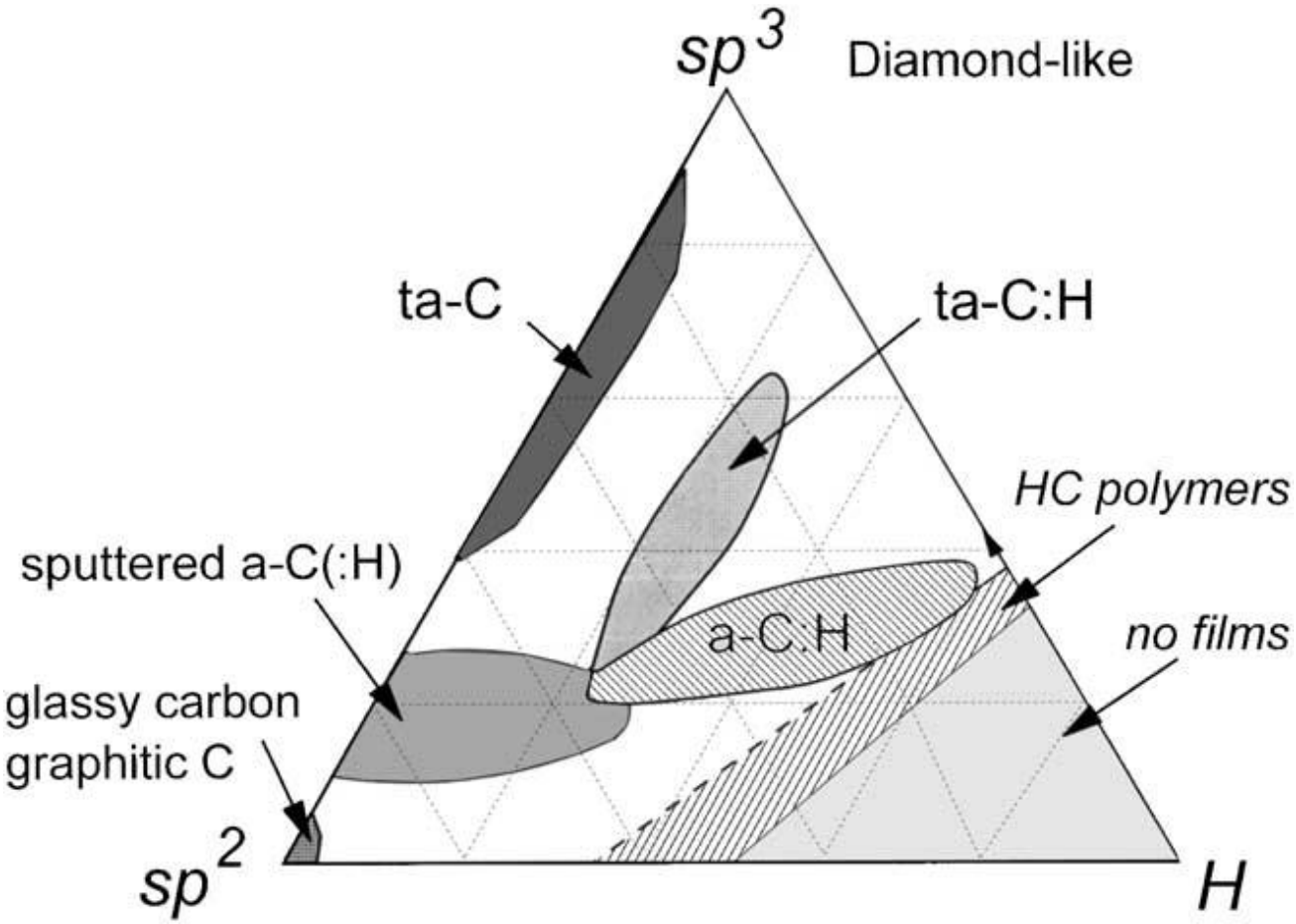

Fig. 2.1 Ternary phase diagram of bonding in amorphous carbon-hydrogen alloys [19]

2.2 Deposition methods

A large number of processes are available [28-33] for the deposition of DLC films, which rely on the lower density of sp^2 relative to sp^3 bonds. So the application of pressure, impact, or some combination of these at the atomic scale can force sp^2 bonded carbon atoms closer together leading to the formation of the sp^3 bonds.

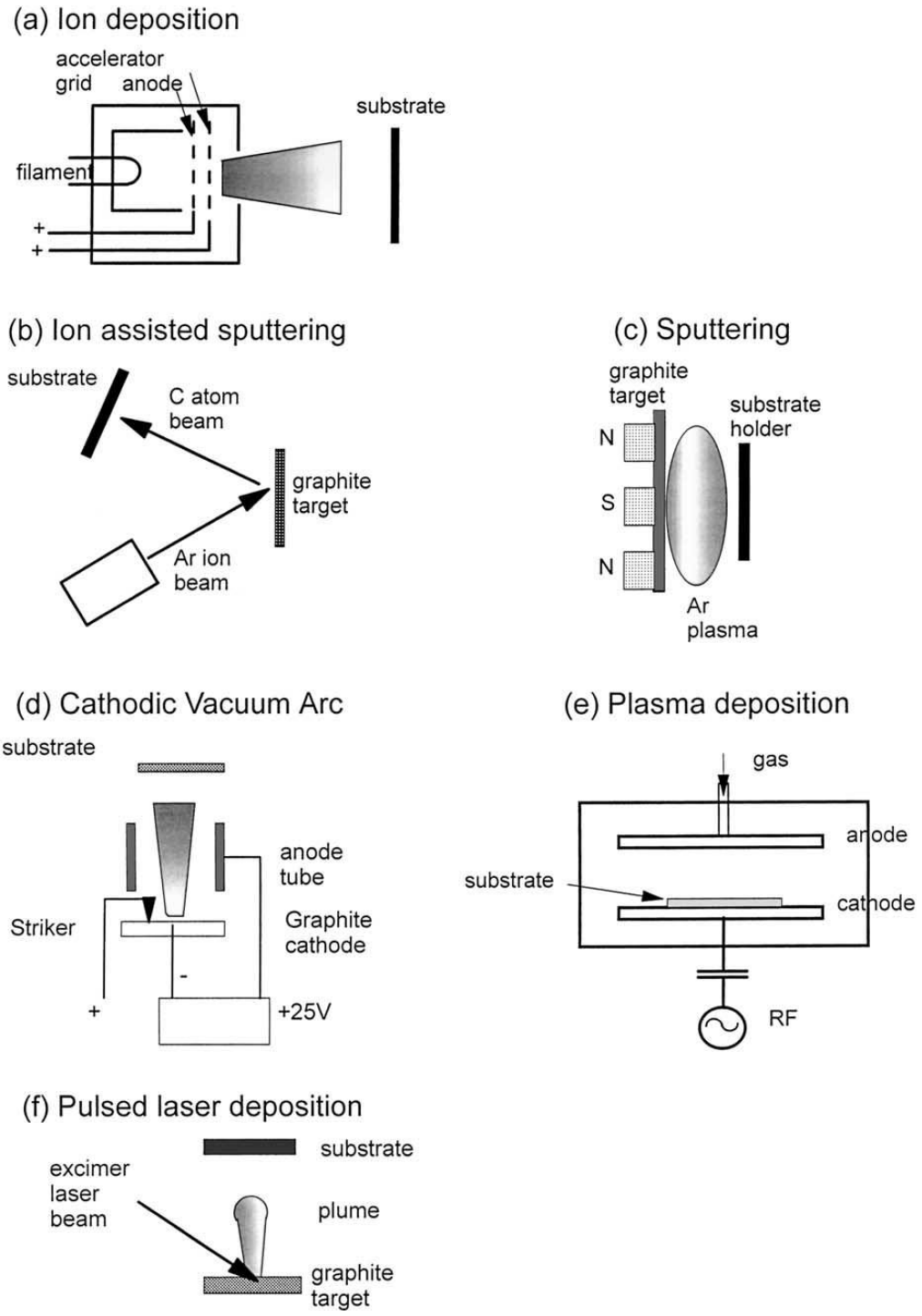

Figure 2.2 Schematics of various deposition systems for DLC [33]

This must be done vigorously enough that the atoms cannot simply spring back apart into separations characteristic of sp^2 bonds. Usually techniques either combine such a compression

with a push of the new cluster of sp^3 bonded carbon deeper into the coating so that there is no room for expansion back to separations needed for sp^2 bonding; or the new cluster is buried by the arrival of new carbon destined for the next cycle of impacts. It is reasonable to envisage the process as a "hail" of projectiles that produce localized, faster, nano-scale versions of the classic combinations of heat and pressure that produce natural and synthetic diamond [ ]. Because they occur independently at many places across the surface of a growing film or coating, they tend to produce an analog of a cobblestone street with the cobbles being nodules or clusters of sp^3 bonded carbon. Depending upon the particular "recipe" being used, there are cycles of deposition of carbon and impact or continuous proportions of new carbon arriving and projectiles conveying the impacts needed to force the formation of the sp^3 bonds. As a result, *ta-C* may have the structure of a cobblestone street, or the nodules may "melt together" to make something more like a sponge or the cobbles may be so small as to be nearly invisible to imaging.

2.2.1 Ion Beam Deposition Methods

In an ion beam deposition system [Fig. 2.2(a-b)] there are two process that use a variable ion source, namely that made in the gas phase and another created by the sputtering of the solid target. In the case of DLC a convenient gas phase ion source would be from the ionisation of hydrocarbon gas such as methane [34-36]. An ion beam is then extracted through a grid from the plasma source under a bias voltage. The hydrocarbon ion and carbon ion are directed with high speed in the high vacuum deposition chamber. The beam contains a wide flux of neutral species at a finite pressure. This may decrease the flux ratio of ions to neutrals to as low as 2-10%.

An appropriate solid phase ion source would be a graphite target. These ions are sputtered by collision with argon ions. These carbon ions produced are accelerated onto a substrate surface to deposit the DLC film. A variation of this method is the mass selected ion

beam, where the beam is passed through a magnetic field and only ions within a certain mass and energy interval are used for deposition. The disadvantage is the low deposition rate of order 0.001Å s^{-1} and the high cost and size of the apparatus.

2.2.2 Sputtering Process

In dc or rf sputtering (Fig.2.2c), a graphite cathode is sputtered by an Ar plasma [37]. Because the weak sputter yield of graphite require the use of magnetron sputtering to increase the deposition rate. Magnets are placed after the target to rotate and to increase the electron mean path and subsequently increase the degree of ionisation of the Ar ion plasma. The magnetic field passed across to the substrate, so this causes the Ar ions to also bombard the substrate and subsequently create an unbalanced magnetron. DC bias is used to vary the ion energy and the sputter species. To produce a-C:H, a plasma of Ar ions and hydrogen or methane is used and for a-C:N_x an argon-nitrogen plasma is used.

In another way, an ion beam of Ar sputters from the graphite target to create the carbon flux [37] and another ion beam of Ar is used to bombard the growing film, to increase the density of sp^3 bonding. This method is called ion beam assisted deposition (IBAD) or ion plating. A disadvantage of sputtering is that it has relatively low ratio of energetic ions to neutral species, so that it does not produce the hardest DLC films, but it is most used in industries because of its flexibility.

2.2.3 Cathodic vacuum arc System

In this method an arc is struck in a high vacuum by touching the graphite cathode with a small carbon striker electrode and removing the striker (Fig. 2.2d). This generates intense plasma with a high ion density of up to 10^{13} cm^{-3}. It uses low voltage and high current supply. The cathode

spot creates particulates that are filtered by passing the plasma along a toroidal magnetic filter duct [38]. This is called filtered cathodic vacuum arc (FCVA).The advantages of FCVA is to produce a highly ionised plasma, and high growth rates of 1 nm/s for a low capital cost. The disadvantages are that the filtering is not enough for some applications and that the cathode spot is unstable.

2.2.4 Plasma Enhance Chemical Vapour Deposition Methods (PECVD)

The rf PECVD power is always connected to the capacitor which is coupled to the smaller electrode on which the substrate is set up, and the other electrode is connected to the earth. The rf power creates a plasma between the electrodes. As electrons move with a higher speed than ions in the plasma, a sheath will generate near the electrodes with high ion density. This forms a positive space charge, thus the plasma generates a positive voltage with regards to the electrodes, which balances the average electron and ion current to the wall [39]. The sheaths works as diodes, in order that the electrodes have dc self-bias voltages balanced with their peak rf voltage. That rf voltage is split between the sheaths of both electrodes as in a capacitative divider, by virtue of their inverse capacitance. So, dc self-bias voltage changes inversely with the electrode surface area [39]. The smaller electrode which has smaller capacitance received the wider bias voltage and has negative value relative to the larger electrode. This becomes the substrate electrode. The negative sheath voltage augments the speed of the positive ions to create the sp^3 bonding on the substrate electrode. For DLC deposition, the plasma must be obtained at the lowest possible pressure, so that the Ar ion is maximised in the plasma atmosphere. However, even at 50 mTorr pressure, the ions get only roughly 10% of the film-forming flux. The ions can reduce their energy by collisions during the acceleration across the sheath .The ion energy

doesn't depend anymore on the sheath voltage. It is important to use a low pressure to minimise these collisions and to maintain a narrow ion energy distribution. The sheath thickness decreases with increasing pressure [39] and the ion mean free path becomes less than the sheath thickness at low enough pressures. We still have important ion collision in the sheath at 50 mTorr, so that there is a large ion energy distribution and the mean ion energy is only about 0.4 of the sheath voltage [40-42]. It is necessary to use lower pressure, but this is impossible for conventional PECVD as the plasma will not be deposited anymore on the substrate. The magnetic field can be applied to compress the plasma at the lower pressure, to increase the electron path length and ameliorate the yield of ionisation. This allows the apparatus to work with a very small pressure as 0.5mTorr. The ion mean free path overcomes the sheath thickness and the ion energy now becomes a narrow distribution [40-42]. This is a principle of plasma beam source (PBS) that has a magnetic field that confines the plasma then the plasma moves out through a grid at earthed potential. This repulses the positive ions through the grid, to form a plasma beam which then deposits on the substrate to form ta-C:H. As the plasma beam is not charged it can be deposited on insulating substrates [43]. The problem of the simple capacitive coupled PECVD system is that the ion current and the ion energy depend on the rf drive power. This means that the bias voltage varies with rf power and pressure, and the mean ion energy varies with the bias voltage. As we know, the magnetic field compresses the plasma to a part of the anode area. Variation of the anode position changes the bias voltage and subsequently the ion energy.

It is understood that high- density plasma sources are possible [39]. The plasma density (n_o) and the electron temperature (T_e) are two basic properties of the plasma. One of the objectives is to maximise n_o. The plasma electrons have a Maxwellian energy distribution, which defines the electron temperature, Te. The capacitive coupling at rf frequencies of 13.6 MHz, produces very

little plasma and then its density is very low, at most $\eta_B \sim 10^9$ cm^{-3}. When the rf frequency increases and reaches a VHF or using an inductive coupled plasma (ICP), it improves excitation of the plasma. In another technique, electron cyclotron resonance (ECR) framework using microwaves has been used [44-46]. ECR consist of a large static axial magnetic field to make electrons vibrate at a cyclotron resonance frequency of 2.45GHz. In that condition, the excited Ar atoms in the chamber meet the reactant gas, collide and transfer energy to the reactant gas. The latter, then deposits on the substrate. The best rf powered, high plasma-density is mproved electron cyclotron wave resonance (ECWR) source [47]. The ECWR source produces very high-density plasma of 10^{12} cm^{-3} or more. It does not control the ion energy and ion current density [45]. It has a small ion energy distribution with a width less than to 5%. The ECWR generates ta-C:H at a much higher growth rate (1.5 $nm.s^{-1}$) compared to the plasma beam deposition(PBS) and gives uniform deposition over a diameter of 10 cm. It is the first industrialised, high-density PECVD source for DLC.

The properties of a-C:H depend on the precursor gas used in PECVD. At this time, benzene is chosen a precursor with low ionisation potential due to its higher growth rate. The deposition rate rises exponentially with reducing ionisation energy [40]. For mechanical applications, acetylene has been used to maximise the hardness by minimising the presence of hydrogen. In electronic application, they have used methane because it is available in high purity, but the growth rate is lower and gives excessively high hydrogen content. The samples used in this work such as hydrogenated amorphous carbon and hydrogenated amorphous carbon doped silicon were deposited by PECVD.

2.2.5 Pulsed laser deposition (PLD) process

ArF laser generates a very short, high energy pulse, which can vaporise a solid target materials such as graphite as energetic plasma plume [48, 49-56].The plasma consists of ions which are directed towards the substrate. The advantage of PLD is that it is an universal laboratory scale method used for deposition of many different materials, from large temperature superconductors to hard coatings. This is the technique used to prepare a-C:N_x samples that have been used in our work (Fig. 2.2f).

2.3 Deposition Mechanism

DLC is dominated by the sp^3 fraction obtained by a physical process, ion bombardment [57]. The largest sp^3 fractions are realised by carbon ions of ion energy ($\sim$ 100 eV).

The atomistic description of the deposition mechanism has undergone many improvements. It starts first by comparing the ion energy ranges and the efficiency for many processes of C and H ions in solid carbon [58]. Spencer et al. [59] suggested several mechanisms, for example, the sp^3 sites appear from the sp^3/sp^2 ratio by a favoured sputtering of the sp^2 sites. The sputtering efficiency is a function of an atom's cohesive energy, which is roughly the same for the sp^2 and sp^3 sites. Spencer [59] proposed that sp^3 bonding appeared from the sp^3/sp^2 by preferential sputtering of the sp^2 sites. This model has some analogue with later models; however, the shock wave is mostly used for higher ion energies and higher ion masses. Lifshitz et al. [58] applied Auger analysis of the depth profiles of medium energy C ions incident on Ni substrates to display that growth was sub-surface. This method is called sub-plantation. They then suggested that the sp^3 sites increase by the displacement of sp^2 sites. This model was improved by Moller [60] . It has been shown that the privileged displacement is not a correct

concept and they proposed a displacement threshold [60]. It was noted that the displacement threshold of graphite is slightly anisotropic. Banhart [61] observed that the small displacement thresholds are sp^2 sites. McKenzie et al. [62] proposed that sp^2 bonded graphite fills 50% more space than sp^3 bonded diamond. This situation is clearly shown, with diamond stable at higher pressures above the Berman-Simon line. It is suggested that the aim of ion beam is to generate a compressive stress in the film, which will shift the film above the Berman-Simon line and so stabilise the high pressure diamond (-like) phase [63]. Robertson propose that that the sub-plantation created a metastable augment in density, which tends to cause the local bonding to change to sp^3preferential displacement is not necessary [64-69]. Only subsurface growth in a limited volume is needed to have sp^3 bonding. In the atomic range processes, they considered the elastic collision of ions in materials as the binary collision approximation. The cross- section of the collisions decreases with the energy. When ion energy become very large, the atomic radius reduced, then the interstices become larger. At certain energy, the ions cross an interstice and traverse the surface layer. This ion energy is denoted the penetration threshold E_p. The minimum energy of an incoming ion necessary to lift an atom from a bonded network and create eternal vacancy-interstitial pair is called the displacement threshold, E_d. The surface of the solid behaves as an attractive potential barrier of height E_B, the surface binding energy and thus the net penetration threshold for free ions is

$$E_p \sim E_d - E_B \qquad (1)$$

For an amorphous carbon on the surface [70], if ion energy is small, it will not be allowed to penetrate the surface, thus it will only glue to the surface, and form its lowest energy state which is sp^2. If the ion energy is larger than E_p, it has a chance to penetrate the surface, and enter a subsurface interstitial site. This increases the local density. In the latter, the configuration will be

changed around that atom with regards to the new density. As it is amorphous, atomic hybridisations can become more sp^2 if the density is diminished and more sp^3 if the density is improved. The penetration becomes deeper into the solid, when the energy and ion range increases. A small fraction of ion energy is used to penetrate the surface, and another fraction of about 30% is dissipated in atom displacement.

*2.3.1 Hydrogenated amorphous carbon (*a-C: H)

The deposition of a-C:H consist of many processes as shown figure 2.3. The properties of plasma deposition depends strongly on the bias voltage and hence on the ion energy which shows that carbon ions are very important element in the deposition of a-C: H. This is not the case for ta-C as the ion flux fraction is around 10% [71, 72]. The deposition of a-C:H can be obtained by different source gases such as CH_4, C_2H_4, C_2H_2 and C_6H_6. The film density variation with bias voltage for each source gas can be plotted on a scale of bias voltage per C atom in the molecule. After this, the maxima in density are found at a same energy [73]. This shows the action of the ions is still through sub-plantation. It means the energy of molecular ion incident at the film surface will be divided into atomic ions and the energy will be spread uniformly. So, each atomic ion will sub-plant independently with that energy. A complete model of a-C:H is obtained to describe the chemical process of neutral species and of dehydrogenation [74-86], plus the physical process of sub-plantation. The plasma deposition consists of three stages that are: the reactions in plasma (dissociation, ionisation etc.), the plasma-surface interaction and the subsurface reactions in the film. The plasma reactions are conducted by the energetic electrons which are defined by the electron energy distribution (EED). These are only important in the case of high-density plasmas, since the mass spectra of the dissociation pattern of CH_4, C_2H_4 and

C_2H_2 at different pressures displays that un-dissociated source gas molecules are still majority in plasma [87].

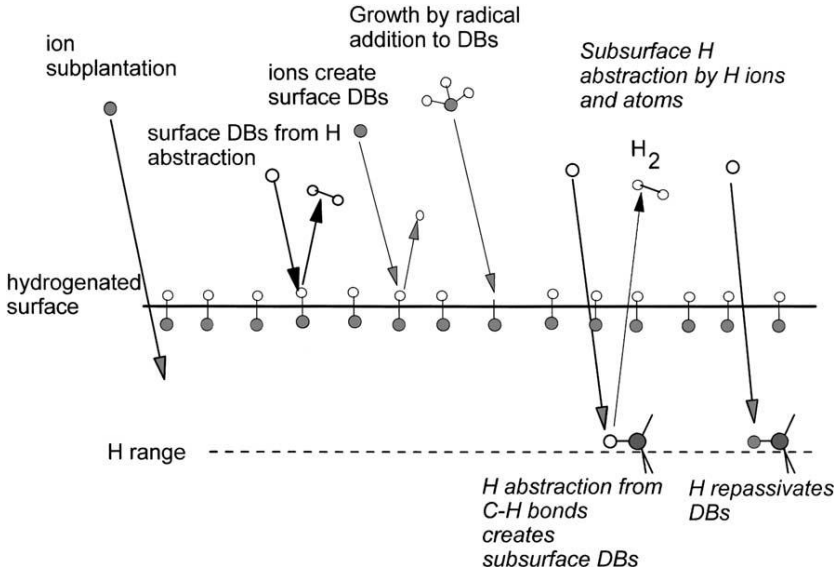

Fig. 2. 3 Component processes in the growth mechanism of a-C:H [71,72].

The plasma species which strikes onto the substrate will compose of ions, neutrals and a large amount of atomic hydrogen 'H'. It is true that the neutral species partake in the growth as the mass deposition rate overcomes the rate due to ions alone. The first effect that is observed is that when the temperature increases, the growth rate decreases. It was explained by the weak adsorption of the neutrals on the surface and which would desorbs at higher temperatures [74, 75]. The input of each neutral species to the growth rate is a function of their sticking coefficient. The a-C:H surface is generally covered with C-H bonds, thus it is chemically inert. Di -radicals and other unsaturated species can be introduce straight into surface C-C or C-H bonds, thus these species are very active in the film as their sticking coefficients are strong and tend to 1. On the contrary to methane has very low sticking coefficients of under 10^{-4} and the effect is minimised. The mono-radicals have a smooth effect. They cannot be introduced directly into a bond, they

can only interact with the film if there is an existing dangling bond on the surface .They will join with this bond to form C-C bond. The dangling bonds have to be created by displacement of an H from a surface C-H bond. This can happen by an ion moving an H atom from the bond, or by an H atom abstracting H from the bond, or by another radical such as CH_3 abstracting H from the C-H bond. Measurement have shown that atomic H' is the most efficient species for abstraction (30 times faster than CH_3) [84]. The CH_3 so adds to this dangling bond. So, the effective sticking coefficient of CH_3 is small, but it becomes strong in the presence of atomic hydrogen [83, 84].This is driving to a synergistic effect of H'atom on the sticking probability of CH_3 [84]. For neutral hydrocarbon species, the effect is not strong and they can only react at the surface. H atoms are too small; they can penetrate about 2 nm into the film [85]. There, they are able to remove again H from C-H bonds and form subsurface dangling bonds and H_2 molecules. Some of these dangling bonds will be re- saturated by incident atomic H. Ions are capable to go deeper into the film. Carbon and hydrocarbon ions can cause sub- plantation. In addition, the more important role of ions in a-C:H is to remove H from C-H bonds. This H can then abstract other H' to form H_2 molecules, and remove from the film. This is the principal method which causes the H fraction of PECVD a-C:H to decrease with increasing bias voltage. Some of the atomic H' does not recombine, but finds dangling bonds to re- saturate [86]. As hydrogen ion mass is small, they do not strongly interact with C atoms. So, H^+ ions have the longest range and reach highest depth into the film [87]. They experience the same reactions as atomic H', but to a greater depth. Therefore, von Keudell [84] conclude that a-C:H films have three characteristic depths: the surface itself is controlled by reactions of hydrocarbon and hydrogen species; the upper 2 nm in which chemistry is controlled by reactions of atomic H', and a larger depth depending on ion energy in which reactions are controlled by H^+ ions.

2.4. Atomic structure and characterisation

2.4.1. Bonding configuration

Carbon has three types of hybridisation, sp^3, sp^2 and sp^1 as discussed in the introducing section. There are carbons with four sp^3 orbitals. They consist of strong σ bonds, which form with the adjacent atoms. Other carbon atoms have three sp^2 orbitals, to form σ bonds ,the fourth p_π orbital forms π bonds with one or more neighbouring π orbital. In sp^1 configuration, they have two σ bonds along the ± x- axis .The two p_π bonds are formed in the y and z planes. All C-C bonds and C-H bonds, in the valence bands, form filled σ states, however in the conduction band the σ* states are empty. Their valence and conduction band are separated by a large σ–σ* gap [88]. While the π bonds of $sp^2$and sp^1 sites are occupied by π states and empty π* states, which are separated by very small π-π* gap [89, 90] shown in Fig. 2.4. There is a simple model of atomic structure, based on the properties of σ and π bonds [91, 92]. It was stated that with a very strong π bonding energy, the sp^2 sites will form π bonded clusters within a sp^3 bond matrix. The cluster size is in the relationship with the band gap. However, this model does not give a good estimation of cluster size [93-95]. Nevertheless it is useful for characterisation of the structure in amorphous carbon [96]. Jacob and Moller [97] were the first to use a ternary phase diagram of the carbon-hydrogen (C-H) system. Their model established two important parameters that determine the structure and properties of DLC namely; • The fraction of sp^3 bonded carbon sites • the hydrogen content. DLC structural characterisation is essentially based on these two parameters. The ordering of sp^2 sites is a third important parameter, principally for the electronic properties of DLCs.

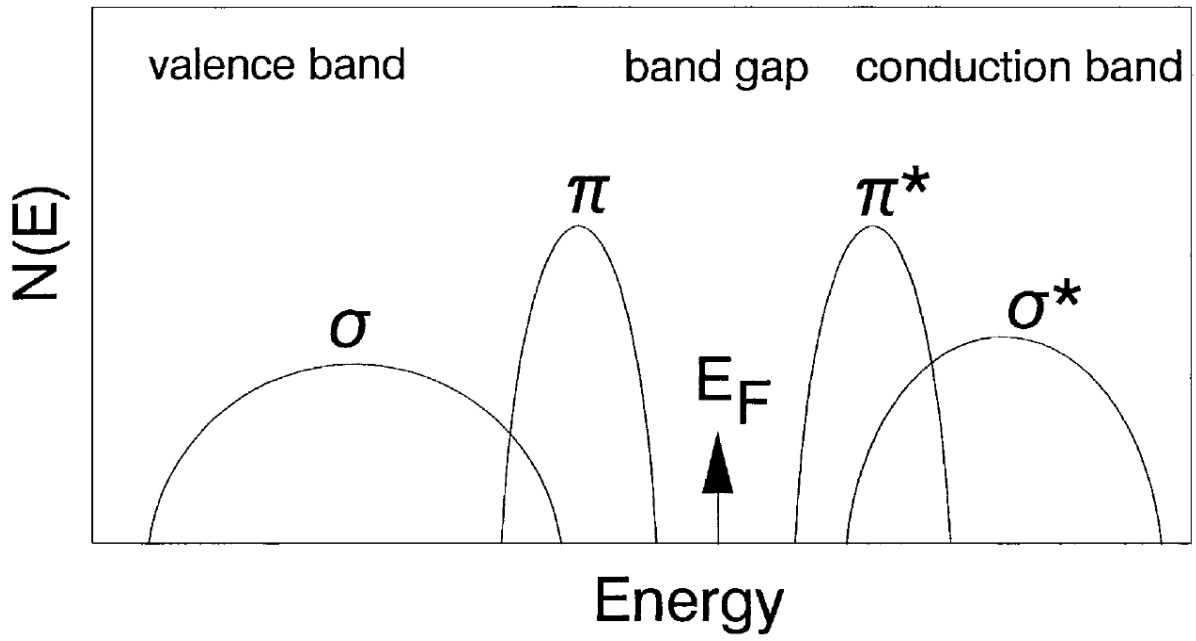

Figure 2.4 Schematic DOS of carbon showing σ and π states [1]

There are many other methods of characterisation used to determine those structure parameters such as diffraction, NMR, density and X-ray reflectivity, and so on.

In this work, visible Raman spectroscopy is used to characterise our samples.

2.4.2 Raman spectroscopy

Raman spectroscopy is the most commonly used technique for structural characterisation of carbon based materials, such as diamond [98, 99], graphites, DLCs and carbon nanotubes [88]. It is a routine process and non-destructive. A Raman spectrum of diamond consists of a single Raman active mode T_{2g} at ~1332 cm^{-1}. Single crystal graphite consists of a Raman active mode which is the zone-centre mode at ~1580 cm^{-1}, of E_{2g} symmetry labelled G for 'graphite'. Disordered graphite displays two modes, the first mode at ~1350 cm^{-1} assigned to the zone centre mode of A_{1g} symmetry and this occurs at K- point phonons [100] labelled D for disorder

and the second mode is G peak that stretches ~1580-1600 cm^{-1}. It is surprising that all the Raman spectra of most disordered carbons is still dominated by these two G and D modes of graphite, even when there are no clustering graphite [101]. These Raman parameters are very important to be explained and also to find the way to derive the structural information of DLCs by using Raman spectroscopy. A large part of the light scattered by carbon based material is elastically scattered. It is called Rayleigh scattering. A very small part of the light is scattered in-elastically. It is this scattering which gives information about energy levels of the sample. The light of an incident photon (ω, k) is scattered by the change in polarisability α due to a lattice vibration. This change in polarisability causes an inelastic scattering of photon (ώ, k′). It is called Raman scattering. The polarisation can happen when the electronic ground state is excited by incident photon into a virtual level at energy E or into real levels at E. The latter case is denoted resonant Raman scattering [102]. The Raman and IR spectra should be relatively ease and will resemble each other. This is possible in a-Si [103-105], however this is not always the case for the Raman spectrum of a-C. The π states lie at lower energy than the σ states and therefore are much more polarisable [89]. Thus Raman cross-section of sp^2 is larger than that of sp^3 sites [106-108]. Even in the case of ta-C, this only has 10-15% of sp^3 fraction, Raman cross-section of sp^2 still more sensible. The G mode consists of the stretching vibration of any pair of sp^2 sites, whether in chains or in rings [109]. The D mode is breathing mode of sp^2 sites only for distorted six-member rings. Mapelli et al. [110] have made a model in which the force field is based on the π bond clusters and polarisability. They said that a short-range field creates a long-range force. So the polarisability of π states is also long-ranged and the charges are more efficient. In addition, the long-range polarisability intensifies both G and D modes which are bond stretching modes. Further, the D mode is intensified more as it is breathing mode of six-fold rings. So the D

mode is a double resonance [111]. All these factors increase G and D breathing modes and eliminate the modes of other symmetries.

The intensity of D mode varies with atomic order. Tuinstra and Koenig [100] proposed that the ratio of D and G intensity, $I(_D)/I(_G)$, is inversely proportional to the cluster size.

$$\frac{I(D)}{I(G)} = C/L_a \qquad (2)$$

[Where C is a constant and L_a is the grain size]

This relationship is the intensity ratios that increase with the number of rings at the border of the clusters. This relationship is only valid if L_a above 2nm. For values below this the following relationship is valid [101,112].

$$\frac{I(D)}{I(G)} = CL_a^2 \qquad (3)$$

The intensity ratio decreases when the number of rings per cluster decreases and the fraction of chain groups increase. For DLC, the grain size is generally below 1 nm, this means the Eq.(3) is valid.

In conventional PECVD deposited a-C:H, the sp^3 content increases with increased H content. The role of H in a-C:H is to saturate the C=C bonds and to convert sp^2 C sites into sp^3 $=CH_2$ and ≡CH sites [101]. The a-C:H has a large sp^2 content [4,113] that have small band gap and the sp^2 sites in this material will be strongly arranged in aromatic rings. In this arrangement D peak will be present in their spectra. For the case where the a-C:H with maximum H content has a high sp^3 content, the band gap will be very large and D peaks will not appear. This means that the sp^2 sites will arrange in very small clusters. The Raman spectra of a-C: H are understood in the following way: Some sp^3 sites of a-C:H are arranged in term of the aromatic rings and others are

in chains. The H bonds which form bonding chains at olefinic sites start to become like polyacetylene. All these factors decrease G peak with increase of sp^3 content in a-C:H. Tamor and Vassel [114] have established a good relation among the Raman parameters and optical band-gap of amorphous carbon thin films.

2.4.3 Hydrogen content

The hydrogen fraction of a-C:H can be obtained by the following techniques probe the nuclear such as nuclear reaction analysis (NRA), nuclear magnetic resonance (NMR) and elastic recoil detection analysis (ERDA). There are also other methods such as combustion, hydrogen evolution or IR spectroscopy which have been used for determining hydrogen content. The nuclear processes are largely used even though they require special facilities and expensive. Their advantage is that they can derive the H:C ratio without measuring the film thickness. The NMR requires the proton decoupling utilisation to derive H content by separating the bonds of carbon and hydrogen [114,115]. It is a unique process able to determine the fraction of each type of C, its hybridisation and number of bonded hydrogen. The two other methods usually used to determine hydrogen for a-C:H are the thermal evolution and IR but they are not easy to process. In thermal evolution, the a-C:H is heated and the amount of H_2 with some hydrocarbons such as CH_4 and C_3H_8 released. This requires a complete mass spectrometer analysis then it becomes an accurate method [116,117]. In IR, the IR spectrum of the C-H bonds stretching modes can be obtained in the range of ~ 2900 cm^{-1}after measurement, the background subtracted ,the integrated weight under curve is derived and the number of H atoms per unit area is determined by multiplying by an absorption strength ,A.

$$N = A \int \frac{\alpha(\omega)}{\omega} d\omega \qquad (4)$$

The problem of this technique is that A is not a constant. Jacob and Unger [118] tried to calibrate and found the values A but it is for the simple use. This problem has been resolved by decomposing the IR band into its component absorption bands and the integrated intensity multiplied by the appropriate absorption strength A_j. Ristein et al. [116] reported on the detail, using bond absorption strength scaled from molecules. They found the values of H content are approximately the same with the H evolution on thermal process.

2.5 Electronic structure

2.5.1 The σ and π states

Disordered carbons are composed sp^2 and sp^3 sites. The sp^3 form only the σ bonds in the σ* states while the sp^2 sites have the π states and the π* states. They will be treated separately because their bonds do not have a similar characteristics. The σ bonds have two centre-bond orbitals between neighbouring atoms. All properties are dependent on the π–π* and σ–σ* states [119]. The π band can form two-centre bonds such as ethylene and in general π orbital interacts with π states and form a conjugated system that can make a continuous linkage of π bonds as in polyacetylene or graphite. These bonds are termed conjugated bonds. It is impossible to separate conjugated bonds into two-centre bonds [120]. This situation creates wider range forces and larger range polarisabilities [120].

2.5.2 Cluster model

The cluster model is the first useful model which explains in a simple way the electronic structure and bonding. This is done by taking the Huckel approximation of treating σ and π states separately [91]. The model describes the σ and π states at different energies with the π states

located in an plane orthogonal to the σ bonds at sp^2 sites. This configuration ensures that the interaction of the π states and σ bonds are minimal [89, 90] . The principal effect is that π bonding promotes a clustering of sp^2 sites, thus the binding energy of the occupied states is lowered if a half-filled band creates a gap in this band at the Fermi level, E_F. The model requires that the sp^2 sites form planar clusters by maximising the π interaction. The π bonded clusters are controlled by a sp^3 bonded matrix. Ordering of sp^2 sites determines the electronic properties and the optical gap, as their π states locate nearest to the Fermi level, while the sp^3 is correlated to the mechanical properties [88]. This model works well for micro-crystalline graphite as well as DLC thin films. However, as-deposited DLC's are more disordered than this cluster model. The sp^2 configuration controls the electronic properties and the optical gap while sp^3 matrix controls the mechanical properties. The band gap of aromatic clusters in graphite, the π states have minimum band energies given by [90, 91].

$$E_g \approx \frac{2\Upsilon}{M^{1/2}} \approx 2\Upsilon\left(\frac{a}{L_a}\right) \qquad (7)$$

[Where ΄Y is the closest neighbour V (P_π) interaction and M the number of six-fold rings in the cluster]

M can be linked to the cluster diameter or in plane correlation length L_a as $M \approx L_a^2$. Eq. (7) shows that the π states of sp^2 states determine the band gap and the latter varies inversely with the cluster diameter. Thus, this gap depends only on the sp^2 arrangement [91].

2.5.3 Network calculations

Direct simulations of networks have produced the best theories of the electronic and atomic structure of amorphous carbons. These simulations are based on the relationship between

the density versus the sp^3 fraction. Beeman et al. [121] carried out the first continuous random network model of amorphous carbons [88].

$$\Delta E = \sum_i k_r \, \Delta r_i^2 + \sum_{i,j} k_\theta \; \Delta r_i \, \Delta r_j \qquad (9)$$

They created models for a-C with three different sp^2 and sp^3 fractions, in order to compare its effect on the RDF and the structure factor. Later Robertson and O'Reilly calculated the electronic DOS for these networks and found that the networks with sp^2 sites were metallic, which disagree with experiment. This is due to the Keating potential not representing the π interaction between sp^2 sites correctly. Stillinger and Weber [122] introduced a number of atomic potentials for Si and C, where coordination can be varied, and the so -called environmentally-dependent potentials. The first model for carbon was due to Tersoff [123,124], and he applied this to generate the first large-scale model of a-C sp^2 structure. This model gives good agreement with the experimental RDF. The Tersoff potential is largely used in simulations of ion beam growth. It is known that the orientation of the π orbitals is needed to get a band gap. Tersoff and Brenner [125-127] were the first to correctly take into account the π-π interactions, which allow aligning of the π orbitals. The Tersoff potential also does not insert a repulsive term between different sp^2 layers, which is required to give a graphitic inter- layer spacing. This was corrected by Heggie [128]. Kelires [129,130] largely used the Tersoff potential to create a number of models with different sp^3 fractions, and to calculate various elastic properties of the networks. The networks of Kelires [129,130] have given valuable information on the elastic properties and stress in a-C. The empirical electronic potentials were used to carry out several simulations of the atomic structure. Wang and Coworkers [131,132] proposed an easiest model based on tight-binding. The model overestimates many sp^2 sites for the sp^3 network. Frauenheim et al. [133] used the empirical core-core repulsive term to give the correct bond length. This method

provides for a good level of approximation to retain sufficient accuracy. These calculations were the first to show that the sp^2 sites in ta-C and a-C:H were principally organised in chains (olefenic) and in rings (aromatic) in opposition to the cluster model. A later simulation observed aromatic rings in low density a-C:H. Some author's [134, 135] realise high quality plane wave Car and Parrinello calculation on ta-C. However, the calculations were limited to a small cell size, they found the unexpected result that a few sp^3 sites formed low order (three-, four -fold) rings. This is clearly true for the Keating potential. But, the calculations emphasise they exist in ta-C. Small closed rings exist in the molecules cyclopropane and cyclobutane, and then clearly some specific small bond angles are found in C systems. The density for given sp^3 content is increased by the main effect of low order rings. The small rings have little or no effect on the electronic structure, because they continuously produce states well away from E_F. These calculations were spread out to larger networks, higher accuracy and other densities by McCulloch [136].These networks should be regarded to be the most consistent. Lately, Haerle et al.[137] produced networks by tight-binding and then optimised them by plane wave methods. They obtained similar results.

All these simulations have tried to calculate sp^3 fraction versus density and they compared it with the experimental result of amorphous carbon networks. Later Bilek et al. [138] found a network of a-C:H with amazing graphitic ordering of sp^2 sites.

2.5.4 Optical gap

In the cluster model, it is the orientation of π states on the sp^2 sites that determines the band gap. It is given by [89].

$$E_g = \frac{2\Upsilon}{M^{1/2}} \qquad (10)$$

Where γ is the V (p_π) interaction and M the number of rings in the cluster

This cluster model does not give a good estimation of the size of the clusters. It is found that the distortions of cluster determine and affects the size of the band gap. The researchers such as Frauenhiem and co-workers [139], Chen and Robertson [140], and McCulloch et al. [136] have found the same result showing that the band gap increased with decreasing sp^2 content. This theory gives the same trend with the variation of experimental values of Tauc gap against sp^2 fraction for a-C:H, ta-C:H and ta-C films [141]. In amorphous semiconductor where there is no true gap,an arbitrary definition must be used for optical gap. The most important found experimentally, the two most common are E_{04} gap defined as the energy at which the optical absorption coefficient α is 10^{-4} $cm^{-}1$,and The Tauc gap is the intercept of E_g found from the graph.

$$\alpha(E)=B(E-E_g)^2 \qquad (11)$$

Tagliaferro and co-workers [142] carried out a simple model of the optical transitions. They have given attributed increasing band gap with decreasing sp^2 content [143] to a decrease in the width of the π-π^* bands, with a constant π-π^* separation. The gap depends generally on the order of sp^2, which need not vary simply with sp^3 fraction. It means that the gap does not vary with sp^2content all the time. The cluster model does not give good information but it can be useful in the case of the network of amorphous carbon. Since it consist of an inhomogeneous mixture of sp^2 and sp^3 sites when the local band gap in this network is regarded in term of distance between clusters [144]. Each configuration of sp^2 cluster forms a local band gap. The band gap of a sample is determined by the average of the local band gap of each cluster. The sp^3 matrix has a larger gap and behaves as a tunnel barrier between each sp^2 cluster. The distribution of sp^2 gaps forms inhomogeneous disorder [144]. In Raman spectroscopy, the Raman G width is

a measure of the homogeneous disorder and bond angle distortions within the network. It varies linearly with compressive stress in as-deposited films. Thus the homogeneous disorder in a-C:H attains a maximum in the most diamond-like a-C:H at a band gap of around 1.4eV, where the density, C-C bonding, mechanical hardness and stress all reach a maximum. The homogeneous disorder in a-C:H polymeric decreases to very small values. On the other hand, the inhomogenous disorder increases progressively with increasing optical gap in a-C:H. This means that the cluster size becomes smaller as the gap becomes wider, but the range of cluster sizes stays large in the large gap of a-C:H [145].

2.6 The Doping of DLC

Any semiconductor can only be used as electronic material when it can be doped to form either or both p-type and n-type materials. The challenge of DLC doping is due to its large-band gap . P-type doping has been found to be relatively easy but n-type doping is proving to be a lot more complicated. P-type doping is usually realised with boron as a dopant [146]. Boron acts as good acceptor and it is well incorporated into the structure of DLC, analogous with the case in diamond .Further It has been established that ta-C is slightly p-type doped in character [147]. This behaviour is attributed to vacancy created defects. Again, like diamond the n-type doping of DLC is more difficult. There have been many studies of nitrogen as an n-type dopant [148-150]. Dopants must fulfil two conditions: moderate solubility and having a shallow energy level. DLC has a significantly smaller band gap than diamond (ta-C has a maximum band gap of around 5.4eV). This means that the nitrogen donor level should lie closer to the conduction band. However with nitrogen substitution the site undergoes a distortion which reduces the size of the band gap. Phosphorus was difficult to dope but success has been reported with a level at about

0.55eV below E_C [151]. Another problem in amorphous semiconductors is that the density of trap states must be low enough to ensure that E_F is shifted away from the gap states. DLC doped nitrogen changes some of sp^3 fraction to sp^2 sites and increases the conductivity by the reducing the width of the band gap while pinning the Fermi level. Further nitrogen forms principally non-doping (compensated) sites. The poor doping efficiency of nitrogen is partially due to the fact that it can make so many bonding configurations in a carbon network [152] such as pyridine, pyrrole and nitrile. Capacitively coupled radio frequency (RF) plasma deposition has been used to produce p-type doped DLC films using PH_3 as a dopant gas, producing films with P content estimated to be 11% [153]. These films also showed increases in room temperature conductivity of nearly five orders of magnitude. Golzan et al [154] showed that when films were doped with 3% P, the dopant stabilised the tetrahedral network in favour of a sp^2 bonded network. The n-type doping of DLC with sulphur has started to be investigated [155], but to date no conclusive reports of a successful n-doping have been published.

2.7 Electrical properties

The electrical properties of DLC have been assumed a band structure consisting of only a mobility gap, where carriers living in gap states are localized [156]. The semiconductor behaviour is strictly dependents on the mobility gap. But the high densities of localised gap states give rise to low carrier mobility that degrades the semiconducting properties of the materials. The room temperature mobility of DLC and ta-C was found within the range of 10^{-11}-10^{-12} cm^2/V [157]. These films are characterised as high resistivity within the range 10^2 - 10^{16} Ω.cm that are dependents on different deposition conditions [158]. The resistivity of diamond-like carbon could be reduced by incorporating metals or nitrogen in the films structure [159], but due to low

doping efficiency there is no evidence that it can form p-n junctions in diamond-like carbon system. It has been confirmed that the decrease of resistivity by the incorporation of dopants can be related to graphitization [160] of the films. Nitrogen was found to be a good n-type dopant in ta-C films that raised the Fermi level from 0.91 eV above the valence band to 0.65eV below the conduction band at different nitrogen concentration [161]. Doping was emphasised by substitution in the sp^3 coordination at low N concentrations and increase of sp^2 bonding at high N concentrations [161]. Due to high intrinsic defect in ta-C the doping efficiency is low. The most probable site hosting an impurity atom is shown to be a graphite-like carbon atom site. The ratio of sp^2 sites and sp^3 sites increase as the number of the impurity valence electrons increases. DLC and /or ta-C are not established semiconducting materials but it could be used in field emission displays [162].

The electrical conductivity of the films increases with increasing nitrogen content. Due to the nitrogen doping in the films, a large amount of C and N atoms can *form the C-N_x bonds, and as an impurity centre it has activated the* conductivity performance *films*, which leads to the increase of the electrical conductivity. In addition, the nitrogen content in the films reaches saturated states, and it appears nonconductive phases, the nitrogen atoms start to decrease the electrical conductivity [163].

2.8. Mechanical property of DLC

DLC's are used as protective coating due to their excellent mechanical properties such as hardness [164]. Ta-C (20 -80 GPa) has the second highest hardness of material after diamond(100 GPa). Furthermore DLC can be also deposited at room temperature which makes them

suitable as good corrosion barriers. DLC is also important in the coating of disks and recording heads in the magnetic storage technology [164]. The disadvantages of DLC films were their intrinsic stress and thermal stability but these problems are now resolved.

2.8.1. Elastic properties

Nano-indentation [165] is a technique used to characterise the mechanical property of DLC thin films. They have used a small diamond tip to penetrate into the film and the force of displacement curve is measured. They also measure the curve for the unloading cycle. This technique is used to determine the Hardness and the Young's modulus. In this technique the value of Poisson's ratio must be approximated. As it is known that the indentation depth is limited to a fraction of the order of 10% of the total film thickness, so the method gives a good approximation of the hardness, but the uncertainty is larger for the Young's modulus [166]. The direct way to measure the elastic moduli is using surface acoustic waves. The technique is called laser induced surface acoustic waves (LISAW). It allows determination of the Young's modulus **E** and also gives the shear modulus. Another related method to measure moduli is surface Brilloum scattering (SBS) [167]. In this experiment, the photons from a laser are inelastically scattered off thermal phonons in the film and detected at an angle, they have obtained frequency dispersion relation in function of wave number of the phonons. There are many advantages of this technique. It is non destructive, it can be used on films as thin as 10 nm of DLC. This technique gives us the Young' and shear modulus with higher accuracy, and the bulk modulus and poisons ratio with lower accuracy [168].

Chapter 3

Experimental Details

3.1. Raman Experimental Arrangement

3.1.1 Introduction

The phenomenon of Raman scattering has been observed in 1928, a long time ago. The Raman scattering is used on a large scale to study materials since 1960. The Raman scattering effect is not very strong, only one in 10^8 photons incident being Raman scattered (Kagel 1991). This meant that intense incident radiation and very sensitive apparatus had to be used. These problems have been solved by the commercial availability of lasers, and the production of very sensitive spectrometers (Adar 2001). These developments have made Raman spectroscopy readily accessible and one of the most useful and most reliable techniques of studying and characterizing materials [169].

3.1.2 Experimental Apparatus

3.1.2.1 The Laser

A laser is a source of intense, coherent monochromatic radiation. Two different excitation wavelengths were used in this work, namely the 488 nm line from a coherent argon ion laser and the 647 nm line from a Spectra-Physics Krypton ion laser. These belong to the set

of noble gas lasers, where laser light is produced by the amplification of the electronic transitions of the ionised states of noble gas atoms.

The gas is enclosed in sealed cylinder, termed a plasma tube, at a low pressure. An intense electric discharge between two electrodes is used to generate plasma, comprising of ionised gas particles and electrons. The electrons strike neutral gas particles, causing them to ionise and become highly excited.

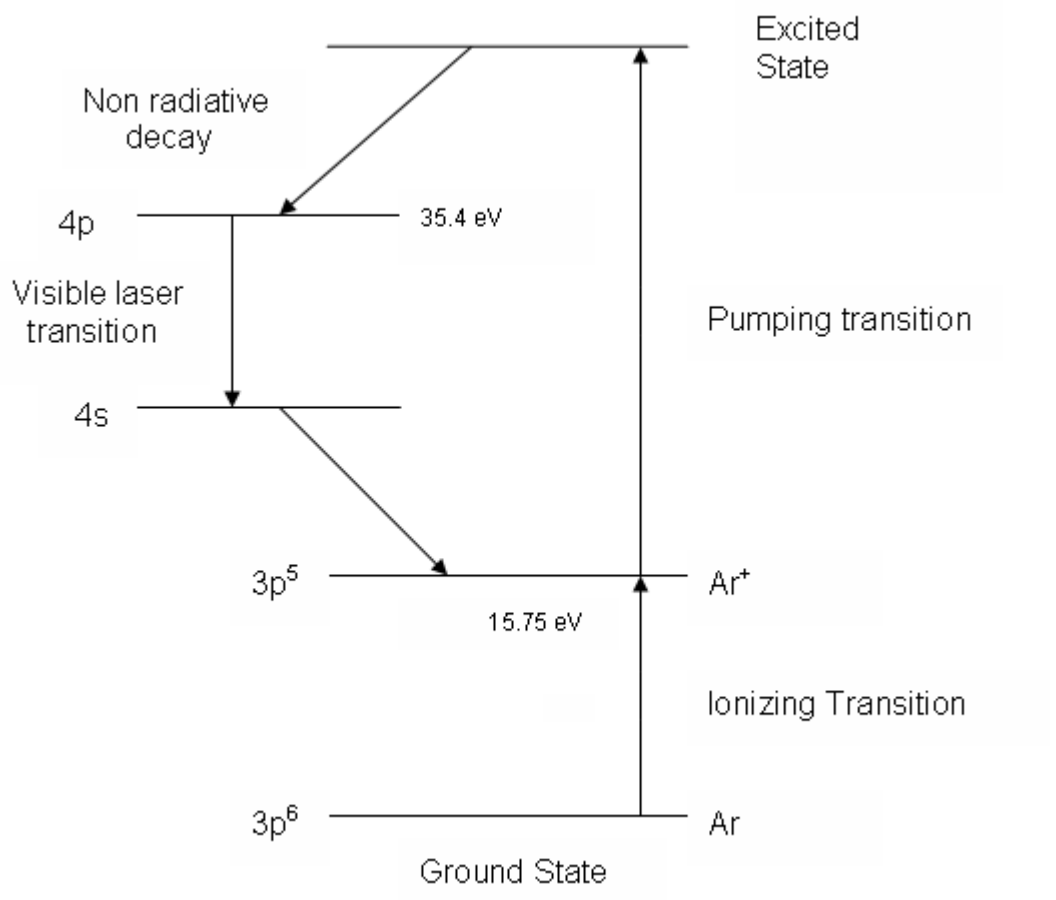

Figure 3.1 ***A transition scheme for an Ar^+ laser. The first collision ionises the neutral argon and the next pumps it to an excited state (from the Operational Manual for the Spectra Physics 2020/2025 Ion Laser).***

In the Ar^+ laser, in the first collision the electron ionises the argon and the second collision bring it to an excited state (Figure 3.1). The lifetime is very short at that level and the ion decays to the 4*p* energy level without giving out radiation. The 4*p* energy level has a relatively long lifetime, allowing the population of a large number of ions in that level. This condition creates what is termed as population inversion, in which the density of ions in the higher energy levels surpasses that in the ground state. Population inversion is one of the required conditions for a laser to operate. The 4*p* ions then decay into the 4s level, either spontaneously or by activating a photon of equivalent energy. The transition is radiative and gives a photon of which the wavelength can be written in following way:

$$\lambda = \frac{hc}{E}$$

where *h* is Planck's constant, *c* the speed of light in the vacuum and *E* the energy separation between two different states.

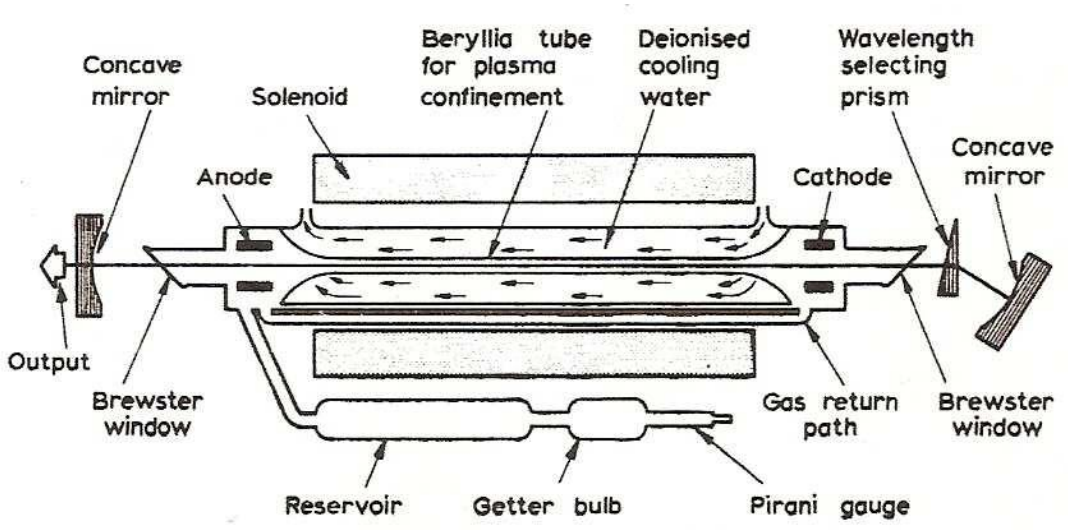

Figure 3.2 ***Schematic diagram of a gas laser***

The light energy sent through stimulated emission in the plasma tube is kept in the optical cavity of the ion laser. Figure 3.2 displays a schematic diagram of the laser optical cavity. At one site is a high reflector mirror with a reflectivity of 100%, and at the other site is an output mirror with a reflectivity of slightly less than 100%. The emitted photons move back and forth between these mirrors and in the process they created more ions to produce photons. A small percentage of the photons can pass through the output mirror and these make up the output laser beam coming from the population inversion, photons emitted by the stimulated emission process are emitted coherently and greatly exceed those emitted spontaneously that are incoherent. The design of the long optical cavity ensures that the activated photons are sent out co-linear with the cavity axis, whereas the spontaneous photons are arbitrarily emitted and hence the relatively few on-axis photons result in a very weak incoherent noise overlaid on the beam [169].

3.1.2.2 The Raman Spectrograph

Figure 3.3 displays a schematic diagram of the Jobin-Yvon T64000 Raman spectrometer used in School of Physics. Laser light is diffracted through the spectrometer by optical mirrors. Raman Spectra were obtained using an Olympus BX40 microscope attachment which focused the light on the sample. The Spectrometer was operated in single Spectrograph mode. At point "A" on the diagram is the location of the plasma line filter that takes out the laser plasma lines by narrow band pass filter and allows only the laser line to be transmitted into the microscope. Backscattered light returns from the sample through the microscope into the spectrometer, where it is processed in any one of the three configurations of the spectrograph. In the single spectrograph mode, the beam is directed to

a holographic notch filter, at point " B" which strongly filters out the Rayleigh scattered light but allows the Raman scattered light to pass through. The transmitted light then passes through an entrance slit and falls on a grating where it is dispersed. Two different types of grating are available with the spectrometer and might be used interchangeably using the software. The choice of grating depends on the resolution and spectral range required. The 600lines/mm grating gives a wide spectral range but resolution is reduced, whereas the 1800lines/mm grating has a narrow spectral range but improved resolution. The 600 lines/mm grating was used in this work

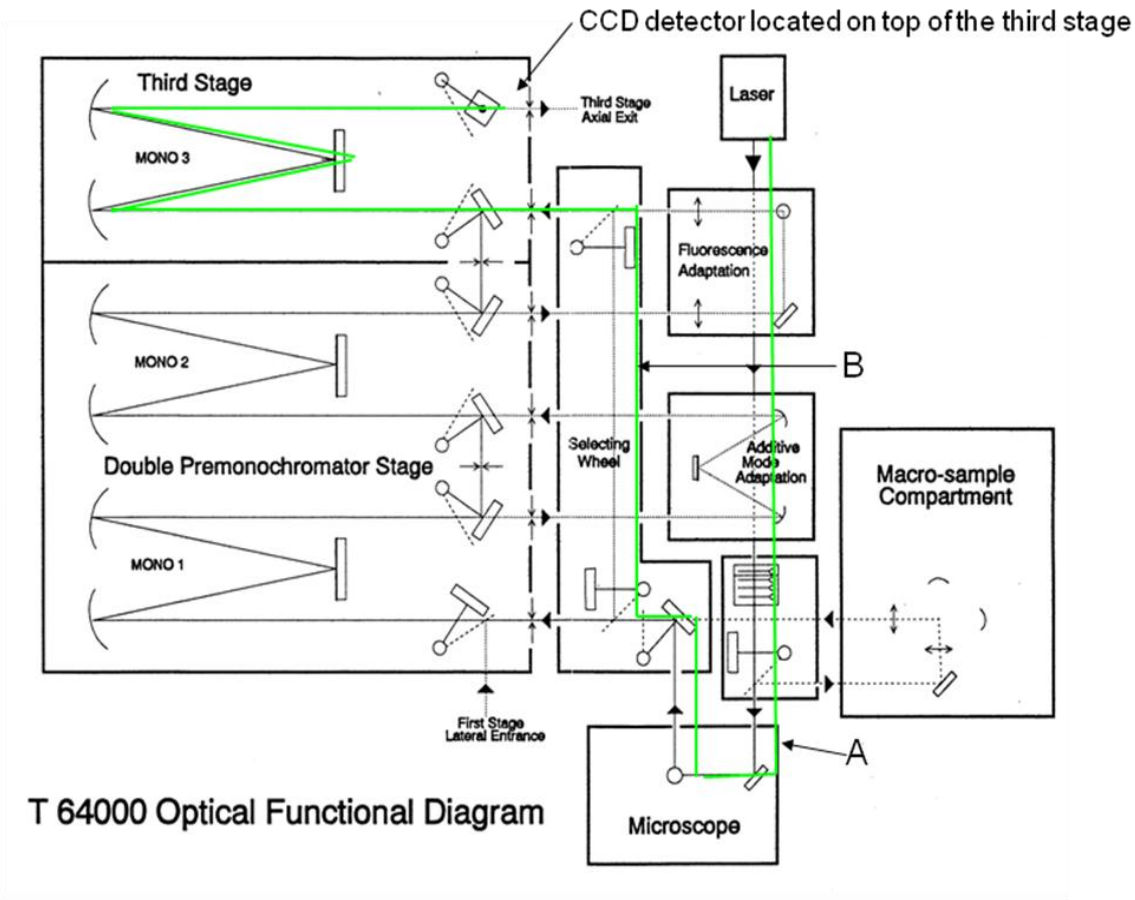

Figure 3.3 Schematic diagram of the Raman Spectrograph showing the beam trajectory. (From the Instruction Manual for the Jobin-Yvon T64000 Raman spectrograph)[169].

The incident laser beam was focused onto the sample using a 100X objective, backscattered light dispersed by the grating falls on the charge coupled device (CCD) detector, which monitors the scattered light and produces a spectrum. The CCD detector is situated on top of the third (final) stage spectrograph as indicated on the diagram. The CCD is a rectangular chip consisting of 1024 x 256 pixels, where the light is dispersed along the 1024 pixels and binning of the measured photons takes place along the 256 pixels and each pixel being a silicon photo-sensor. When scattered light falls on a pixel, photoelectrons are produced in numbers proportional to the intensity of the radiation. For optimum performance, the CCD is cooled to 140K by liquid nitrogen. The spectra were acquired and displayed using Lab Spec V4 software. For the 488 nm measurements the power at the sample was 1.3mW, and for the 647.1nm measurements the power was 1.38mW. The spectral resolution was better than $4cm^{-1}$for both wavelengths. The advantage of the single spectrograph mode is that it has a higher throughput and offers rapid analysis time. Its disadvantage is that it cannot be used for Raman bands near the frequency of the laser line. The readout from the detector goes via the CCD controller to the computer, where the Labspec software captures the output and displays it for saving and processing [169].

3.2 I-V characteristics of DLC films by 4140B p.A Meter/DC voltage Source.

3.2.1 Description of the instrument

The HP Model 4140B pA Meter/DC Voltage Source shown in fig.3.4 a high stability pA Meter with 10^{-15}A (max) resolution coupled with two programmable DC Voltage sources to secure useability in many application fields. The pA meter has a basic accuracy of 0.5% over

wide measurement ranges ($\pm$0.001X10^{-12} - 1.999 X10^{-2}A) allowing stable pA current measurement at 10^{-15}A (1 count). This is accomplished by using a new unique, variable, digital, integration method. This stable and fast (less than 35ms at 1nA) measurement technique is very useful, not only for the measurement of the small outflow currents of semiconductor devices and the static characteristics of FET, but also for making insulation resistance/leakage, current/absorption measurements/analyses of capacitance and insulation materials. One of the programmable DC Voltage sources (V_A) can work not only as a programmable DC voltage source, but also as a unique staircase and accurate ramp generator. The DC voltage source has an output range of $\pm$100 V in 100 mV steps or $\pm$10V in10 mV steps, and the ramp rate can be set from 0.001V/S to1V/s at0.001V/s resolution. The sweeps of the staircase and ramp functions operate, both in the auto sweep mode with a pause key and in the manual sweep mode with down and up keys. Each programmable DC voltage source (V_A and V_B) has a current limiter to avoid damaging the DUT by excessive current [170].



Figure 3.4 Model4140B and supplied Accessories (From manual HP4140B p.A Meter/D.C Voltage Source) [170]

3.2.2 Measurement of I-V Characteristics

The 4140B pA Meter/ DC Voltage is connected with the 3488A Switch/Control unit plate via BNC connector to source voltage through selected relay configurations and simultaneously measure the current flowing in the sample through two probe geometry. The voltage from the HP 4140B was sourced from the V_A output via a female BNC connector to sweep voltage values to the sample through a selected relay configuration of the HP 3488A switch/control unit. Current measurement at the other end of the samples was carried out using a Triaxial cable after grounding the chassis and the force pin of the cable. A HP 3456A Digital voltmeter was connected in series to read out the voltage output from the terminal V_A of the HP 4140B device. All these three apparatus were interfaced using home built Lab View via GPIB control for I-V characteristics measurements. The first sweep involved the variation of voltage values from +3V to -3V in steps of 0.01 V, this was later followed by the voltage range sweep from-3V to 0V at a similar step size of 0.01V. Lastly for completion of the hysteresis loop, a voltage range of 0V to +3V with a larger step size of 0.1V was selected. The voltage – current (I-V) characteristic was carried out sequentially after sourcing voltage and simultaneously measuring the current through the sample using the picoammeter (pA) HP 4140B module.

Chapter 4

Results and Discussion

4.1 Introduction

Since last few decades, many researches are oriented towards diamond-like carbon (DLC) films because of their hight application potential in electronic, optical, and wear protection applications. DLC has properties similar to those of diamond material because the degree and presence of sp^3-bonding configuration. These applications are possible due to the following material properties of DLCs which are chemical inertness, high hardness, low friction and high thermal conductivity. Among all deposition process the CVD process is more superior to any other process. In this study DLC films were prepared using acetylene (20 sccm for all) as a carbon precursor by plasma enhanced CVD (PECVD) method at different bias voltage in presence of Ar^+ atmosphere (10 sccm) [4,6]. Silicon was used as a dopant in the growth of DLC films (DLC:Si) at different flow rate (sccm) precursor of tetramethylsilane [$Si(CH_3)_4$, TMS] vapor as a Si precursor while keeping all other parameter constant during deposition [4,7]. The microstructure of DLC and DLC:Si are studied with help of Raman spectroscopy. Raman spectroscopy is a non-destructive process for structural characterization of any carbon materials. In this work, we obtained visible Raman spectra of DLC, excited by 488- or 647 nm photons, which is dominated by the G band and a D band, both of which only depend on sp^2 - bonded carbon. The silicon substrate peak measured the different absorption in the sample .The list of DLC and Si-doped DLCs thin films with their deposition parameters are listed below in table 1.

Table 1 (a) DLC films deposited at different bias voltage (V_B) and (b) DLC films deposited at different TMS flow rate at constant bias voltage (400 V). [C_2H_2 = 20 sccm, Ar^+ = 10 sccm)]

(a) DLC films deposited on silicon substrate at different bias voltage.		**(b) DLC films deposited on silicon substrate at different TMS flow rate and at V_B= 400 V.**	
Type	**Bias Voltage (V_B)**	**Type**	**TMS flow rate (sccm)**
a-C:H	**100 V**	**a-C:H:Si**	**5**
a-C:H	**300 V**	**a-C:H:Si**	**10**
a-C:H	**400 V**	**a-C:H:Si**	**20**
		a-C:H:Si	**30**
a-C:H	**600 V**	**a-C:H:Si**	**40**

4.1.1 Raman spectroscopy of diamond like carbon (DLC)

The Raman spectra DLC thin films obtained at 488 nm of LASER excitation energy are shown in Fig. 4.1.1.1 in the range of 1000 - 1800 cm^{-1}.Raman peak of the silicon substrate was observed around 950 cm^{-1}. This peak is measuring the transparency of the films close to the wavelength of 488 nm. It is observed that the spectral features are similar for all spectra. The G-peak mode and D-peak mode of visible Raman are observed around 1580-1600 cm^{-1} and around 1350 cm^{-1} respectively.

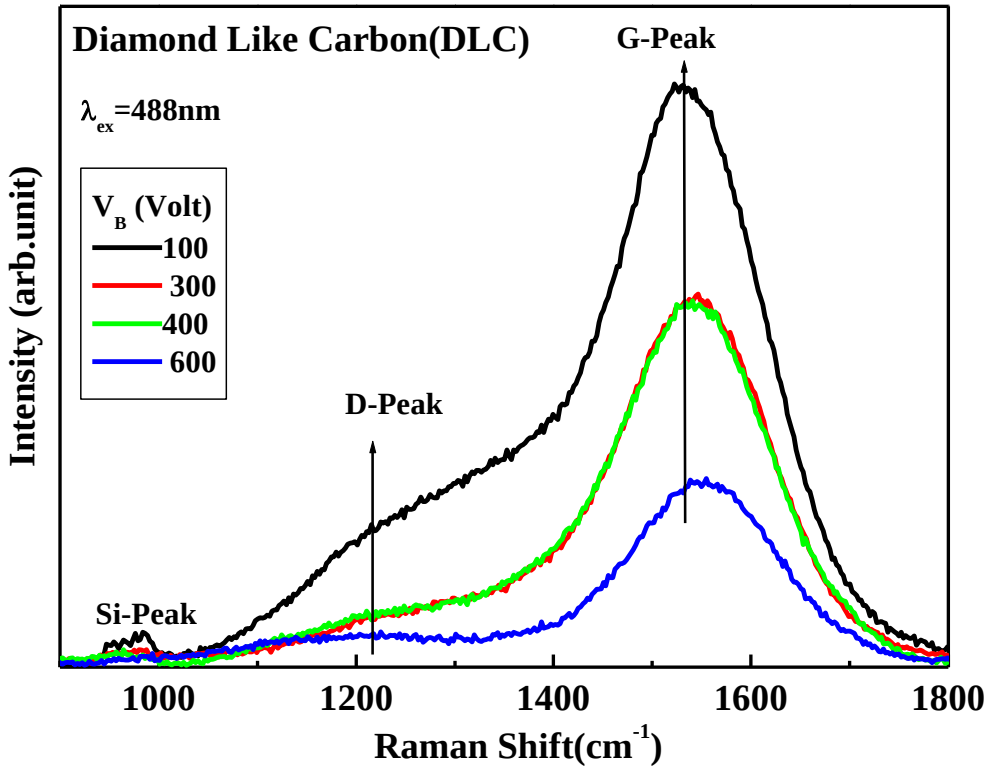

Figure 4.1.1.1 Raman Spectra of DLC films deposited at different bias voltage [LASER excitation wavelength λ_{exc} = 488 nm]

The important fact that G and D peaks vary its intensity position, and width. This continues to dominate the Raman spectra of all the carbon material even those that does not have graphitic ordering. Overall the spectra shows that the intensity of D-peak gradually decreases with increase of bias voltage during deposition process indicating the number of defects and resulting broken symmetry of the basal plane decreases. Here, it is mentioned that all the DLC films are similar thickness and is ~150±15 nm. However, to obtain the clear evidence for the presence of D-peak and G-peak in all spectra, we have deconvoluted all Raman spectra into distinct D-peak and G- peak using two Gaussian's peak after subtracting a best fitting base line and are shown in Fig. 4.1.1.2 for the spectra obtained at the LASER excitation wavelength 488

nm. We have obtained the D-Peak and G-peak positions, their peak width (W_D and W_G), and their corresponding I_D/I_G ratios. These results are tabulated in table 2 for Raman spectra of LASER excited wavelength 488 nm.

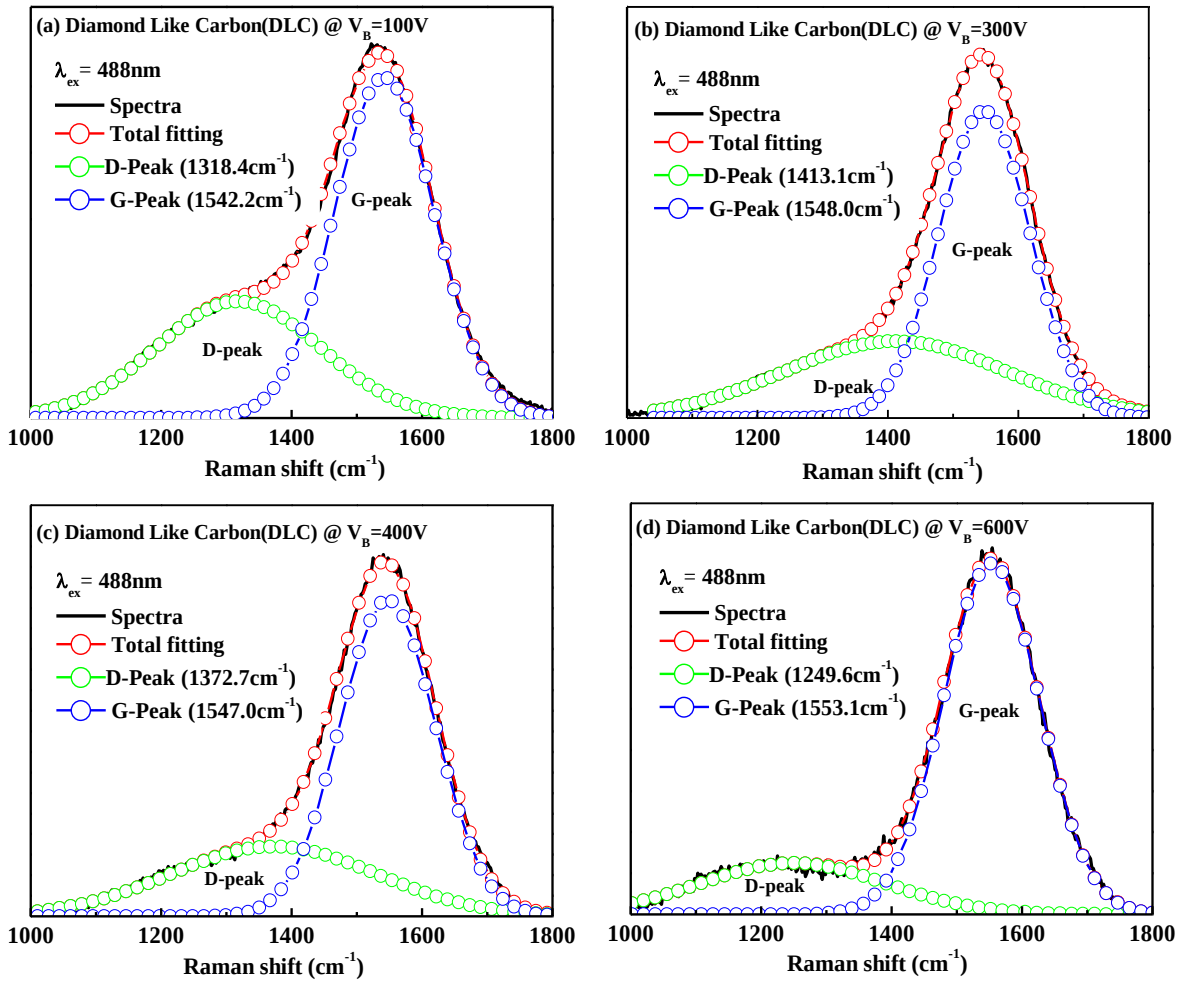

Figure 4.1.1.2 Deconvoluted into D-peak and G-peak of Raman Spectra of DLC films deposited at different bias voltage: (a) 100 V, (b) 300 V, (c) 400 V and (d) 600 V [λ_{exc}= 488 nm]

Table 2 Results obtained after deconvolution of the D and G-peaks when excitation energy of wavelength (λ_{ex}) = 488 nm

Sample description	Peak Position		Width		I_D/I_G ratio	
	D-Peak (cm^{-1})	G-Peak (cm^{-1})	W_D (cm^{-1})	W_G (cm^{-1})	From Area	From Height
DLC V_B =100V	1318.4	1542.2	353	136	0.67	0.34
DLC V_B = 300V	1413.1	1548.0	341	139	0.61	0.25
DLC V_B = 400V	1372.7	1547.0	315	147	0.47	0.22
DLC V_B = 600V	1249.6	1553.0	279	149	0.27	0.14

Table 2 shows the results obtained from Raman spectra at the excitation wavelength 488 nm of DLC films deposited with acetylene precursor (C_2H_2 = 20 sccm) at different bias voltage (V_B) using PECVD method in Ar^+ (10 sccm) atmosphere. The results show that the FWHM of G peak (W_G) increases with increase of bias voltage during deposition process. This indicates the increase in sp^3-fraction in the DLC film structure. The I_D/I_G ratio decreases in terms of both height and area of the corresponding D-peak and G-peak with the increase bias voltage that further confirms the formation of higher sp^3-content in the films structure and forming more and more diamond like carbon films. The precursor gas C_2H_2 is used in this PECVD process and it has a significant effect for the formation of DLC thin films as well as their properties. It is well known that the acetylene (C_2H_2) has a small H/C ratio that affects the resulting film. The result also shows that the G peak positions of DLC films are gradually shifted at higher energy level (from 1544 cm^{-1} to 1553 cm^{-1}), when bias voltage (V_B) increases gradually that reveals the formation of higher sp^3-content. The FWMH of G peak (W_G) increases whereas the D peaks width (W_D) decrease indicating the decrease of disorderness of the DLC films decreases with increase of bias voltage during the deposition process. The FWHM (G) studies the structural

disorder caused by defect of the bond angle and bond length in amorphous carbon films. This parameter increases with augmentation of the mechanical properties and also with increase of Csp^3-Csp^3 bonding content in the film. The I_D/I_G ratio in terms of height and area is a parameter which gives the amount of ring-like sp^2 clusters and their disorder in a-C:H films. In this case, the intensity of height and area ratio decreases mentioned above that further implies that the sp^2 clusters size decreases with the decrease of rings number and their disorder increases. It means that when the bias voltage increases during deposition process then some sp^2-C is converted to sp^3-C that becoming stronger / harder films. The I_D/I_G ratio decreases by increasing bias voltage as given in table 2. These ratios are related with the sp^2 sites configuration i.e. topological disorder. The decrease of ratios indicate that the sp^2 decrease in rings and rise in chains. The FWHM (G) increase with increase bias voltage. This suggests that the structural disorder and mechanical properties such as hardness and elastic modulus increase with bias voltage. Thus, the ring-like sp^2 transforms to sp^3 chains and raises the amount of sp^3-chains. The increase sp^3-content correlates with the hardness of the films, in agreement with the work done by Tamor and Vassel [114] by using Raman spectroscopy with visible excitation wavelength 514 nm of a-C:H.

We also studied the Raman spectroscopy of these DLC films using the LASER excitation wavelength of 647 nm as shown in figure 4.1.1.3. We have followed the similar fitting process (*as used in the above case: DLC films at the λ_{exc} = 488 nm*) for the decomposition of all Raman spectra into D-Peak and G-peak. Figure 4.1.1.4 obtained similar results as found in earlier case (λ_{exc} = *488 nm*). Overall it is found that the sp^3- and sp^2-bonded carbon atoms increased and decreased respectively, when V_B increased from 100 to 600 V indicating the formation of more diamond-like carbon films. We have observed the effects of the excitation two different LASER wavelength (λ_{exc} = 488 nm and λ_{exc} = 647 nm) on the G-peak position and their peak-widths,

FWHM (Full Width Half Maximum). The Raman G-peak position and its width one dependent on the LASER excitation wavelength. The variation of dispersion of the G-peak using different excitation wavelength in DLC films is tabulated in Table 3. The G-peak increases in more disordered carbon and the dispersion increases with the degree of disorder in amorphous carbon. The FWHM of the G-peak is inversely proportional to excitation energy due to the gap variation of the DLC films. larger band gap is excited by a wider excitation energy at the same wave-number. The width of the peak also increases because of the variation in the number of sp^2 C and sp^3 C atoms closest neighbors.

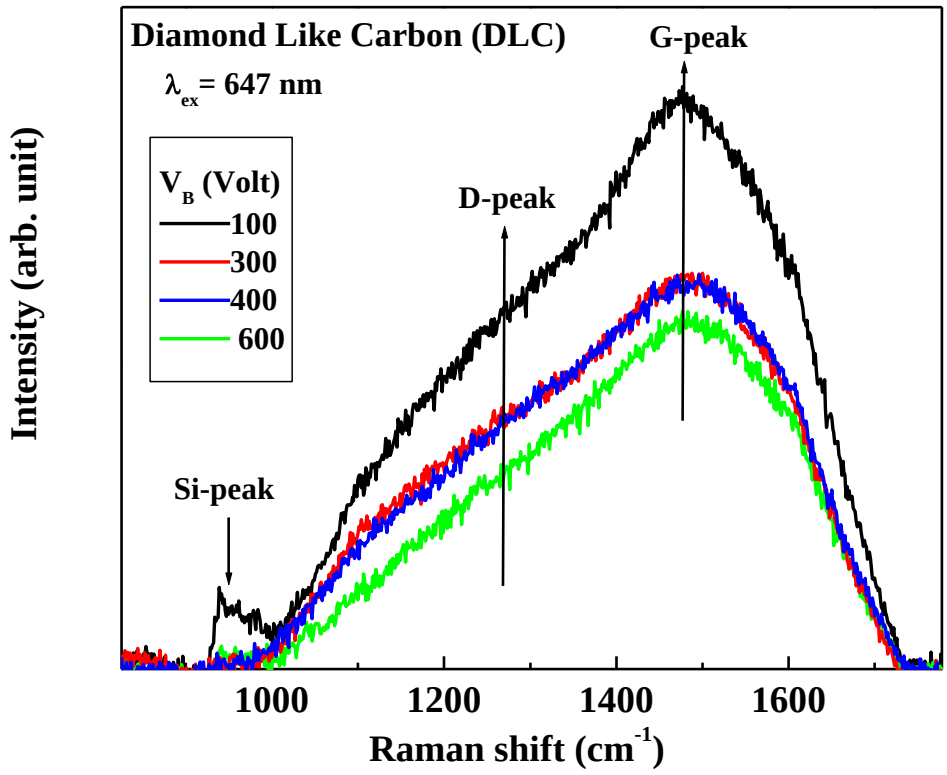

Figure 4.1.1.3 Raman Spectra of DLC films deposited at different bias voltage [λ_{exc} = 647 nm]

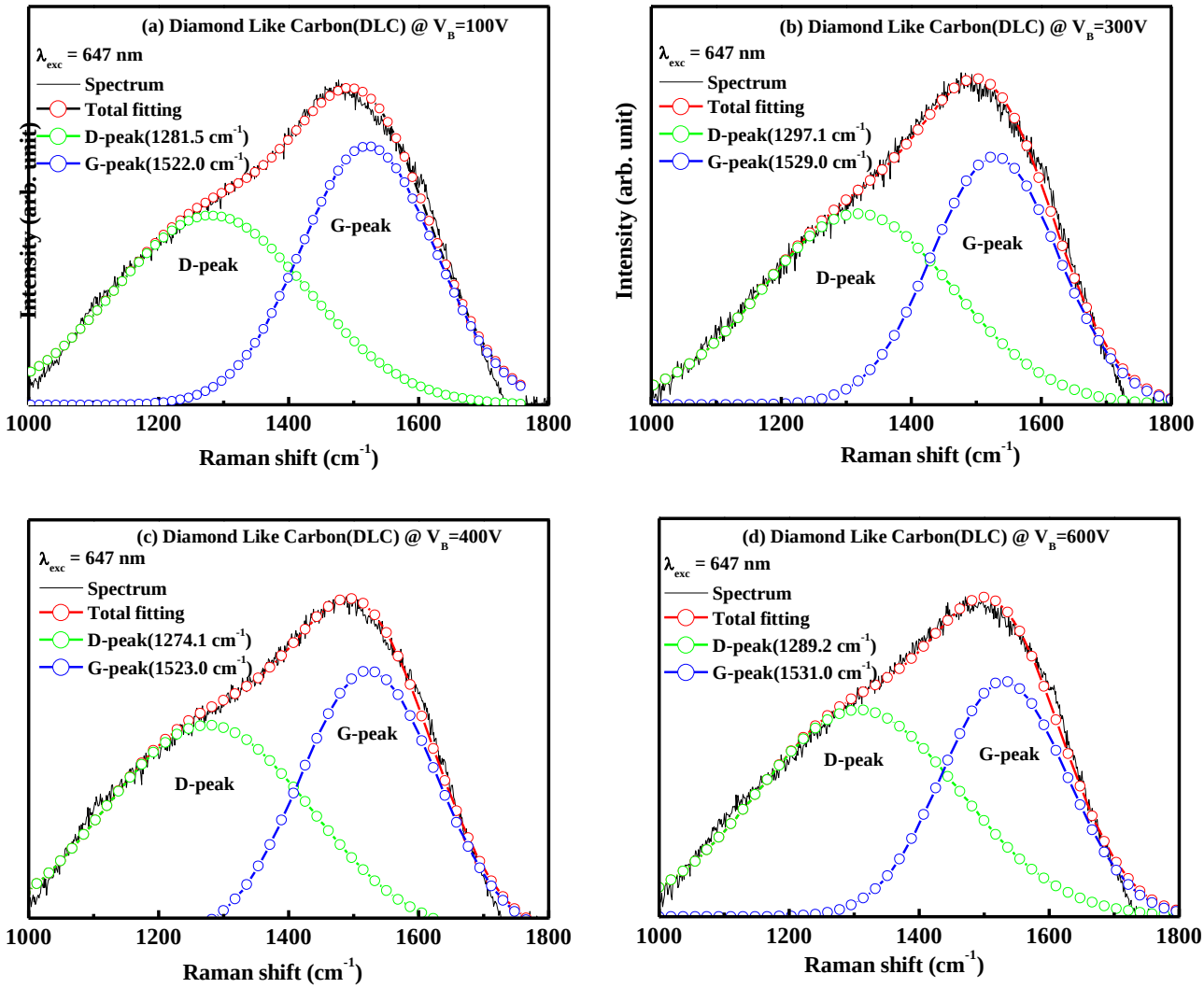

Figure 4.1.1.4 Deconvoluted into D-Peak and G-peak of Raman Spectra of DLC films deposited at different bias voltage: (a) 100 V, (b) 300 V, (c) 400 V and (d) 600 V [λ_{exc}= 647 nm]

Table 3: **Results obtained after decomposition into two Gaussian peaks *viz* D-peak and G-peak when LASER excitation energy of wavelength (λ_{ex}) = 647 nm**

DLC thin films prepared at different V_B	λ_{exc} = 448 nm G-Peak (cm^{-1})	λ_{exc} = 647 nm G-Peak (cm^{-1})
V_B=100V	1543	1522
V_B=300V	1548	1529
V_B=400V	1547	1523
V_B=600V	1553	1531

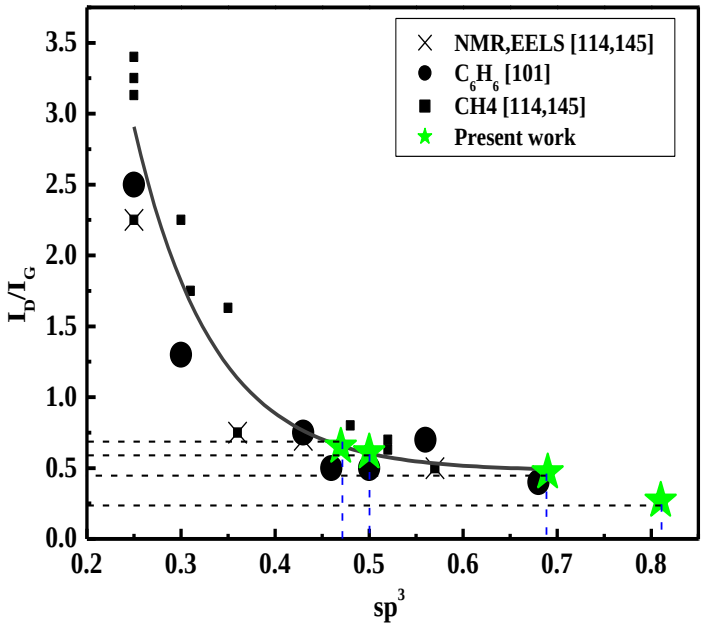

Figure 4.1.1.5 Variation of the Raman $I_{(D)}/I_{(G)}$ ratio of DLC thin films with sp^3-content at LASER excitation wavelength λ_{exc} = 488 nm [184]

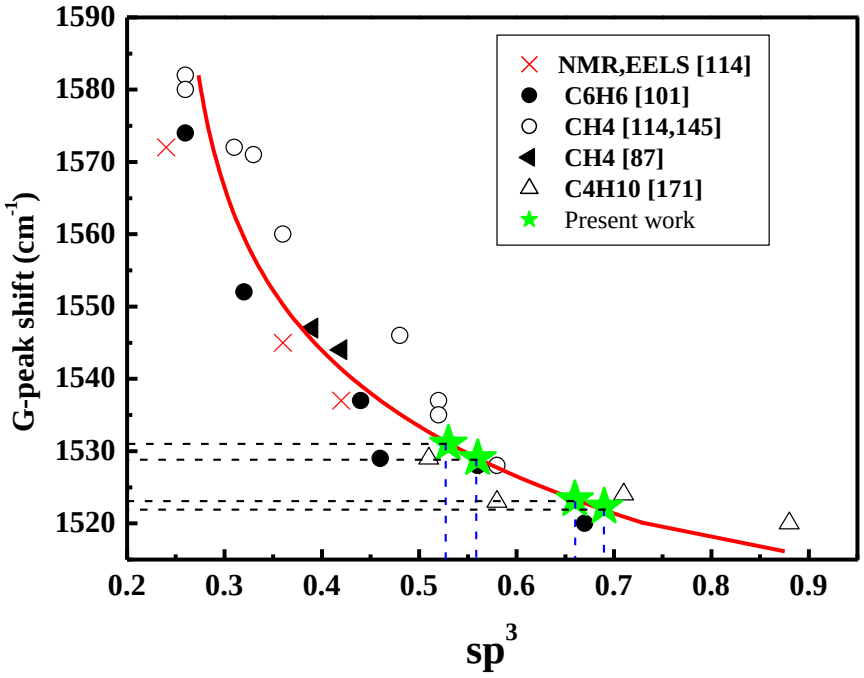

Figure 4.1.1.6 Variation of G-peak position shift of DLC thin films with sp^3-content at LASER excitation wavelength = 488 nm [145]

We have estimated the sp^3 fraction of all DLC films with help of statistical results of I_D/I_G versus sp^3concentration [219] curve as shown in Fig.4.1.1.5. In this figure we have used the I_D/I_G ratio values obtained from the Raman data when LASER excitation wavelength (λ_{exc}) is 488 nm. This sp^3 values also obtained from the G-peak position as shown in Fig. 4.1.1.6, where we have used the G-peak shift from the Raman spectrums when excitation wavelength (λ_{exc}) is 647 nm. It is found that the trends of both values are similar and the values are well matching each other. Ferrari et al. [184] plotted the statistical Tauc Gap (eV) values I_D/I_G ratios in carbon materials. From this data curve we have also obtained the Tauc Gap results (E_g) as shown in Fig. 4.1.1.7. It is found that the E_g (eV) is increases with decrease of I_D/I_G ratios when bias voltage increases in our DLC thin film during the deposition process that further confirms for the formation of sp^3-rich carbon films

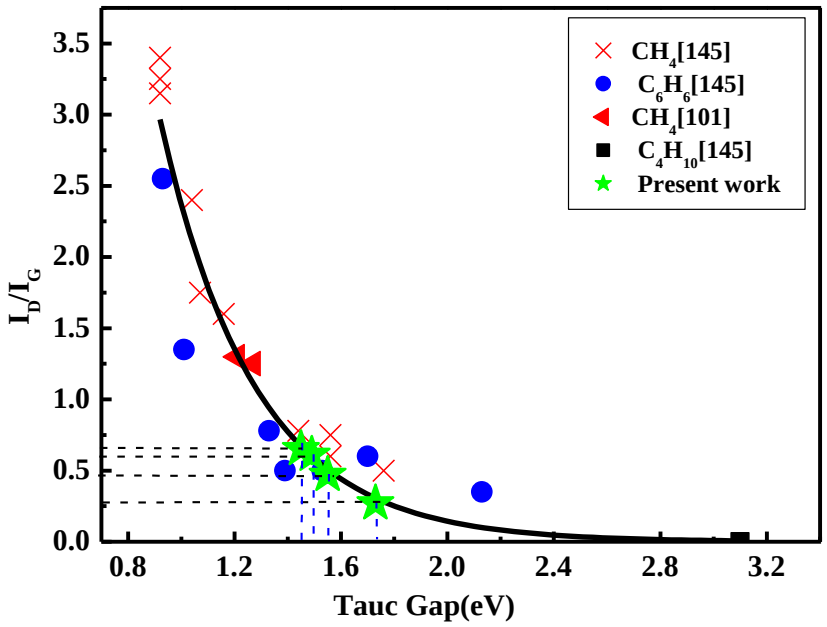

Figure 4.1.1.7 Variation of $I_{(D)}/I_{(G)}$ ratio of DLC thin films with optical Tauc gap [145]

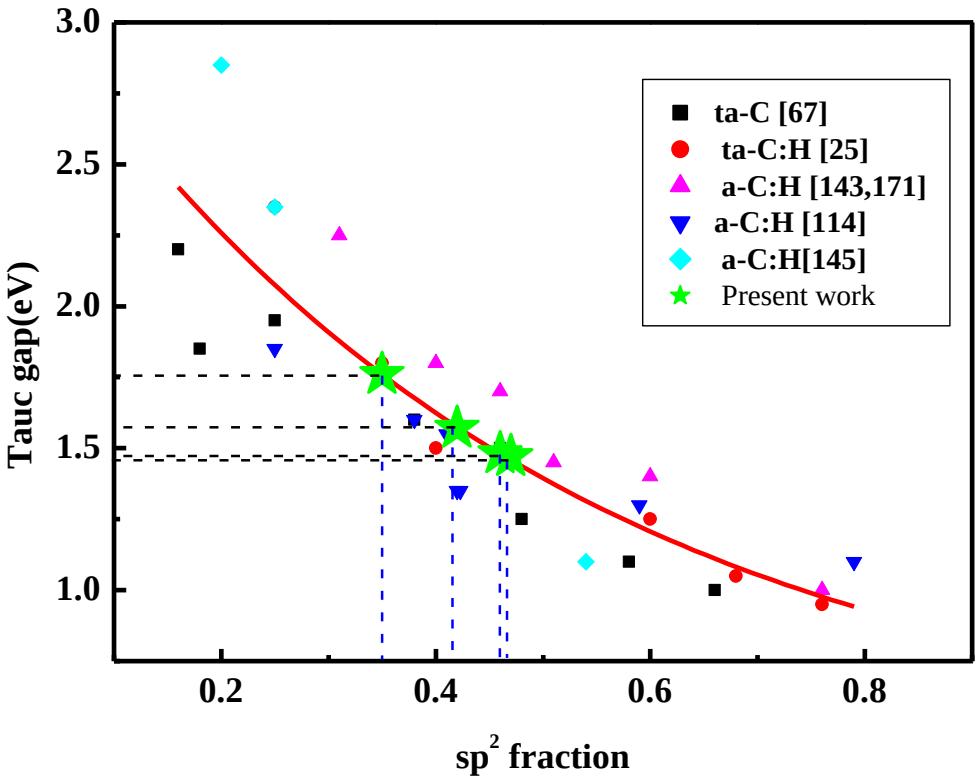

Figure 4.1.1.8 Variation of Tauc gap of DLC thin films with sp^2-fraction [145]

In the DLC film structure from the statistical data plots between Tauc gap (eV) and sp^2-fraction as shown in Fig. 4.1.1.8. Again from the obtained sp^2-fraction we can also estimate the density (gm/cm^3) of these DLC films as shown in Fig. 4.1.1.9. In each figure (Figure 4.1.5 to Figure 4.1.1.9), this present results are plotted with green star mark that are comparable with other literatures results. Moreover, all the parameters (obtained results) that we have obtained for DLC thin films deposited at different bias voltage in PECVD process from the Raman spectra are tabulated in table 4 given in the next page.

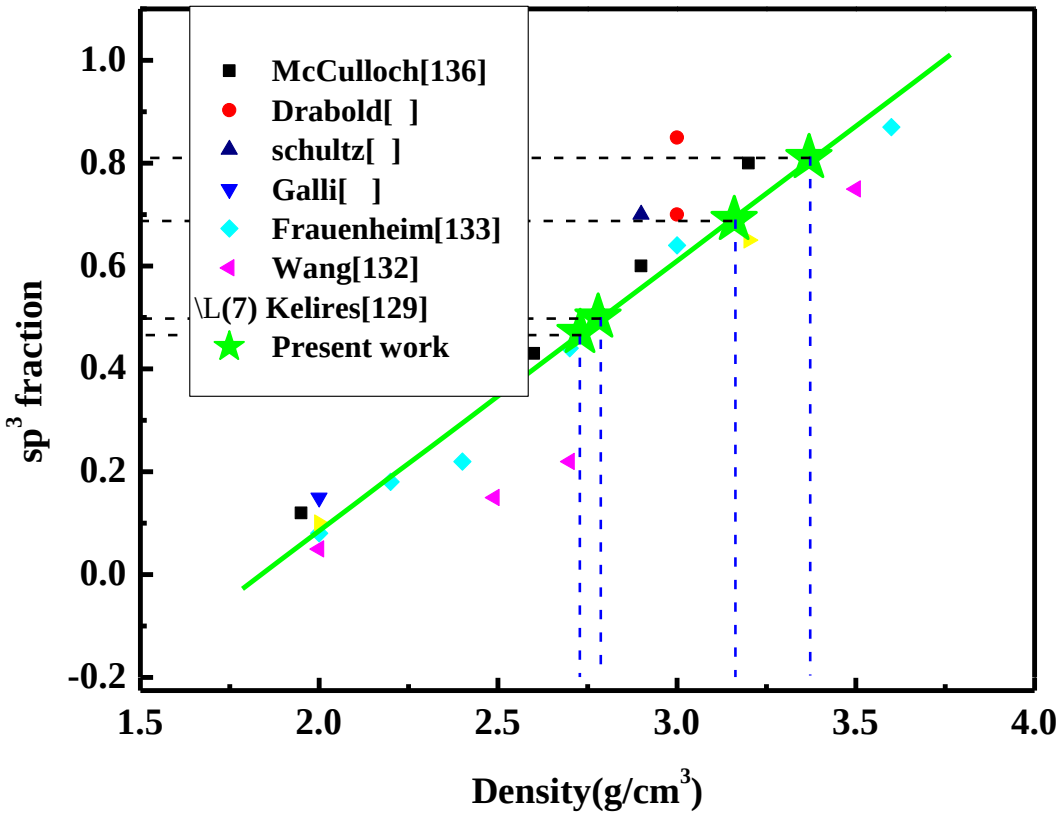

Figure 4.1.1.9 sp^3 fractions in function of density for different simulations of a-C networks. data from Kelires [129,130], Wang et al.[131], Jungnickel et al. [133], Drabold et al. [134], Galli et al. [137,138], Marks et al. [160,161], and McCulloch et al.[136].

We also estimated the stress of DLC films from the statistical data plots between stress (GPa) and sp^3 fraction as shown in Fig. 4.1.1.10 and tabulated in table 4. It shows that the stress of the DLC films increases with increase of bias voltage during deposition of the films**.**

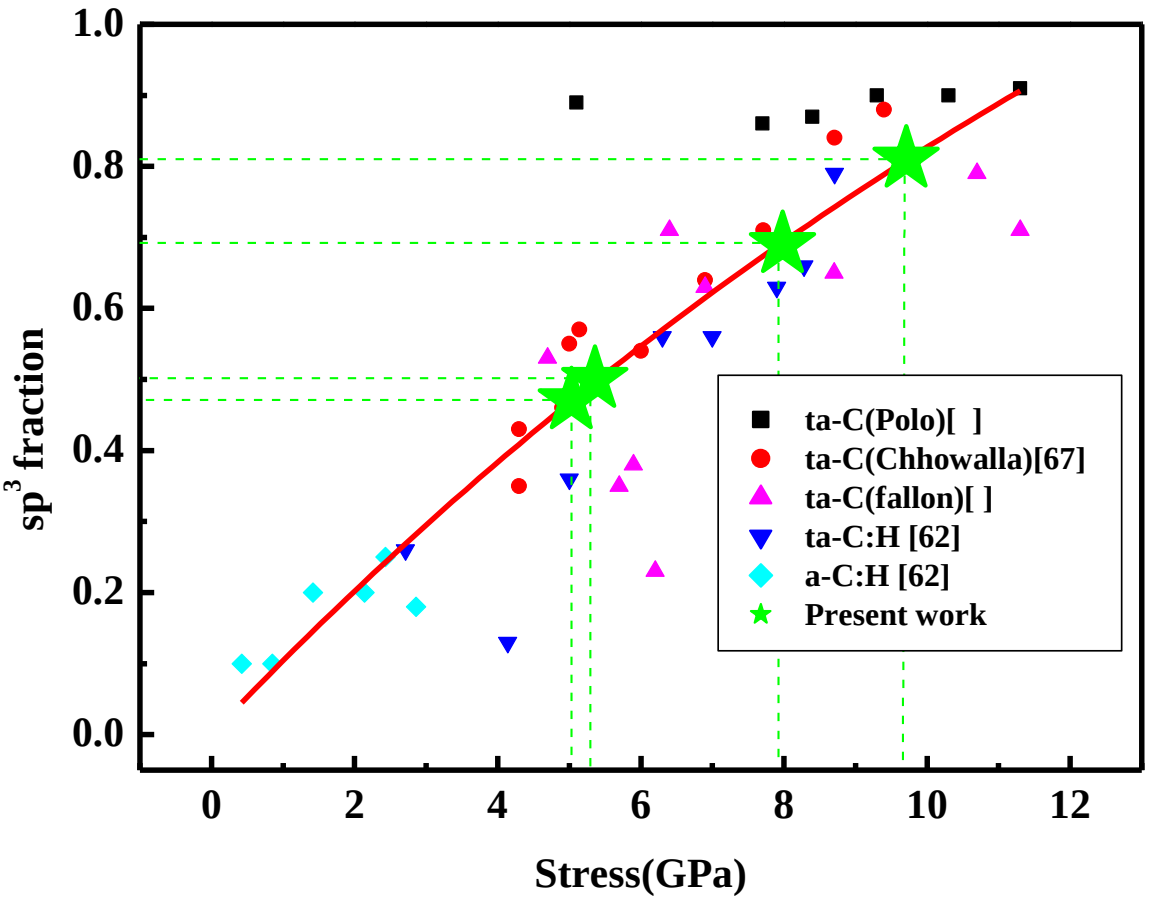

Figure 4.1.1.10 sp^3 fractions in function of stress for different ta-C and a-C:H films.

Table.4 Different parameters of DLC thin films obtained from the Raman spectra when excitation LASER wavelength λ_{exc} = 488 nm.

DLC films	G-peak width (cm^{-1})	I_D/I_G ratio	sp^3 (±0.05)	sp^2 (±0.05)	Density (gm/cm^3)	Tauc gap (eV)	Stress (GPa)
V_B = 100 V	136	0.65	0.47	0.47	2.73	1.47	5.03
V_B = 300 V	139	0.61	0.50	0.46	2.78	1.48	5.36
V_B = 400 V	147	0.47	0.69	0.42	3.16	1.57	7.98
V_B = 600 V	149	0.27	0.81	0.35	3.37	1.76	9.71

4.1.2 Raman spectroscopy of Silicon doped Diamond Like Carbon (DLC:Si)

There is great interest in doping Diamond-like carbon (DLC) films to manipulate their electronic properties. In this work, Si-doped DLC films are investigated.

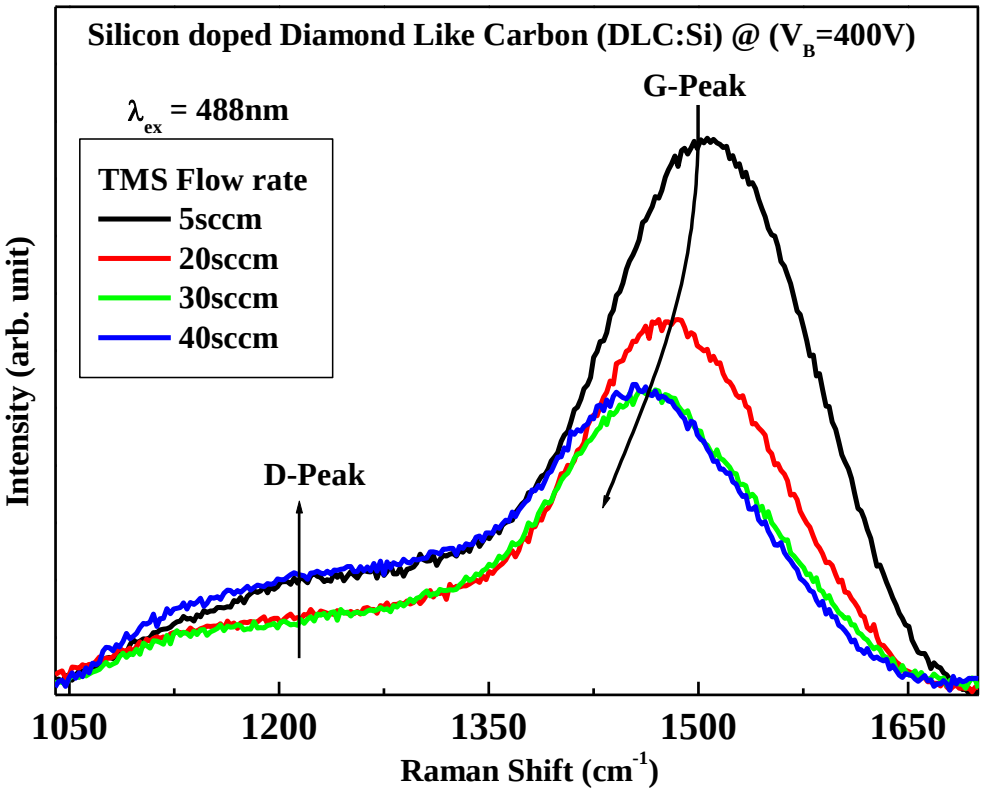

Figure 4.1.2.1 Raman Spectra of silicon doped DLC (DLC:Si) films deposited at different TMS flow rate with bias voltage 400 V [LASER excitation wavelength λ_{exc} = 488 nm]

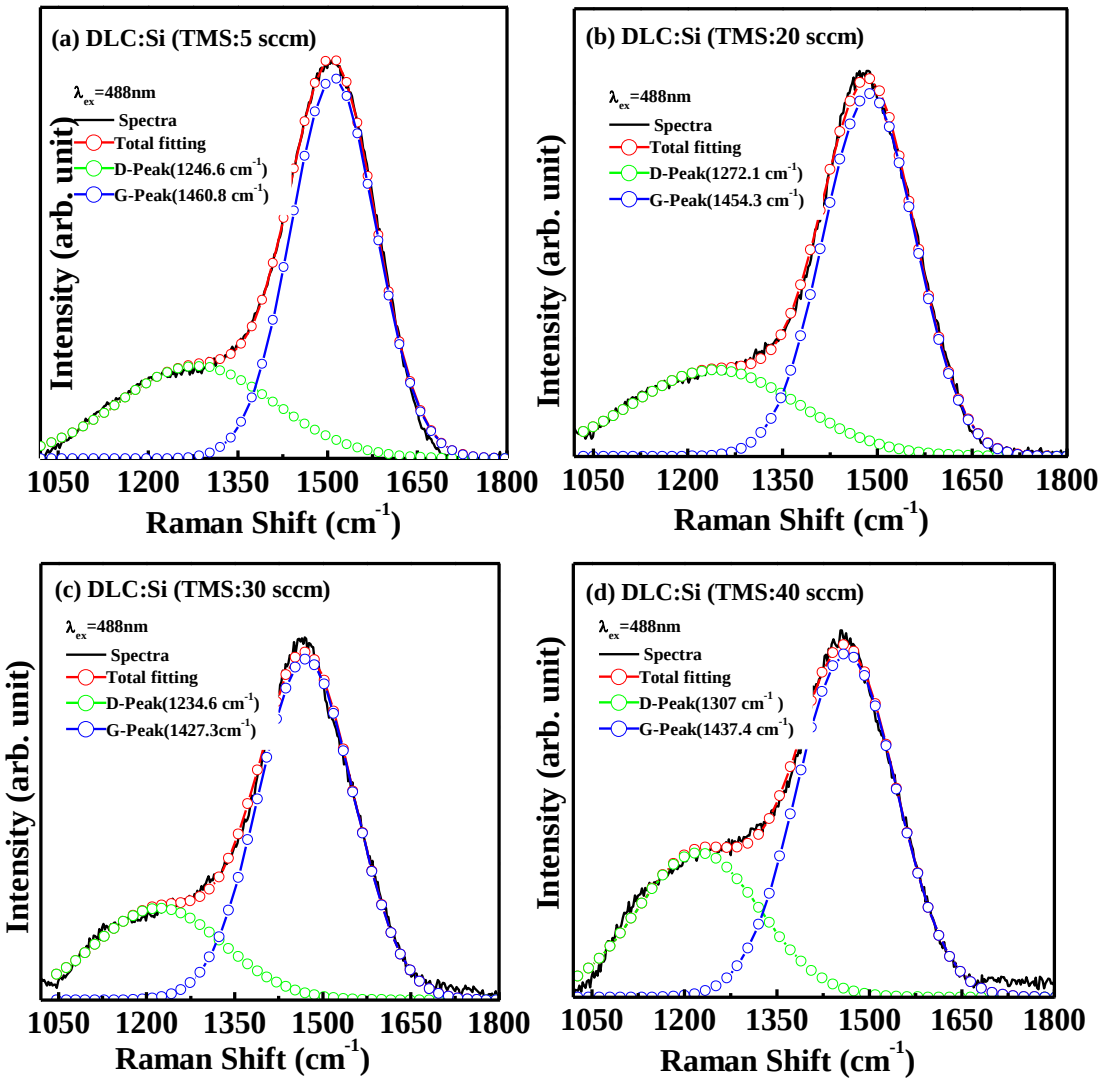

Figure 4.1.2.2 Deconvoluted into D-Peak and G-peak of Raman Spectra of DLC:Si films deposited at constant bias voltage (V_B= 400 V) and at different TMS flow rate (a) 5 sccm, (b) 20 sccm, (c) 30 sccm and (d) 40 sccm [λ_{exc}= 488nm]

The Silicon doped Diamond Like Carbon (DLC:Si) thin films dealt in this work were synthesized by the PECVD method on the Si <100> substrate at a bias voltage of 400 V [4]. The silicon dopant of where controlled at different concentration using different tetramethylsilane **(**TMS) flow rate (5-40 sccm) during deposition process along with C_2H_2. During the deposition process C_2H_2 is injected inside the deposition chamber at a flow rate of 20 sccm in Ar^+ atmosphere (10 sccm). The structural property is studied by the Raman spectroscopy using two different LASER excitation of wavelength *viz* 488 nm and 647 nm. Fig.4.1.2.1 shows the Raman spectra of silicon doped DLC films (DLC:Si) at different TMS flow rate (5-40 sccm) that are obtained at the LASER excitation wavelength of λ_{exc} = 488 nm. The deconvolution into G-peak and D-peak of each spectrum using Gaussian lines are also shown in figures 4.1.2.2(a-d).

In general the spectral features are similar but the G-peak is shifted towards lower Raman frequency when TMS flow increases from 5 sccm to 40 sccm during the deposition process. This shift in peak position was identified after deconvolution into D-peak and G-peak using two Gaussian peaks. The deconvoluted results are tabulated in table 5.

Table 5: Results obtained after decomposition Raman spectra of DLC:Si films into D-peak and G-peak when LASER excitation energy of wavelength (λ_{ex}) = 488 nm.

Sample DLC:Si	Peak Position		Width		I_D/I_G ratio
	D-Peak (cm^{-1})	G-Peak (cm^{-1})	W_D (cm^{-1})	W_G (cm^{-1})	From Area
TMS=5 sccm	1281	1510	259.2	143.3	0.44
TMS=20 sccm	1243	1487	263.0	146.3	0.42
TMS=30 sccm	1222	1471	219.4	161.0	0.37
TMS=40 sccm	1223	1463	199.1	162.0	0.51

It is also observed that the width of G-peak (FWHM) is increasing whereas the width of D-peak (FWHM) reduces on increasing of TMS flow rate. This change of G- peak positions and peak width indicates that the mechanical and tribological properties are changing. Due to increase of TMS flow rate changing from 5 sccm to 40 sccm during deposition process , the hydrogen contents increases along with incorporation of silicon in the DLC film structure. This causes the change of all those parameter that obtained from the Raman results and could be explained by the creation of disorder in the DLC:Si films structure. The ratio of I_D/I_G is also decreasing with increase of TMS flow up to 30 sccm and then increases at 40 sccm TMS flow during deposition process. This decrease of I_D/I_G ratio suggests that Si-doping diminishes the average size of the sp^2-bonded clusters and creates the sp^3 bonded clusters in the Si-DLC films. The development of sp^3 chemical bonds and the suppression of aromatic sp^2-bonded clusters on Si addition were also observed by Zhao et al. from the analysis of x-ray photoemission spectroscopy (XPS).

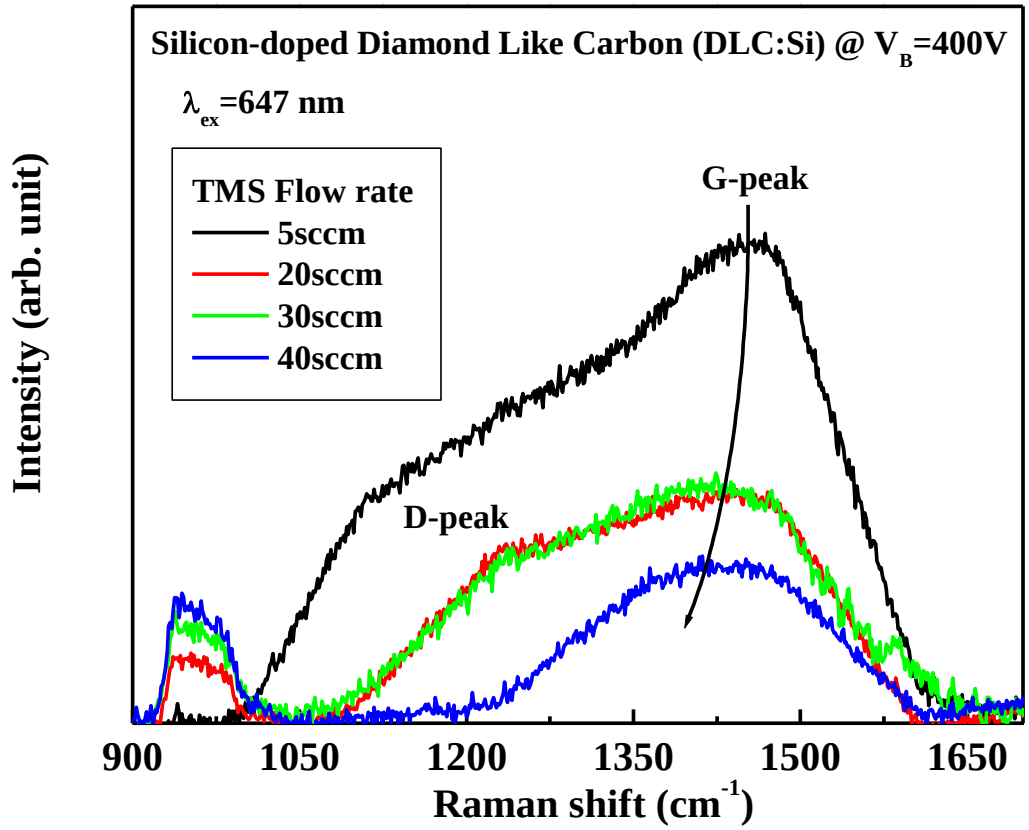

Figure 4.1.2.3 Raman Spectra of silicon doped DLC (DLC:Si) films deposited at different TMS flow rate with bias voltage 400 V [λ_{exc} = 647 nm]

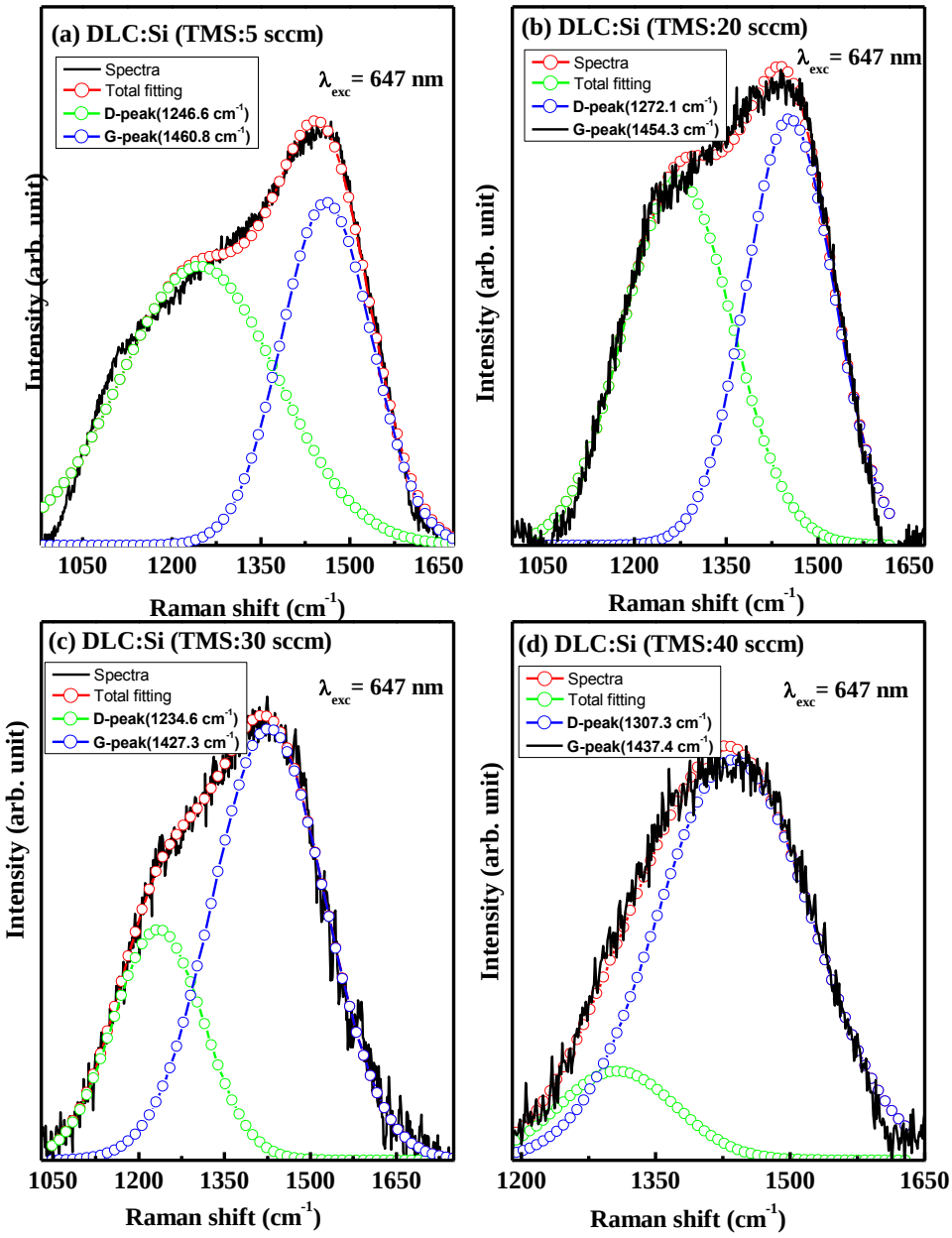

Figure 4.1.2.4 Deconvoluted into D-Peak and G-peak of Raman Spectra of DLC:Si films deposited at constant bias voltage (V_B= 400 V) and at different TMS flow rate (a) 5 sccm, (b) 20 sccm, (c) 30 sccm and (d) 40 sccm [λ_{exc}= 647 nm]

The Raman spectra of silicon doped DLC films (DLC:Si) at different TMS flow rate (5-40 sccm) obtained using the laser excitation wavelength λ = 647 nm has been studied as shown in Fig.4.1.2.3. The deconvolution into G-peak and D-peak of each spectrum using Gaussian function are shown in figures 4.1.2.4(a-d) and their results are tabulated in table 6. The fitted results (table 5) shows that the G-Peak shifted towards lower Raman frequency; whereas D-peak shifted towards higher Raman frequency with increasing tetramethylsilane (TMS) flow rate during deposition process. In the same time FWHM of the G-Peak increases; whereas D-peak width decreases. These results show an increase in the structural disorder and the clusters of sp^2 are converted in chains of sp^3 bonding in the Si-DLC film. It is also observed that the dispersion of G-peak is arises when laser excitation energy is changes from 1.91 eV (674 nm) to 2.42 eV (488 nm) and is caused by the resonant selection of sp^2 chains of variety sizes at different excitation energies.

Table 6: Results obtained after decomposition Raman spectra of DLC:Si films into D-peak and G-peak when LASER excitation energy of wavelength (λ_{ex}) = 647 nm.

Sample DLC:Si	Peak Position		Width		I_D/I_G ratio
	D-Peak (cm^{-1})	G-Peak (cm^{-1})	W_D (cm^{-1})	W_G (cm^{-1})	From Area
TMS=5 sccm	1246.6	1460.8	262.8	152.3	1.41
TMS=20 sccm	1272.1	1454.3	177.3	143.5	1.05
TMS=30 sccm	1234.6	1427.3	157.1	196.6	0.43
TMS=40 sccm	1307.3	1437.4	130.5	172.4	0.16

The decrease of I_D/I_G ratio for both excited energy shown in figure 4.1.2.5 confirms the samples become more diamond like carbon films on Si-doping. Si-doping decreases the average

size of the sp^2 clusters and creates the sp^3 bonded clusters in the Si-DLC films. It shows that at 40 sccm the I_D/I_G ratio is abruptly changed when an excited wavelength of 488 nm was used as shown in figure 4.1.2.5 with error bar.

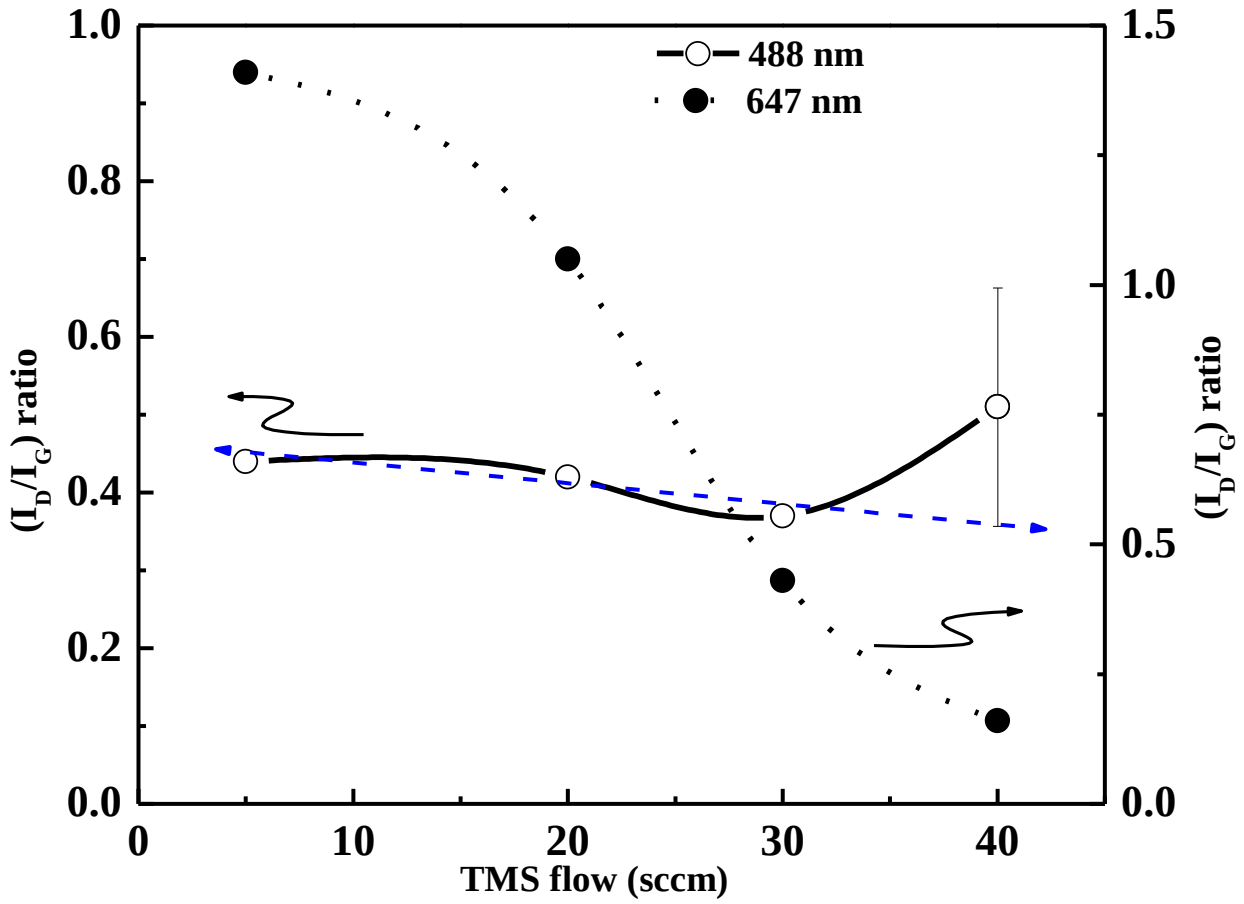

Fig. 4.1.2.5 (I_D/I_G) ratio (obtained from the D-Peak and G-peak area) with tetramethysilane (TMS) flow rate with excitation Laser wavelength λ_{exc} = 488 nm and λ_{exc} = 647 nm

However, these DLC and DLC:Si thin films deposited in PECVD method are good quality films and could be used in different application. In this further work, the parameters used

will be improved, the choice of the best substrate and the combination of compounds can give a superior quality of DLC thin films.

4.1.3 Nitrogen Doped amorphous carbon (a-CNx)

A few decades ago many studies were directed towards the addition of nitrogen to amorphous carbon (a-C) for two reasons; the synthesis of crystal of carbon nitride as a superhard compound (C_3N_4) [171] and the electronic doping of a-C. This work investigates the conversion of a-C and hydrogenated a-C (a-C:H) to good semiconductors by incorporating nitrogen. Meyerson and Smith [172] found that a-C:H could be doped n- and p-type by phosphorus and boron, respectively, in a same way to a-Si:H. They said that there was true substitutional doping by reversing the thermo-power sign because the conductivity varied from n- type to p-type [173]. Jones and Stewart [174] found that nitrogen increases the conductivity of a-C:H. This observation were collaborated by many other groups [174–180]. However, it is found that the increase of conductivity due to decrease of the band gap but no due to the shift in Fermi level [177]. In this present study, the Nitrogenated amorphous carbon thin films at different nitrogen concentration (at %) were prepared using pulsed laser deposition (PLD) system. The pulsed laser deposition (PLD) system composed of a Ti-sapphire laser (λ= 800 nm) with a frequency of 1 KHz and a full width at half maximum (FWHM) of 50 fs. The laser beam was directed to an angle of incidence of 45° to the target. The distance between the substrate and target was 4 cm. The depositions were carried out at room temperature. The preparation of the films depends on nitrogen pressure. The depositions run into the chamber were pumped down to nearly 9.8 $x10^{-6}$ mbar. A laser fluence of 0.64 J /cm^2 was spread to clean a graphite target (purity 99.999%). Nitrogen was deposited into the chamber with a mass flow controlling the background nitrogen pressure. Films were deposited at different nitrogen pressures ranging from $1x10^{-3}$ until 0.7

mbar. The deposition time for depositing these films was around 15 min and the thickness ranged around 150 nm for a-C with low nitrogen concentration (start by 0 - 4at.% N) and the thickness was nearly 95-115 nm when the higher nitrogen concentration (9 -17 at.% N) was used [178]. We have studied the microcrystalline structure of these films by Raman spectroscopy using two different excitation LASER wavelengths *viz*. 488 nm and 647 nm respectively. Fig.4.1.3.1 shows Raman spectra of nitrogen doped a-C films (a-CNx) with 488 nm excitation wavelength. It is very clear from the spectra and is that the spectra become more asymmetric when incorporated nitrogen at% is higher into the films structure. The intensity of the D-band becomes more intense with increase of nitrogen concentration in the film structure.

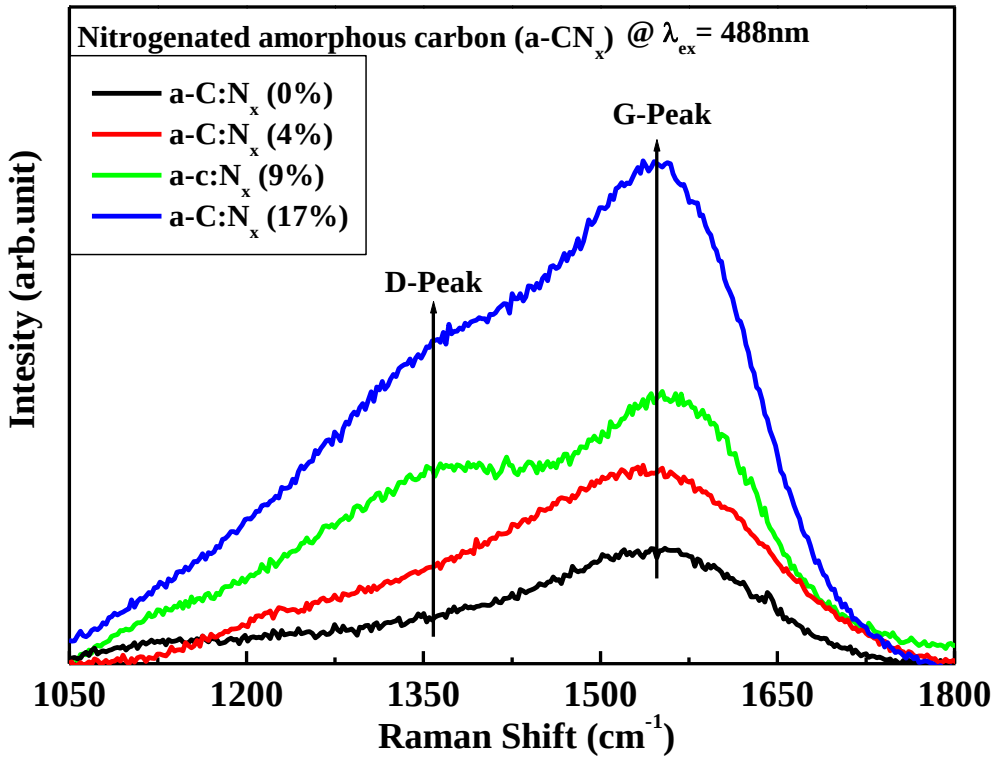

Fig. 4.1.3.1 Raman spectra of different at% N-doped amorphous carbon (a-CNx) obtained at the LASER excitation wavelength λ_{exc} = 488 nm

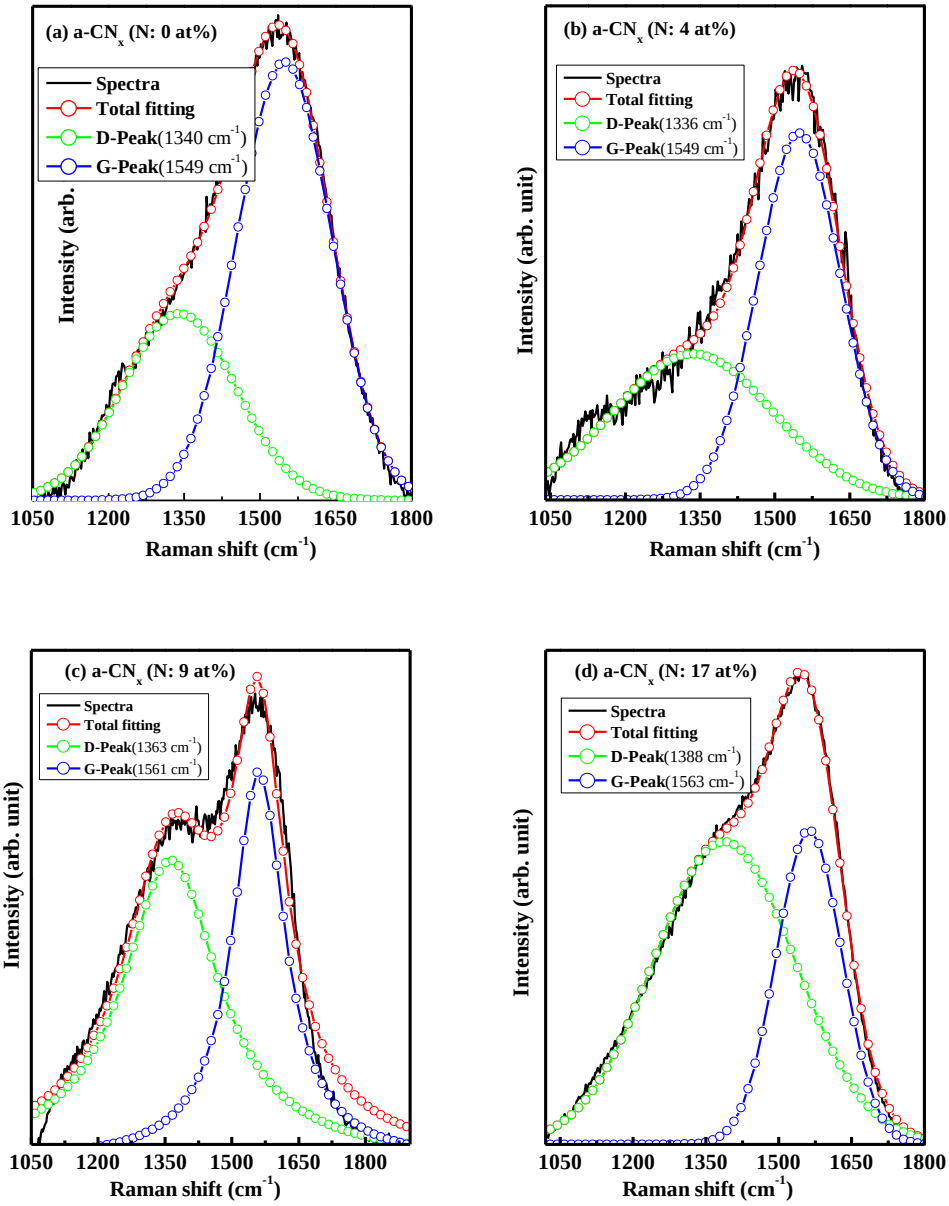

Figure 4.1.3.2 Deconvoluted into D-Peak and G-peak of Raman Spectra of a-CN_x films deposited at different nitrogen concentration (at %) (a) 0 at%, (b) 4 at %, (c) 9 at % and (d) 14 at % [λ_{exc}= 488 nm]

We have deconvoluted each spectrum into two Gaussian peaks using two Gaussian distributions and linear background to fit both the D-peaks and G peaks as displayed in Fig. 4.1.3.2 (a-d). The *G* band was located at 1580 cm^{-1} in the zone of E_{2g} mode and *D* band located at 1350 cm^{-1} in the zone mode A_{1g} , only appear in the presence of disorder. Then, the Raman spectra of nanocrystalline and amorphous carbon are influenced by *G* and *D* peaks which can vary their intensities, widths, and positions. The scattering of sp^2 sites was the one controlling the presence of *G* and *D* bands within *a*-C. Since the p states have a lower energy than the s states becoming much more polarizable. It has been reported that the sp^2 sites give a much larger Raman cross section (around 50–230 times larger than sp^3 sites) [179]. Raman spectra of carbon nitride films are divided in three different approaches, which created confusion. The first [180-183] approach reported that both the *D* and *G* peaks are fitted with two Gaussian distribution functions and a linear background. Breit–Wigner–Fano (BWF) and a Lorentzian [184,185] is the second approximation used for fitting of the *G* and *D* bands, respectively. The last approach [186, 187] is based on three Gaussian line shapes attributed to *D*, *G*, and nitrogen (N) bands, respectively. In this report, we have only used first approach for simplicity approach. The results of fitting procedure are shown on table 6 as functions of the nitrogen content in the films. The G-peak and D-peak positions are shifted at higher frequencies with increase of nitrogen concentration. The full width at half maximum (FHWM) of the G peak and D-peak is decreased and increased respectively indicating the formation of more and more graphitic a-CNx thin films. The I_D/I_G ratio also increases as a function of nitrogen that further confirms for the formation of more disorder films. An I_D/I_G ratio of 0.51 (0.43) was calculated for the film deposited without incorporated N_2. With increase of nitrogen to 17 at% we have observed the intensity ratio reaches the value of 2.01 (0.96). The G peak became narrower when they have more

incorporated the nitrogen content. Those are explained by the creation of large size of clusters in the a-C and are good agreement with the other researchers [8].

Table 7: Raman band Parameters obtained after deconvolution of Raman spectra of nitrogenated amorphous carbon films at different N-at% when excitation wavelength is λ_{ex}= 488nm.

Sample description	Peak Position		Width		I_D/I_G	
	D-Peak (cm^{-1})	G-Peak (cm^{-1})	W_D (cm^{-1})	W_G (cm^{-1})	From Area	From Height
DLC:N(0%)	1340	1549	225.4	187.0	0.51	0.43
DLC:N(4%)	1336	1549	320.0	165.7	0.77	0.40
DLC:N(9%)	1363	1561	264.7	144.0	1.44	0.77
DLC:N(17%)	1388	1563	291.5	135.1	2.01	0.96

We also studied the Raman spectra of Nitrogenated amorphous carbon films (a-CNx) at different concentration (N at %) using the laser excitation wavelength λ = 647 nm and is shown in Fig.4.1.3.3. The deconvolution into G-peak and D-peak of each spectrum using Gaussian lines are shown in figures 4.1.3.4(a-d) and their results are tabulated in table 7. The fitted results (table 7) shows that the G-Peak shifted towards lower Raman frequency; whereas D-peak shifted towards higher Raman frequency with increasing nitrogen concentration (N-at%) during deposition process. In the same time FWHM of G-Peak decrease; whereas D-peak width increases like previous results obtained when excitation wavelength was used 488 nm. These results indicating the disorder decrease and the amount of sp^2 clusters increases. It is also observed that the dispersion of G-peak is arises when laser excitation energy is changes from 1.91 eV (674 nm) to 2.42 eV (488 nm) .It is caused by the resonant selection at the different sizes of sp^2 chains using different excitation energies.

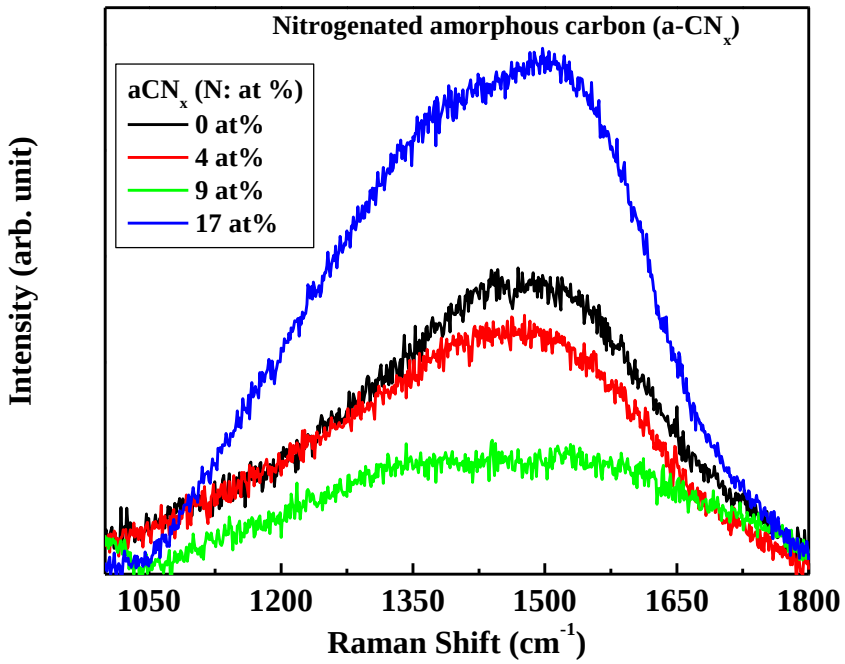

Fig. 4.1.3.3 Raman spectra of different at% N-doped amorphous carbon (a-CNx) obtained at the LASER excitation wavelength λ = 647nm

Table 8: Raman band Parameters obtained after deconvolution of Raman spectra of nitrogenated amorphous carbon films at different N-at% when excitation wavelength is λ_{ex}= 647 nm.

Sample description	Peak Position		Width		I_D/I_G	
	D-Peak (cm^{-1})	G-Peak (cm^{-1})	W_D (cm^{-1})	W_G (cm^{-1})	From Area	From Height
DLC:N(0%)	1209.5	1487.7	317.9	283.5	0.32	0.28
DLC:N(4%)	1333.4	1507.9	397.6	246.0	1.56	0.97
DLC:N(9%)	1350.5	1546.3	281.9	196.2	1.71	1.19
DLC:N(17%)	1355.4	1626.6	345.8	267.5	1.90	1.47

Table 8 shows the I_D/I_G ratio is proportional to nitrogen content at two excitation wavelengths. the number and size of sp^2 sites clusters increase when the I_D/I_G ratio also rise .

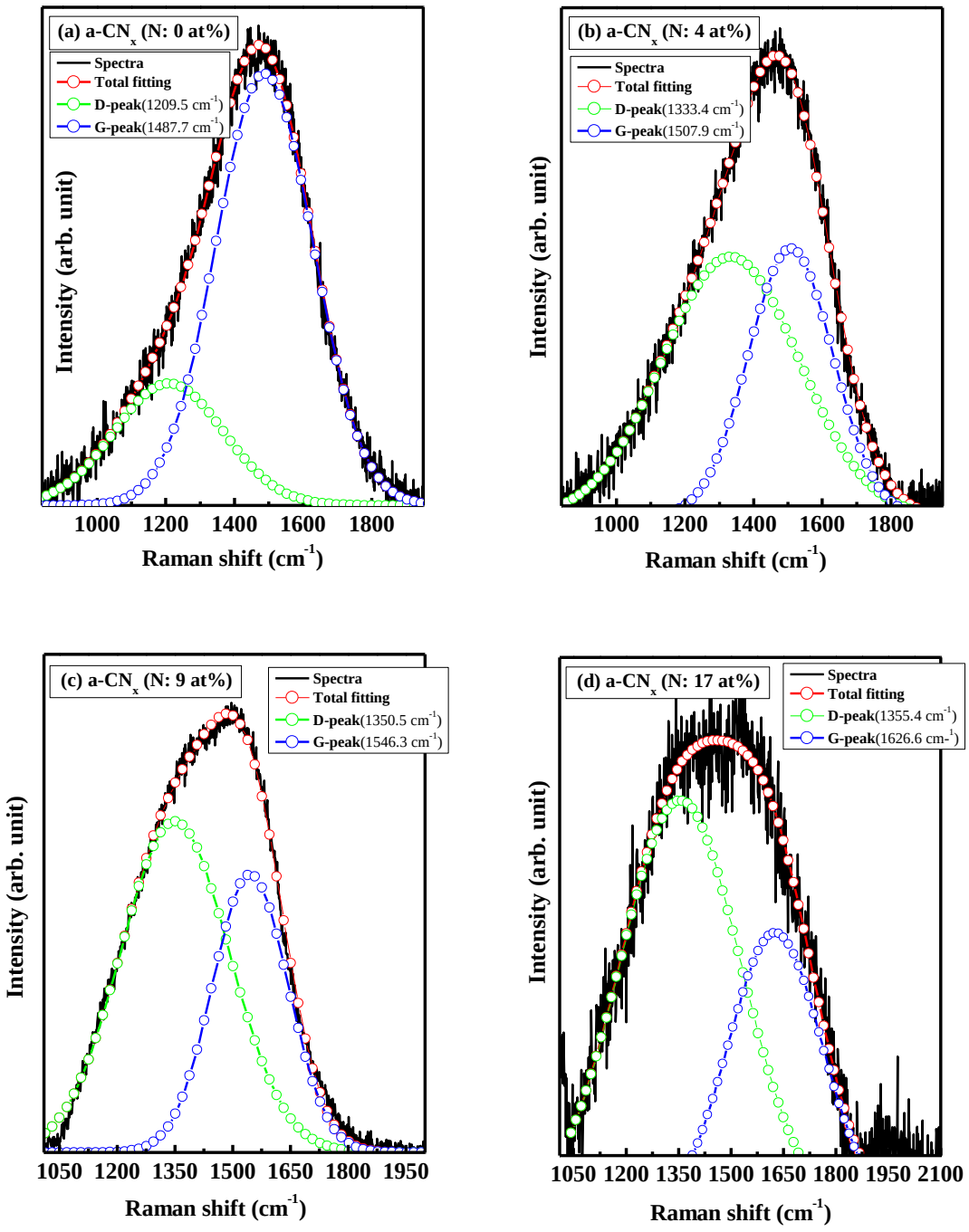

Figure 4.1.3.4 Deconvoluted into D-Peak and G-peak of Raman Spectra of a-CN$_x$ films deposited at different nitrogen concentration (at %) (a) 0 at%, (b) 4 at %, (c) 9 at % and (d) 14 at % [λ_{exc}= 647 nm]

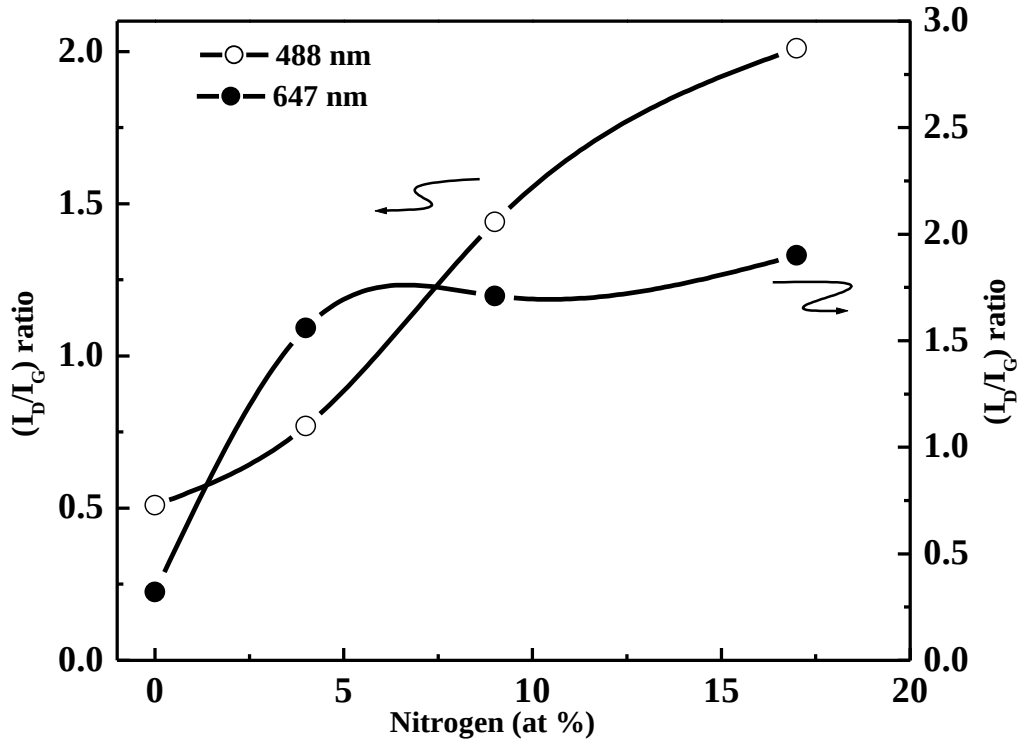

Fig. 4.1.3.5 (I_D/I_G) ratio (obtained from the D-Peak and G-peak area) with nitrogen concentration (at %) with excitation Laser wavelength λ_{exc} = 488 nm and λ_{exc} = 647 nm

4.2 Electrical properties of diamond like carbon (DLC) and amorphous carbon (a-C) films

Diamond-like carbon (DLC) and amorphous carbon thin films are groups of materials with high interest because of these numerous applications. Its properties are more influenced by the method of deposition and the deposition parameters. Obviously, the electrical properties of DLC films prepared by PECVD method is function of the preparation conditions. The electrical conductivity of DLC films is largely related to deposition conditions. The electrical properties also could be change by doping process. The obtained results about the electrical conduction of DLC and DLC: Si hetero-structures are described and discussed in the following sections. Both of them are different in properties from the electron transport through localised states in the DLC films. The conductivity could be increased using nitrogen doping in amorphous carbon films (a-CNx). Here, the voltage-current (V-I) relationships are studied for the DLC, DLC:Si and amorphous nitrogenated carbon (a-CNx) thin films. The voltage (V) and current (I) data were measured using 4140B pA Meter /DC voltage source interfaced to a computer via a locally designed LABVIEW software program. These measurements were carried out in a set of voltage varying and steps. In this work, we focused on the conductivity / resistivity behaviour of those thin films.

4.2.1 Voltage-Current (V-I) relationships of Diamond like carbon (DLC) thin films

As it is mentioned above that the conductivity of DLC films widely is dependent on the process parameters such as; deposition process, rf. power, substrate temperature and bias voltage. In this study, the DLC films are deposited under various bias voltage, starting from 100V - 600V in steps of 100 V by plasma enhanced chemical vapour deposition (PECVD) process.

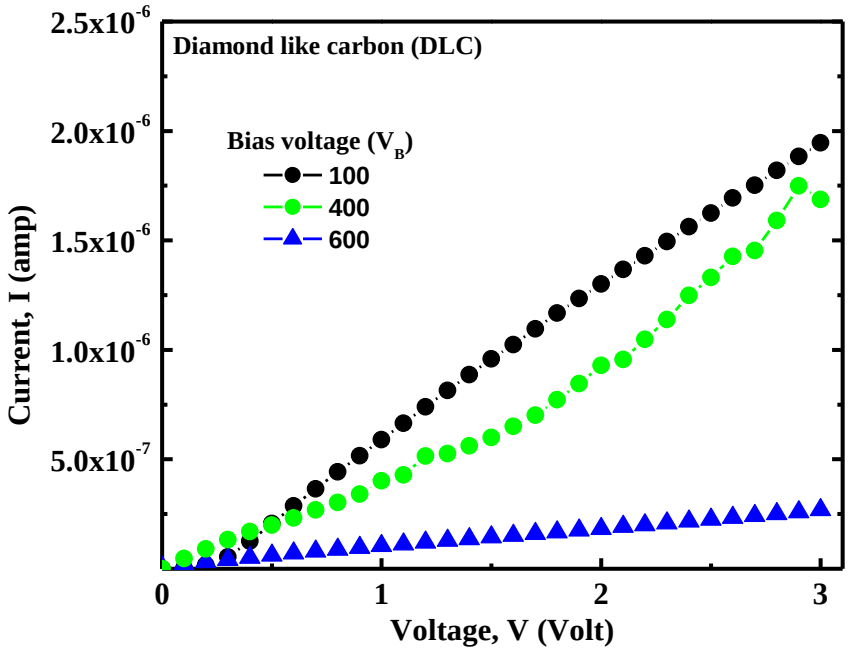

Fig.4.2.1.1 Current-Voltage characteristics of Au/DLC/Au structure for various bias voltage deposited DLC thin films (V vs I)

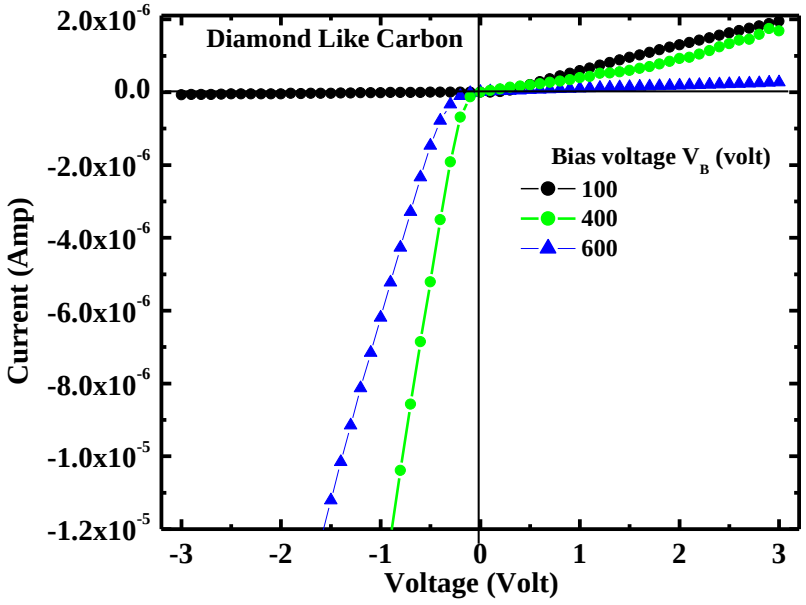

Fig.4.2.1.2 Current-Voltage characteristics of Au/DLC/Au structure for various bias voltage deposited DLC thin films (V vs I)

The voltage – current relationship of DLC films is presented in different ways as shown in Fig. Fig.4.2.1.1-4. In general, all presented V-I curve displayed that the conductivity diminishes when the bias voltage increase in the DLC films during deposition process. All the above figures clearly indicates that the DLC films becoming more and more sp^3-rich films when biasing voltage is increases gradually during deposition process and hence the conductivity is decreases gradually. The conductivity of DLC films is mainly depends on sp^2-content. Higher sp^2-content is responsible for high conductivity. We also observed in Raman spectroscopy results that I_D/I_G ratio decreases with increases of bias voltage i.e. increasing sp^3-content and hence decrease the conductivity is well agreed with this V-I results.

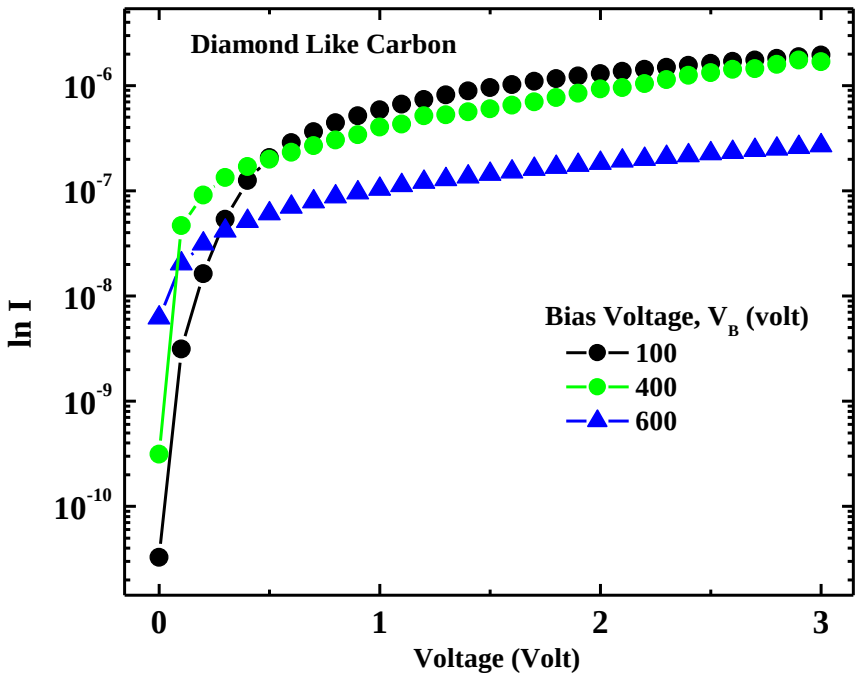

Fig.4.2.1.3 Current-Voltage characteristics of Au/DLC/Au structure for various bias voltage deposited DLC thin films [(V) vs ln (I)]

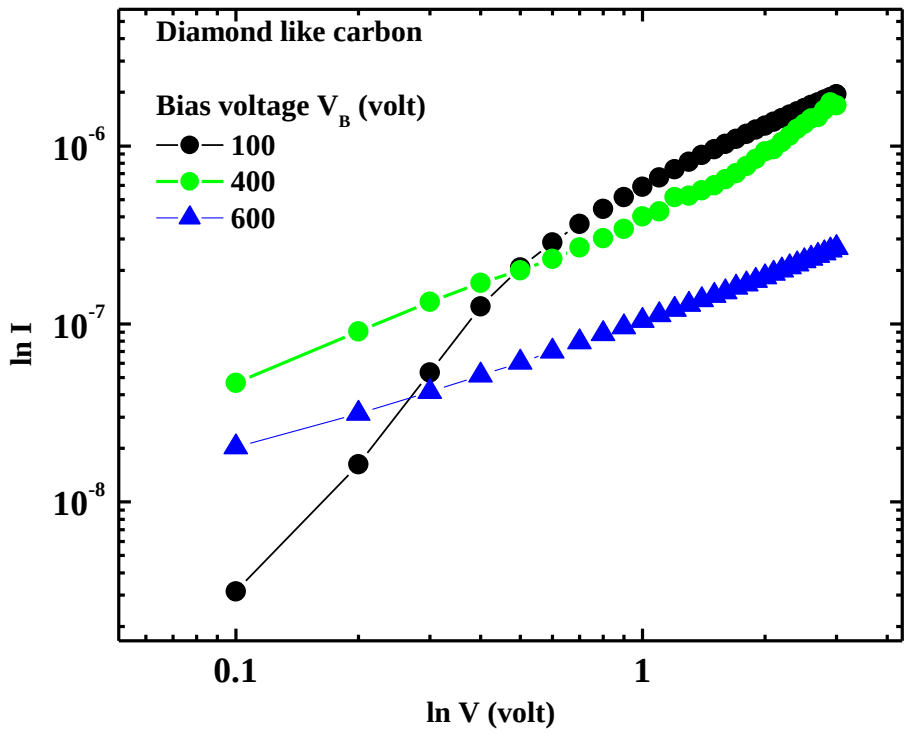

Fig.4.2.1.4 Current-Voltage characteristics of Au/DLC/Au structure for various bias voltage deposited DLC thin films [ln(V) vs ln (I)]

4.2.2. I-V Characteristic of Silicon doped DLC (DLC:Si)

The conductivity of Si doped DLC films is determined by the deposition ion energy process parameter such as, rf. power, substrate temperature, bias voltage. In this study the properties of DLC films deposited at 400V bias voltage and at different tetramethylsilane (TMS) flow rate for Si-doping in the film structure by the plasma enhanced chemical vapour deposition (PECVD) process are investigated.

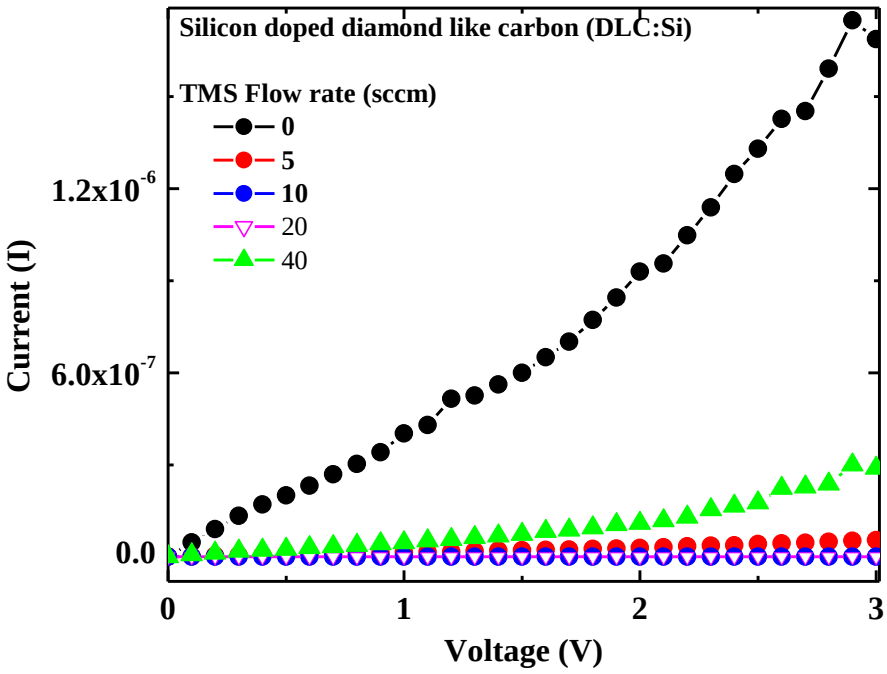

Fig.4.2.2.1 Current-Voltage characteristics of Au/DLC/Au structure for various TMS flow rates deposited DLC:Si thin films (V vs I)

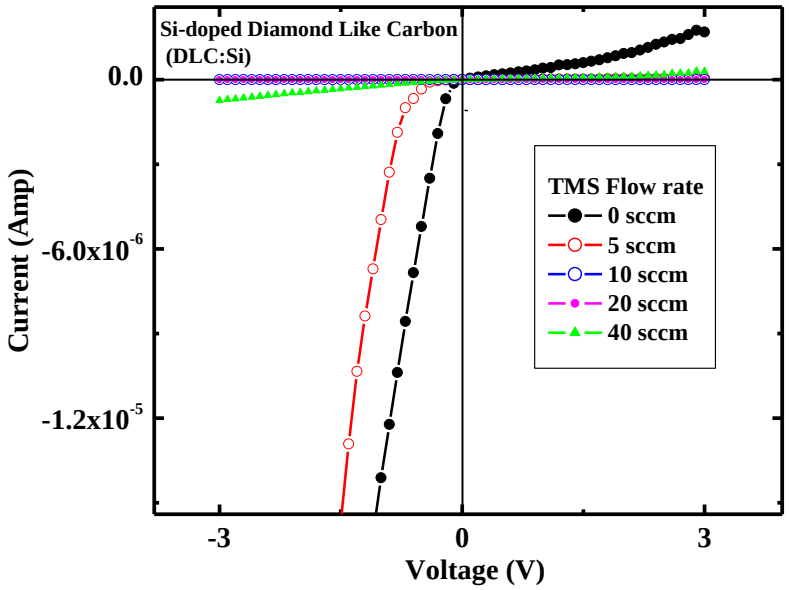

Fig.4.2.2.2 Current-Voltage characteristics of Au/DLC/Au structure for various TMS flow rates deposited DLC:Si thin films (I vs V)

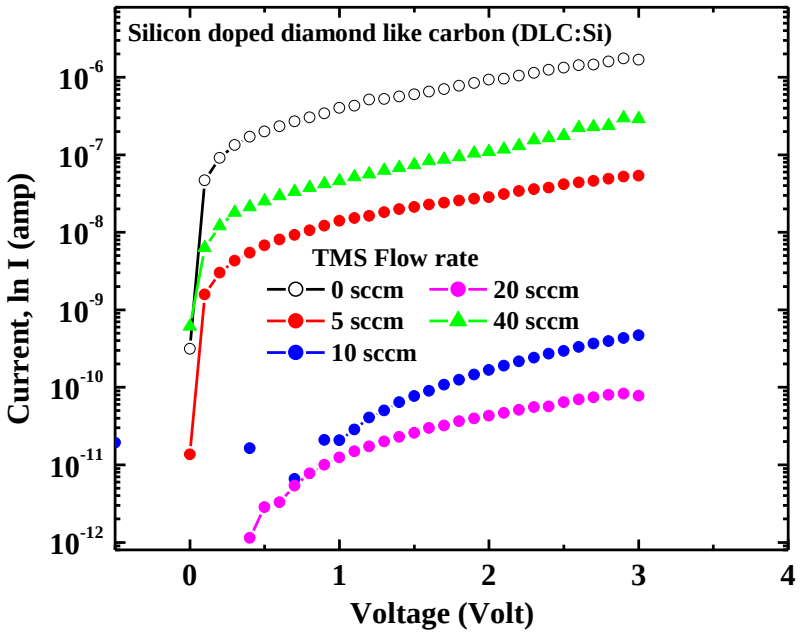

Fig.4.2.2.3 Current-Voltage characteristics of Au/DLC/Au structure for various TMS flow rates deposited DLC:Si thin films [(V) vs ln (I)]

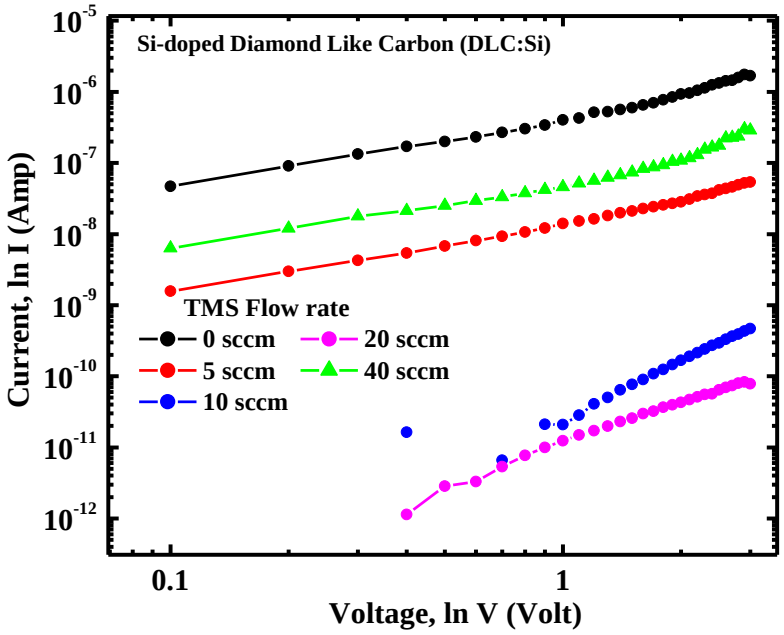

Fig.4.2.2.4 Current-Voltage characteristics of Au/DLC/Au structure for various TMS flow rates deposited DLC:Si thin films [ln(V) vs ln (I)]

It is observed from the I-V characteristics curve [see Fig. 4.2.2.(1-4)] that the conductivity of disordered Si-doped diamond-like carbon (DLC) thin films depend not only on properties of the conductive clustered sp^2 phase and the insulating sp^3 matrix (or sp^2/sp^3 ratio) but also on the presence of $Si–H_n$ and $C–H_n$ species in the film. In this earlier report [Ray et al. JJAP] It is found that there is an apparent crossover between space charge limited current (SCLC) and the Frenkel effect due to impurities incorporated during the fabrication of Si-DLC films. The flow of current occurs through tunneling from one conductive cluster (sp^2 C=C) to another separated by an insulating matrix (sp^3 C–C).

In the above figures the conductivity is decreases with increase of TMS flow rate up to 30 sccm but after that at 40 sccm the conductivity is slightly improved. The Si can have only sp^3 bonds, higher residual compressive stress could be expected when Si is incorporated into DLC. The compressive stress in the DLC films remaining due to increase of C-C sp^3 bond [188]. The number of C-C sp^3 bonds increased as the Si content increases, resulting in a lower conductivity.

4.2.3 I-V characteristic of nitrogen doped amorphous carbon (a-CNx) films.

Nitrogen-doped amorphous carbon films (a-C:Nx) were deposited on silicon by PLD process using different way of deposition with CH_4 and nitrogen. The structure and electrical properties of the films were studied upon incorporation of nitrogen. The electrical properties of a-C: Nx films can range between a semimetal to that of a insulator. We can obtain semiconductor behaviour when we have a mobility gap, but the high density of localized gap states conducts to low mobilities and significantly deteriorate the semiconducting properties of materials. The films have high electrical resistivities and have a large range of values, from 10^2 to 10^{16} Ω cm, depending on the deposition conditions.

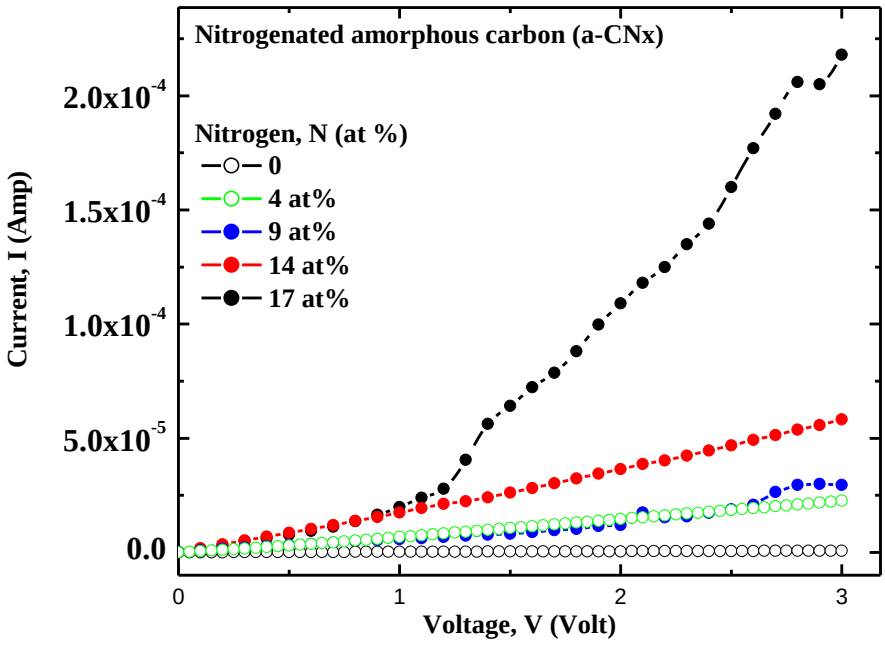

Fig.4.2.3.1 Current-Voltage characteristics of Au/DLC/Au structure for various atomic percentages deposited DLC:Si thin films (V vs I)

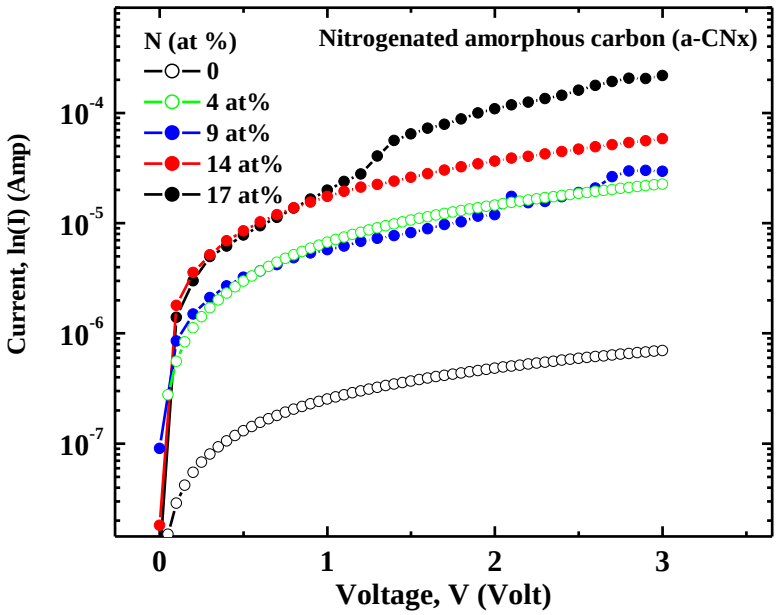

Fig.4.2.3.2 Current-Voltage characteristics of Au/DLC/Au structure for various atomic percentages deposited DLC:Si thin films [(V) vs ln(I)]

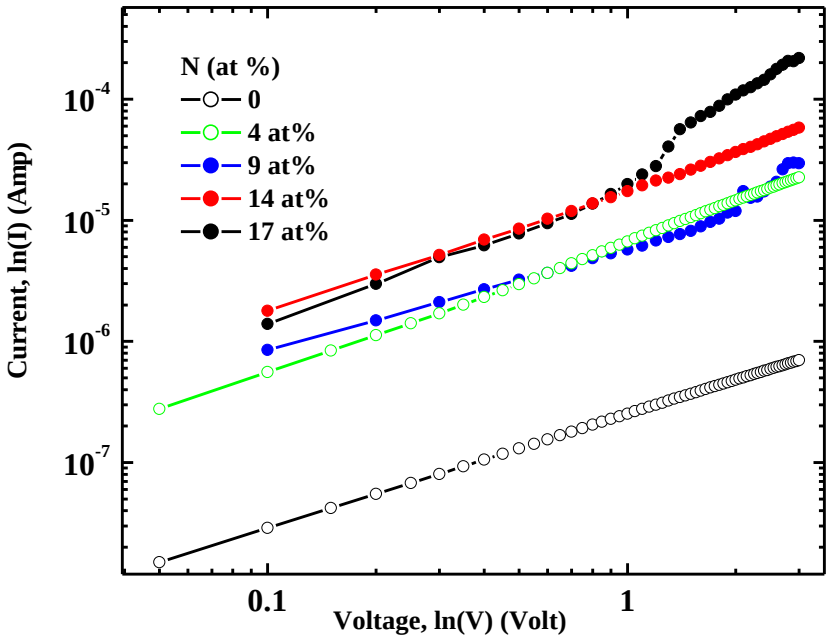

Fig.4.2.3.3 Current-Voltage characteristics of Au/DLC/Au structure for various atomic percentages deposited DLC:Si thin films [(V) vs ln(I)]

The electrical resistivity of amorphous carbon is mostly decreased by many orders of magnitude through doping with metals or nitrogen. It is well known that nitrogen doping in a-C films forms a n-type by changing the position of the Fermi from 0.91 eV above the valence band and 0.65 eV below the conduction band [189]. The measurement of electrical resistivity was done at room temperature by a two-point probe resistance measurement method. Fig.4.2.3.(1-3) shows the I-V characteristic of a-CNx thin films at different nitrogen concentration. Since from 0V to 3V the graphs are linear i.e the conductivity was obtained by using Ohm's law. As nitrogen (N at%) concentration increase, the current (the slope increase) also increase and it reaches the maximum at higher N-concentration. The conductivity of a-CNx thin films increase with the formation of sp^2 rings cluster due to the increase of localized hopping states. During nitrogen doping N–H, C–N, and C≡N bonds increased when the N_2 concentration is also

augmented. The creation of the C–N and C=N bond in the samples is at the basis of augmentation of the electrical conductivity [190]. Raman spectra revealed two peak D and G bands, and the D band was more strong than the G band. The optical band gap diminished when the N_2 concentration augments that further confirms for more conductive a-CNx film. The ratio of intensity of the D and G peak increases with higher nitrogen concentration, which explain by the more presence of sp^2 cluster [191] in this films and is responsible for the enhancement of conductivity of the a-CNx films. We conclude that at higher nitrogen concentration, a-C films show the augmentation of graphitic characteristics producing higher conductivity and optical band gap is found a narrow in our present study.

Chapter 5

Conclusion and proposed future work

The Raman parameters of DLC (a-C:H), silicon doped DLC (a-C:H:Si) and nitrogen doped amorphous carbon(a-C:N) obtained after deconvolution of each spectrum into D and G-peaks. It is observed that the sp^2-content for DLC (a-C:H) and Si-DLC films decreases and increases the number of sp^3 hybridized carbon atoms when bias voltage (V_B) increases. This result implies the formation of more diamond like carbon films collaborative with the decrease in conductivity. In case of DLC:Si films, the films becoming more diamond like carbon when TMS flow rate increases from 0 – 30 sccm and after that at 40 sccm flow rate the films become slightly graphitic in nature because the number of sp^2 hybridized carbon atoms slightly increases and hence formation of graphite DLC films. The increase silicon concentration decreases I_D/I_G ratio and convert sp^2 clusters to sp^3 chains presumably the formation of SiC compound and nanostructures with increasing Si concentration. In case of a-CNx films the sp^2-content increases with increases of nitrogen doping and becoming more graphitic in nature that reveals the improvement of conductivity.

The electrical conductivity of DLC films is found to decrease with an increase in the bias voltage. This decrease has been attributed to the formation of higher number of sp^3-hybridized carbon atoms in the film structure networks with increasing Si-doping concentration. When bias voltage increases during deposition process of DLC films, sp^3 hybridized carbon atoms increases. As consequence (a result) the conductivity decreases gradually with the bias voltage. These results are consistent with the stress (GPa) estimated from the statistical data plotted with sp^3 versus stress as shown in figure 4.1.1.10 as discussed above. In this figure our results are

highlighted and compared with the other stress value obtained by different researchers. Again, when silicon is doped in DLC films, then sp^2 hybridized carbon atom converted into sp^3 hybridized carbon atom and the samples becoming more DLC; However nitrogen doping in amorphous carbon sp^3 hybridized carbon atom converted into sp^2 hybridized carbon atom and the films become more graphite in nature and hence the conductivity increases significantly.

In future we will propose to measure and study scanning electron microscopy (SEM) and X-Ray diffraction (XRD) for surface morphology .Further ,we will also propose to measure X-Ray photoemission spectroscopy (XPS) for the study of the electronic and bonding structure of these materials. At the end, we will determine the fraction of hydrogen in each sample.

REFERENCES

1. Robertson, J. Diamond-like amorphous carbon, *Materials Science and Engineering R,* vol. no. 37.4-6, May 2002, pp. 129-281.
2. IUPAC Compendium of Chemical Terminology 2nd edition (1997).
3. Carey, J.D. and Silva, S.R.P. Conditioning of hydrogenated amorphous carbon thin films for field emission current stressing, *Appl. Phys. Lett.* vol. no. 78.3, Oct. 2001, pp. 347-349.
4. Papakonstantinou, P. Zhao, J. F. Lemoine, P. McAdamand, E.T. Mclaughlin, J.A. The effects of Si incorporation on the electrochemical and nanomechanical properties, *Diam. and Rel. Mater*, vol. no. 11.(3-6), March-June 2002, pp. 1074-1080.
5. McCann, R. Roy, S.S. Papakonstantinou, P. McLaughlin, J.A. and Ray, S.C. Spectroscopic analysis of a-C and a-CN_X films prepared by ultrafast high repetition rate pulsed laser, *Journal of Applied Physics*, Vol. no. 97.7, Jan. 2005, pp. 073522-073533.
6. Ray, S.C. Pao, C.W. Tsai, H.M. Chiou, J.W. Pong, W.F. Tsai, M.H. Okpalugo, T.I.T. Pakontantinou, P. Pi, T.W. Pi, J.A. Enhancement of sp^3-bonding in high-bias-voltage grown diamond-like carbon thin films studied by x-ray absorption and photoemission spectroscopy. *J. Phys. Condens. Matter*, vol. no. 19.17, April 2007, pp. 176204-176209.
7. Ray, S.C. Pao, C.W. Tsai, H.M. Chiou, J.W. Jan, J.C. Krishna Kumar, K.P. Pong, W.F. Wang, W.J. Hsu, C.J. OKpalugo, T.I.T. Papakontantinou, P. and MaLaughlin, J.A. Electronic structure and bonding properties of Si-doped hydrogenated amorphous carbon films. *Appl. Phys. Lett*, vol. no. 85.18, Nov. 2004, pp. 4022-4024.
8. Ray, S.C. Pao, C.W. Chiou, J.W. Tsai, H.M. Jan, J.C. Pong, W.P. McCann, R. Roy, S.S. Papakonstantinou, P. and McLaughlin, J.A. Electronic properties of a-CN_X thin films: An X-ray

absorption and photoemission spectroscopy study. *Journal of Applied Physics*, vol. no. 98.3, Aug. 2005, pp. 033708(1-4).

9. Spitsyn, B.V. Derjaguin, B.V. Author's Certificate July10 (1956); USSR Patent, vol. 339134, May 5 (1980).
10. Eversole, W. US Patents, vol. 3030187 and 3030188 (1962).
11. Angus, J.C. Will, H.A. Stanko, W.S. Growth of diamond seed crystals by vapour deposition. *J. Appl. Phys*, vol. no. 39.6, May 1968, pp. 2915-2922.
12. Field, J.E. Properties of Diamond, Academic press, London 1993.
13. Celi, F.G. Butler, J.E. Diamond Chemical Vapor Deposition. *Ann. Rev. Phys. Chem*, vol. 42, Oct. 1991, pp. 643-684.
14. Dresselhau, M.S. Dresselhaus, G. Ekhund, P.C. Science of Fullerenes and carbon nanotubes, Academic Press, London, vol. no. 41.3, January 1996, pp.352
15. Kelly, B.T. Physics of graphite. *Journal of Nuclear Materials*, vol. no. 114.1, Feb. 1983, pp 116.
16. Green, D.C. Mckenzie, D.R. Lukins, P.B. The Microstructure of carbon thin films, *Mater. Sci. Forum*, vol. 52-53, 1989, pp.103-124.
17. Enke, K. Some new results on the fabrication of and the mechanical, electrical and optical properties of i-carbon layers. *Thin Solid Films*, vol. no. 80. (1-3), June 1981, pp. 227-234
18. Zele, J. Low-stress diamond-like carbon films. *J. Vac. Sci. Technol. A*, vol. no. 1.2, 1983, pp. 305-307.
19. Jacob, W. Möller, W. On the structure of thin hydrocarbon films. *Appl. Phys. Lett*, vol. no. 63.13, Sept.1993, pp. 1771-1773.
20. Mckenzie, D.R. Tetrahedral bonding in amorphous carbon. *Rep. Prog. Phys*, vol. no. 59.12, Dec.1996, pp. 1611-1664.

21. Koidl, P. Wagner, P.L.C. Dischler, B. Wagner, J. Ramsteiner, M. Properties and structure of amorphous hydrogenated carbon films, *Mater. Sci. Forum*, vol.52-53, 1990, pp. 41-70.
22. Weiler, M. Satte, S. Jung, K. Ehrhard, H. Veerasamy, V.S. Robertson, J. Highly tetrahedral, diamond-like amorphous hydrogenated carbon prepared from a plasma beam source, *Appl. Phys. Lett.*, vol. no. 64.21, May 1994, pp.2797-2799.
23. Fanchini, G. Ray, S.C. Tagliaferro, A. Optical properties of disordered carbon-based materials. *Surface and Coatings Technology*, vol. 151 –152, March 2002, pp. 233–241.
24. Fanchini, G. Ray, S. C. Tagliaferro, A and Laurenti, E. Density and capture radius of 'defects': quenching of the luminescent states in non-nitrogenated and nitrogenated amorphous carbon thin films. *J. Phys.: Condens. Matter*, vol. 14, Nov**.** 2002, pp.13231–13240
25. Davis, C.A. Veerasamy, V.S. Amaratunga, G.A.J. Milne, W.L. McKenzie, D.R. Properties of tetrahedral amorphous carbon films deposited in a filtered cathodic arc in the presence of hydrogen. *Philos. Mag. B*, vol. no. 69.6, Sept.2006, pp. 1121-1131.
26. Rengan, A. Narayan, J. Jahnke, C. Bedge, S. Park, J.L. Li, M. Characteristics of diamond-like carbon films formed by a hybrid laser-plasma ablation of graphite. *Mater. Sci. Eng. B.* vol. no.15.1, Oct. 1992, pp. 15-24.
27. Godet, C. Conway, N.M. Bourre, J.E. Bouamra, K. Grosman, A. ortega, C. Structural and electronic properties of electron Cyclotron plasma deposited hydrogenated amorphous carbon and carbon nitride films, *J. Appl. Phys*. vol. no. 91.7, April 2002, pp. 4154-4162.
28. Aisemberg, S. Chabot, R. Ion-Beam deposition of thin films of diamond-like carbon, *J. Appl. Phys.* vol. no. 42.7, June 1971, pp.2953-2958.
29. Spencer, E.G. Schmidt, P.H. Joy, D.C. Sansalone, E.J. Ion-beam-deposited polycrystalline diamond like films, *Appl. Phys. Lett.* vol. no. 29.2, July 1976, pp. 118-120

30. Whitmell, D.S. Williamson, R. The deposition of hard surface layers by hydrocarbon cracking in a glow-discharge. *Thin solid Films*, vol. no.35.2, June 1976, pp.255-261.
31. Holland, L. Ojha, S.M. The growth of carbon films with random atomic structure ion impact damage in hydrocarbon plasma, *Thin Solid Films*, vol. no.58.1, March 1979, pp. 107-116.
32. Angris, J.C. Koidl, P. and Domitz, S Plasma deposited thin films, eds. Mort, J. and Jansen, F. (CRC Press. Beca. Reton, Florida) 1986, pp.189
33. Wei, Q. Narayan, J. Superhard diamondlike carbon: preparation, theory, and properties, *Int. Mat. Rev*., vol. no.45.4, April 2000, pp.133-164.
34. Lifshitz, Y. Kasi, S.R. Rabalais, J.W. Eckstein, W. Substantiation model for film growth from hyperthermal species. *Phys. Rev. B*, vol. no. 41.15, May 1990, pp.10468-10480.
35. Lifshitz, Y. Lempert, G.D. Grossman, E. Substantiation of subplantation model for diamond-like film growth by atomic microscopy, *Phys, Rev. Lett*, vol. no.72.17, April 1994, pp.2753-2756.
36. Hofsäss, H. Binder, H. Klumpp, T. Recknagel, E. Doping and growth of diamond-like carbon films by ion beam deposition, *Diamond. Rel. Mater*, vol. no. 3.(1-2), Jan.1994, pp.137-142.
37. Jansen, F. Machonkin, M. Kaplan, S. Hark, S. The effects of hydrogenation on the properties of ion beam sputter deposited amorphous carbon. *J. Vac. Sci. Techno*l. A, vol. no.3.3, May 1985, pp.605-609
38. Rubin, M. Hopper, C.B. Cho N. H. and Bhushau, B. Optical and mechanical properties of dc sputtered carbon films, *Journal of materials Research*, vol. no. 5.54, Nov.1990, pp. 2538-2542.
39. Lieberman, M. A. Lichtenberg, A.J. Principles of plasma Discharges and Materials Processing, Wiley, New York, 1994.

40. Koidl, P. Wagner, C. Dischler, B. Wagner, J. Ramsteiner, M. Plasma deposition, Properties and structure of amorphous hydrogenated carbon films, *Mater. Sci. Forum*, vol.52-53, 1991, pp.41-70.
41. Müller-Sebert, W. Wörner, E. Fuchs, F. Wild, C. Koidl, P. Nitrogen induced increase of growth rate in chemical vapour deposition of diamond. *Appl. Phys. Lett,* vol. no.68.6, Feb. 1996, pp.759-760.
42. Wild, C. Koidl. P. Ion and electro-dynamics in the sheath of radiofrequency glow discharge, *J. Appl. Phys,* vol. no. 69.5, March 1991, pp.2909-2922.
43. Weiler, M. Sattel, S. Giessen, T. Jung, K. Ehrhardt, H. Veeramy, V.S. Robertson, J. Preparation and properties of highly tetrahedral hydrogenated amorphous carbon, *Phys. Rev. B*, vol. no.53.3, January 1996, pp. 1594-1608.
44. Martinu, L. Raveh, A. Boutard, D. Houle, S. Poitras, D. Vella, N. Weitheimer, MR. Properties and stability of diamond-like carbon films related to bonded and unbonded hydrogen. *Diamond. Rel. Mater*. vol.no. 2.(5-7), April 1993, pp. 673-677.
45. Zarrabian, M. Fourches-Coulon, N. Turban, G. Observation of nanocrystalline diamond in diamond-like carbon films deposited at room temperature in electron cyclotron resonance plasma, *Appl. Phys. Lett*., vol. no 70.19, May 1997, pp. 2535-2537.
46. He, X.M. Lee, S.T. Bello, I. Cheung, A.C Lee, C.S. Characterization and optical properties of diamondlike carbon prepared by electron cyclotron resonance plasma, *J. Mater. Res*, vol. no.14.3, January 2001, pp.1055-1061.
47. Weiher, M. Lang, K. Li, E. Robertson, J. Deposition of tetrahedral hydrogenated amorphous carbon using a novel electrons cyclotron wave resonance reactor. *Appl. Phys. Lett,* vol. no. 72.11, March 1998, pp.1314-1316.

48. Voevodin, A. A. Donley, M.S. Preparation of amorphous diamond-like carbon by pulsed laser deposition: a critical review, *Surf. Coat. Techn*. vol. no. 82.3, Aug. 1996, pp.199-213.
49. Davanloo, F. Juengerman, E.M. Jander, D.R. Lee, T.J. Collins, C.B. Amorphic diamond films produced by a laser plasma source, *J. Appl. Phys*, vol. no. 67.4, February 1990, pp.2081-2087.
50. Lossy, R. Pappas, D.L. Roy, R. A. Cuomo, J. J. and Sura, V. M. Filtered arc deposition of amorphous diamond. *Appl. Phys. Lett*, vol. no. 61.2, July 1992, pp.171-173.
51. Xiong, F. Chang, Y.Y. Chong, R.P.H. Complex dielectric function of amorphous diamond films deposited by pulsed-excimer-laser ablation of graphite, *Phys. Rev. B.* vol. no. 48.11, Sept. 1993, pp.8016-8023.
52. Kovarik, P. Bourdon, F.B.D. Prince, R.H. Electron-energy-loss characterization of laser deposited a-C, a-C:H, and diamond films, *Phys. Rev. B*, vol. no. 48.16, Oct. 1993, pp.12123-12129.
53. Huai, Y. Chaker, M. Brougghton, J.N. Gat, E. Pipin, H. Gu, T. Bran, X. Sutton, M. Study of density in pulsed-laser deposited amorphous carbon films using x-ray reflectivity, *Appl. Phys. Lett* , vol. no. 65.7, Aug. 1994, pp.830-832.
54. Siegal, M.P. Barbour, J.C. Provencio, P.N. Tallant, D.R. Friedmann, T.A. Amorphous tetrahedral diamond-like carbon layered structures resulting from film growth energetics, *Appl. Phys. Lett*, vol. no. 73.6, Aug. 1998, pp.759-761.
55. Siegal, M.P. Martinez-Miranda, L.J. Dinardo, J.N. Tallent, D.R. Barbour, J.C. Provencio, P.N. Ultrahard carbon nanocomposite films in High Powered Laser Ablation, Spie, Dec.1998.
56. Merkulov, V.I. Lowndes, D.H. Jellison, G.E. Puretzky, A.A. Geohegan, D.B. Structure and optical properties of amorphous diamond films by ArF laser ablation as a function of carbon ion kinetic energy, *Appl. Phys. Lett.*, vol. no. 73.18, Nov. 1998, pp.2591-2593.

57. Robertson, J. Diamond-Like Carbon, *Pure. Appl. Chen.* vol. no.66.9, April 1994, pp.1789-1796.
58. Lifshitz, Y. Kasi, S.R. Rabalais, J.W. Eckstein, W. Subplantation model for film growth from hyperthermal species, *Phys. Rev. B*, vol. no. 41.15, May 1990, pp.10468-10480.
59. Spencer, E.G. Schnidt, P.H. Joy, D.C. Sansalone, F. Ion-bean-deposited polycrystalline diamond-like films, *Appl. Phys. Lett*, vol. no. 29.2, July 1976, pp. 118-120.
60. Moller, W. Modeling of sp^3/sp^2 ratio in ion beam and plasma-deposited carbon films, *Appl. Phys. Lett*, vol. no. 59.19, Nov. 1991, pp.2391-2393.
61. Banhart, F. Irradiation effects in carbon nanostructures, *Rep. Prog. Phys*. vol. no. 62.8, Aug. 1999, pp.1181-1221.
62. Mckenzie, F.R. Muller, D. Parlthorpe, B.A. Compressive stress-induced formation of thin-film amorphous carbon is tetrahedral. *Phys. Rev. Lett*, vol. no. 67.6, Aug. 1991, pp.773–776.
63. Mckenzie, D.R. Generation and applications of compressive stress induced by low energy ion beam bombardment, *J. Vac. Sci. Technol. B*, vol. no. 11.5, 1993, pp.1928-1935.
64. Shi, X. Tay, B.K. Tan, H.S. Li, Z. Tu, Y.Q. Properties of carbon ion deposited tetrahedral amorphous carbon films. *J. Appl. Phys*, vol. no.79.9, May 1996, pp.7234-7240.
65. Shi, X. Tu, Y.Q. Tan, H.S. Tay, B.K. Simulation of plasma flow in toroidal solenoid filters, *IEEC Trans. Plasma. Sci*, vol. no. 24.6, Dec. 1996, pp. 1309-1318.
66. Tay, B.K. You, G.F. Lau, S.P. Shi, X. Plasma flow Simulation in an off-plane double bend magnetic filter, *Surf. Coat.Tech*. vol.133-134, Nov. 2000, pp.593-597.
67. Chhowalla, M. Robertson, J. Chen, C.W. Silva, S.R.P. Amaratunga, G.A. Influence of ion energy and substrate temperature on the optical and electronic properties of tetrahedral amorphous carbon (*ta*-C) films. *J. Appl. Phys*, vol. no. 81.1, January 1997, pp.139-145.

68. Shi, X. Flynm, D. Tay, B.K. Prawer, S. Nugent, K.W. Silva, S.R.P. liffshitz, Y. Milne, W.I. Mechanical properties and Raman spectra of tetrahedral amorphous carbon films with high sp^3fraction deposited using a filtered cathodic arc. *Philos. Mag. B*, vol. no.76.3, Sept. 2006, pp.351-361.
69. Shi, X. Tay, B.K. Lau, S.P. The double bend filtered cathodic arc technology and its applications, *Int. J. Mod. Phys, B* vol.no.14.(2-3), January 2000, pp 136-153.
70. Robertson, J. The deposition mechanism of diamond-like a-C and a-C:H. *Diamond Rel. Mater*, vol. no. 3.(4-6), April 1994, pp.361-368.
71. Koidl, P. Wagner, C. Dischler, B. Wagner, J. Ramsteiner, M. Plasma deposition, Properties and structure of amorphous hydrogenated carbon films, *Mater. Sci. Forum*, vol. 52-53, 1991, pp.41-70.
72. Catherine, Y. Preparation Techniques for Diamond-Like Carbon. *Diamond and Diamond-like Films and Coatings:* NATO ASI Series, vol.266, 1991, pp.193-227.
73. Weiler, M., Sattel, S. Jung, K. Ehrhardt, H. Veerasamy. V.S. Robertson, J. Highly tetrahedral, diamond-like amorphous hydrogenated carbon prepared from a plasma beam source. *Appl. Phys. Lett*, vol. no. 64.21, May 1994, pp.2797-2799.
74. Möller, W. Plasma and surface modelling of the deposition of hydrogenated carbon films from Low-Pressure Methane Plasma. *Appl. Phys.* A, vol. no.56.6, June 1993, pp.527-546.
75. Möller W. Fukarek, W. Lange, K. Keudell, A.von, Jacob, W. Mechanisms of the deposition of hydrogenated carbon films, *Jpn. J. Appl. Phys*, vol.34, April 1995, pp. 2163-2171.
76. Mantzaris, N.V. Goloides, E. Boudouvis, A.G. Turban, G. Surface and plasma simulation of deposition processes: CH_4 plasmas for the growth of diamond-like carbon, *J. Appl. Phys*. vol. no. 79.7, April 1996, pp.3718-3729.

77. Perrin, J. Shiratani, M., Kae-Nune, P. Videlot, H. Jolly and J. Guillon, J. Surface reaction probalities and kinetics of H, SiH_3, Si_2H_5, CH_3 and C_2H_5, *J. Vac. Sci. Technol.* A, vol. no. 16.1, 1998, pp.278-289.

78. Jacob, W. Plasma chemical vapour deposition of hydrocarbon films, *Thin Solid Films*, vol. no. 326. (1-2), August 1998, pp.1-42.

79. Keudell, A.V. Jacob, W. Growth and erosion of hydrocarbon films investigated by in situ ellipsometry. *J. Appl. Phys*, vol. no.79.2, Jan.1996, pp.1092-1098.

80. Keudell, A.V. Jacob, W. Surface relaxation during plasma-enhanced chemical vapor deposition of hydrocarbon films, investigated by *in situ* ellipsometry. *J. Appl. Phys*, vol. no.81.3, 1997, pp 1531-1535.

81. Kessels, W.M.M. Gielen, J.W.A.M. van de sanden, M.C.M. van Ijzendoom, L.J. Dekempeneer E.H.A. Schram, D. C. A model for the deposition of a-C:H using an expanding thermal arc, *Surf. Coatings Technol*, vol. no. 98.(1-3), Jan.1998, pp.1584-1589.

82. Boutard, D. Moller, W. Scherzer, B.M.U. Influence of H-C bonds on the stopping power of hard and soft carbonized layers, *Phys. Rev. B*, vol. no.38.5, August 1988, pp.2988-2994.

83. Hopf, C. Schwarz-Sellinger, T. Jacob, W. von Keudell, A. Surface loss probabilities of hydrocarbon radicals on amorphous hydrogenated carbon film surfaces, *J. Appl. Phys*, vol. no.87.6, March 2000, pp.2719-2725.

84. Von Keudell, A. Schwarz-sellinger, T. Jacob, W. Simultaneous interaction of methyl radicals and atomic hydrogen with amorphous hydrogenated carbon films, *J. Appl. Phys*, vol. no.89.5, March 2001, pp.2979-2986.

85. Von Keudell, A. Schwarz-sellinger, T. Jacob, W. Novel method for absolute quantification of the flux and angular distribution of a radical source for atomic hydrogen, *J .Vac. Sci. Technol. A*, vol. no.18.3, 2000, pp.995-1001.

86. Kuppers, J. The hydrogen surface chemistry of carbon as plasma facing material surface science, *Surf. Sci. Rep*, vol. no.22.7/8, Dec. 1995, pp. 249-321.

87. Knotek, O. Löffler, F. Brand J. Hydrogen-free amorphous carbon coatings deposited by the arc ion-plating process, *Diamond. Rel. Mater*, vol. no.2.3, March 1993, pp.243-245.

88. Dresselhaus, M.S. Dresselhaus, G. Dresselhaus, G. Eklund, P.C. Science of Fullerenes and Carbon Nanotubes. Academic Press, London, 1996.

89. Robertson, J. O'Reilly, E.P. Electronic and atomic structure of amorphous carbon, *Phys. Rev. B*, vol. no.35.6, Feb.1987, pp.2946-2957.

90. Robertson, J. Electronic Structure and Bonding of a-C:H. *Mater. Sci. Forum*, vol. 52-53, 1990, pp. 125-150.

91. Robertson, J. Amorphous carbon, *Adv. Phys*, vol. no.35.4, June 2006, pp.317-374.

92. Wei, Q. Sankar, J. Sharma, A.K. Oktyabrsky, S. Narayan, J. and Narayan, R.J. Atomic structure, electrical properties, and infrared range optical properties of diamond-like carbon films containing foreign atoms prepared by pulsed laser deposition. *J. Mater. Res*., vol. no.15.3, Mar 2000, pp.633-641.

93. Lee, C.H. Lambretch, W.R.L. Segall, B. Kelires, P.C. Frauenheim, T. Stephan, U. Electronic structure of dense amorphous carbon, *Phys. Rev. B*, vol. no.49.16, April 1994, pp.11448-11451.

94. Roberston, J. Structural models of a-C and a-C:H. *Diamond Rel. Matter*. vol. no.4.4, April 1995. pp. 297-301.

95. Roberston, J. Hard amorphous (Diamond-like) carbon. Phys. Rev. B. vol. 53, 1996. pp.1594.

Prog. Solid St.Chem., 1991,vol. no.21.4, pp199-333.

96. Bewilogua, K. Dietrich, D. Holzküter, G. Weissmantel, Ch. Structure of amorphous carbon films. vol. no. 71.1, Feb 2006, pp.K57-K59.
97. Jacob, W. W. Möller, W. On the structure of thin hydrocarbon films. *Appl. Phys. Lett.*, vol. no.63.13, Sept. 1993. pp.1771-1773.
98. Knight, D.S. White, W.B. Characterization of diamond films by Raman spectroscopy, *J. Mater. Res.*, vol. no.4.2, March/April 1989, pp. 385-393.
99. Elman, B.S. Shayegan, M. Dresselhaus, M.S. Mazurek, H. Dresslhaus, G. Structural characterization of ion-implanted graphite, *Phys. Rev.* B, vol. no.25.6, March 1982, pp.4142-4156.
100. Tuinstra, F. Koening, J.L. Raman spectra of Graphite, *J. Chem. Phys.* vol. no.53.3, Aug. 1970, pp.1126-1130.
101. Ferrari, A.C. Robertson, J. Interpretation of Raman spectra of disorder and amorphous carbon, *Phys. Rev. B*, vol. no.61.20, May 2000, pp. 14095-14107.
102. Yu, P.Y. Cardona, M. Physics and Materials Properties, Fundamentals of Semiconductors. Springer. Berlin, 1996.
103. Alben. R. Weaire, D. Smith, J.E. Brodsky, M.H. Vibrational properties of elemental amorphous Si and Ge. *Phys. Rev.* B, vol. no.11.6, March 1975, pp. 2271-2296.
104. Beeman, D. Alben, R. Vibrational properties of elemental amorphous semiconductors. *Advances in Phys*, vol. no.26.3, May 1977, pp.339-361.
105. Maley, N. Lannin, J.S. Raman coupling parameter variation in amorphous germanium. *Phys. Rev.* B, vol. no.35.5, Feb. 1987, pp. 2456-2459.

106. Wada, N. Gaezi, P.J. Solin, A. “Diamond-like” 3-fold coordinated amorphous carbon. *J. Non Cryst. Solids*, vol. no.35/36.1, Jan./Feb.1980, pp.543-548.

107. Schroder, R.E. Nemanich, R.J. Glass, J.T. Analysis of the composite structures in diamond thin films by Raman spectroscopy. *Phys. Rev.* B, vol. no. 41.6, Feb 1990, pp.3738-3745.

108. Salis, S.R. Gardiner, D.J. Bowden, M. Savage, J. Rodway, D. Monitoring the quality of diamond films using Raman spectra excited at 514.5nm and 633nm. *Diamond Rel. Mater*, vol. no.5. (6-8), May 1996, pp.589-591.

109. Al-Jishi, R. Dresselhaus, G. Lattice-dynamical model for alkali-metal-graphite intercalation compounds. *Phys. Rev*. B, vol. no.26.8, Oct.1982, pp.4523-4538.

110. Mapelli, C. Castiglioni, C. Zerbi, G. Müllen K. Common force field for graphite and polycyclic aromatic hydro-carbons. *Phys. Rev*. B, vol. no.60.18, Nov. 1999, pp.12710-12725.

111. Thomsen, C. Reich, S. Double Resonant Raman scattering in graphite, *Phys. Rev. Lett*., vol. no.85.24, Dec. 2000, pp.5214-5217.

112. Chhowalla, M. Ferrari, A.C. Robertson, J. Amaratunga, G.A. Evolution of sp^2 bonding with deposition temperature in tetrahedral amorphous carbon studied by Raman spectroscopy. *Appl. Phys. Lett*, vol. no.76.11, March 2000, pp.1419-1421.

113. Ferrari, A.C., Robertson, J. Resonant Raman spectroscopy of disordered, amorphous, and diamond-like carbon, *Phys. Rev*. B, vol. no.64.7, July 2001, pp.75414-75427.

114. Tamor. M.A. Vassel, W.C. Carduner, K.R. Atomic constraint in hydrogenated diamond-like carbon. *Appl. Phys. Lett*, vol. no.58.6, Feb. 1991, pp.592-594.

115. Donnet, C. Fontaine. J. Lefbvre, F. Grill, A. Patel, V. Jahnes, C. Solid state ^{13}C and ^{1}H nuclear magnetic resonance investigations of hydrogenated amorphous carbon. *J. Appl. Phys*, vol. no.85.6, Dec.1999, pp.3264-3270.

116. Ristein, J. Stief, R.T. Ley, L. Beyer, W. A comparative analysis of a-C:H by infrared Spectroscopy and mass selected thermal effusion. *J. Appl. Phys*, vol. no.84.7, Oct. 1998, pp.3836-3847.

117. Jiang, X. Beyer, W. Reichelt, K. Gas evolution from hydrogenated amorphous carbon films. *J. Appl. Phys*, vol. no.68.3, Aug. 1990, pp.1378-1380.

118. Jacob, W. Unger, M. Experimental determination of the absorption strength of C-H vibration for infrared analysis of hydrogenated carbon films, *Appl. Phys. Lett*, vol. no.68.4, Jan. 1996, pp.475-477.

119. Harrison, W.A. Bond-orbital Model and the Properties of Tetrahedral Coordinated Solids. *Phys. Rev* B, vol. no.8.10, Nov. 1973, pp.4487-4498.

120. Coulson, C.A. Longuet-Higgins, H.C. The electronic structure of Conjugated system: General theory. *Proceedings of the Royal Society of London. Series A: Mathematical and Physical Sciences*, vol. no.191.1024, Sept. 1947, pp. 39-60.

121. Beeman, D. Silverman, J. Lynds, R. and Anderson, M.R. Modelling studies of amorphous carbon. *Phys. Rev. B*, vol. no.30.2, July 1984, pp.870-875.

122. Stillinger, F.H. and Weber, T.A. Computer simulation of local order in condensed phases of silicon. *Phys. Rev. B*, vol. no.31.8, April 1985, pp.5262-5271.

123. Tersoff, J. Ruoff, R.S. Structural properties of a carbon-nanotube crystal. *Phys. Rev. Lett*, vol. no.73.5, Aug. 1994, pp.676-679.

124. Tersoff, J. Empirical inter-atomic potential for carbon, with applications to amorphous carbon. *Phys. Rev. Lett*, vol. no.61.25, Dec. 1988, pp.2879-2882.

125. Tersoff, J. Structural properties of sp3-bonded hydrogenated amorphous carbon. *Phys. Rev. B*, vol. no.44.21, Dec 1991, pp.12039-12042.

126. Brenner. D.W. Empirical potential for hydrocarbons for use in simulating the chemical vapour deposition of diamond films. *Phys. Rev. B*, vol. no.42.15, Nov. 1990, pp.9458-9471.

127. Brenner, D.W. The Art and science of analytic potential. *Phys. Stat Solid* B, vol. no.217.1, Jan. 2000, pp.23-40.

128. Heggie, M.I. Semiclassical potential for carbon and its application to the self-interstitial in graphite. *J. Phys. Cond. Matter,* vol. no**.** 3.18 May 1991, 3065-3079

129. Kelires, P.C. Structural properties and energetic of amorphous forms of carbon. *Phys. Rev. B*, vol. no.47.4, January 1993, pp.1829-1839.

130. Kelires, P.C. Elastic properties of amorphous carbon networks. *Phys. Rev. Lett*, vol. no.73.18, Oct. 1994, pp.2460-2463.

131. Wang, C.Z. Ho, K.M. Chan, C.T. Tight-binding molecular-dynamics study of amorphous carbon. *Phys. Rev. Lett*, vol. no.70.5, Feb.1993, pp.611-614.

132. Wang, C.Z. and Ho, K.M. Structure, dynamics, and electronic properties of diamond-like amorphous carbon. *Phys. Rev. Lett*. vol. no.71.8, August 1993, pp.1184-1187.

133. Frauenheim, T. Blaudeck, P. Stephan, U. Jungnickel, G. Atomic structure and physical properties of amorphous carbon and its hydrogenated analogues. *Phys. Rev.* B, vol. no.48.7, August 1993, pp.4823-4834.

134. Schultrich, B. Siemroth, P. Scheibe, H.J. High rate deposition by vacuum arc methods. *Surf. Coatings Technol*., vol. no.93.1, Aug. 1997, pp.64-68.

135. Scheibe, H.J. Siemroth, P. The method of laser sustained arc ignition. *IEEE Trans. Plasma Sci.* vol. no.18.6, Dec.1990, pp.911-916.

136. McCulloch, D.G. McKenzie, D.R. Goringe, C.M. Ab initio simulation of the structure of amorphous carbon, *Phys. Rev. B*, vol. no.61.3, Jan.2000, pp.2349-2355.

137. Haerle, R. Riedo, E. Pasquarello, A. Baldereschi, A. sp^2/sp^3 hybridization ratio in amorphous carbon from C 1S core-level shift-principles calculation. *Phys. Rev. B*, vol. no.65.4, Dec 2001, pp.45101-45109.

138. Bilek, M.M.M. McKenzie, D.R. McCulloch, D.G. Goringe, C.M. Ab initio simulation of the structure of amorphous carbon. *Phys. Rev.* B, vol. no.62.5, August 2000, pp. 3071-3077.

139. Frauenheim, Th. Jungnickel, G. Fraunheim, Stephan, U. Blaudeck, P. Deutschmann, S. Atomic scale structure and electronic properties of highly tetrahedral hydrogenated amorphous carbon. *Phys. Rev. B*, vol. no.50.11, Sept.1994, pp.7940-7945.

140. Chen, C.W. Robertson, J. Nature of disorder and localization in amorphous Carbon. *J. Non. Cryst. Solids*, vol. no. 227/228.1, May 1998, pp.602-606.

141. Robertson, J. Recombination and photoluminescence mechanism in hydrogenated amorphous carbon. *Phys. Rev.* B, vol. no.53.24, June 1996, pp.16302-16305.

142. Oppedisano, C. Tagliaferro, A. Relationship between sp^2 carbon content and E_{04} optical gap in amorphous carbon-based materials. *Appl. Phys. Lett*., vol. no.75.23, Dec. 1999, pp.3650-3652.

143. Conways, N.M.J. Ferrari, AC. Flewitt, A.J. Robertson, J. Milne, W.I. Tagliaferro, A. Beyer, W. Defect and disorder reduction by annealing in hydrogenated tetrahedral amorphous carbon. *Diam. Rel. Mater*., vol. no.9.3-6, April-May 2000, pp.765-770.

144. Robertson, J. π–bonded clusters in amorphous carbon materials. *Philos. Mag.* B, vol. no.66.2, Aug. 2006, pp. 199-209.

145. Tamor, M.A. Vassel, W.C. Raman "fingerprinting" of amorphous carbon films. *J. Appl. Phys*., vol. no.76.6, Sept. 1994, pp.3823-3830.

146. Cheng, H.F. Chuang, F.Y. Tsai, C.H. Wang, W.C. Huang, C.M. and Lin, I.N. Boron-doping effect on the field emission behavior of pulse laser deposited diamond-like carbon films. *Applied Surface Science*, vol. no.142.1-4, April 1999, pp.504-509.

147. Clough, F.J. Milne, W.I. Kleinsorge, B. Robertson, J. Amaratunga, G.A.J. and Roy, B.N. Tetrahedrally bonded amorphous carbon (ta-C) thin film transistors. *Electronics Letters*, vol. no.32.5, Feb.1996, pp.498-499.

148. Clay, K.J. Speakman, S.P. Amaratunga, G.A.J. and Silva, S.R.P. Characterization of C:H:N deposition from CH_4/N_2 rf. Plasma using optical emission spectroscopy. J. *Appl. Phys.*, vol. no.79.9, Jan.1996, pp.7227-7233.

149. Robertson, J. and Davis, C.A. Nitrogen doping of tetrahedral amorphous carbon. *Diam. and Relat. Mat.* vol. no.4.4, April 1995, pp.441-444.

150. Chen, M.Y. and Murray, P.T. Carbon nitride thin-film growth by pulsed laser deposition. *Journal of Vacuum Science and Technology A*, vol. no.16.4, July 1998, pp.2093-2098.

151. Koizumi, S. Kamo, M. Sato, Y. Ozaki, H. Inuzuki, T. Growth and characterization of phosphorous doped {111} homo-epitaxial diamond thin films. *Appl. Phys. Lett*., vol. no.71.8, Aug. 1997, pp.1065-1067.

152. Lim, S. H. Elim, H. I. Gao, X. Y. Wee, A. T. S. Ji, W. Lee, J.Y. and Lin, J. Electronic and optical properties of nitrogen-doped multiwalled carbon nanotubes. *Phys. Rev*. B vol. no.73.4, Jan. 2006, pp. 045402(1-6).

153. Helmbold, A. Hammer, P. Thiele, J.U. Rohwer, K. and Meissner, D. Electrical conductivity of amorphous hydrogenated carbon. *Philosophical Magazine B*, vol. no.72.3, Sept. 2006, pp.335-350.

154. Golzan, M.M. McKenzie, D.R. Miller, D.J. Collocott, S.J. and Amaratunga, G.A.J. Magnetic and spin properties of tetrahedral amorphous carbon. *Diamond and Related Materials*, vol. no.4.7, May 1995, pp.912-916.

155. Hideo, Y. Takao, H. Nobutaka, T. Akio, O. Tooru, F. Shin'ichi, K. Mamoru, O. Study on Improvements of Tribological Properties of Magnesium Alloys-Diamond-Like Carbon Film Coating with the Interface Layer of Carbonaceous Film Containing Silicon. *Journal of Japanese Society of Tribologists.* vol. no.48.8, 2003, pp.667-672.

156. Robertson, J. Gap states in diamond-like amorphous carbon. *Philos. Mag. B*, vol. no.76.3, Sept. 2006, pp.335-350.

157. Ilie, A. Conway, N. Kleinsorge, B. Rattier, M. Robertson, J. And Milne, W. Photoconductivity of diamond-like carbon. *MRS proc.*, 498, 1998, pp.103-108.

158. Grill, A. Meyerson, B., in: K. Espear, Dismukes (Eds), J.P. Synthetic Diamond: Emerging CVD Science and Technology, Wiley, New York, 1994, pp.91-94.

159. Dimigen, H. Hubsch, H. Memming, R. Tribological and electrical properties of metal-containing hydrogenated carbon films. *Appl. Phys. L*ett., vol. no.50.16, April 1987, pp.1056-1058.

160. Chen, C.W. Robertson, J. Doping Mechanism in tetrahedral amorphous carbon. *Carbon*, vol. no. 37.5, April 1999, pp.839-842.

161. Cheah, L.K. Shi, X. Liu, E. Tay, B.K. Electron field emission properties of tetrahedral amorphous carbon films. *J. Appl. Phys.*, vol. no.85.9, May1999, pp. 6816-6821

162. Roberston, J. Self-compensation and the absence of doping in amorphous GaAs. *Phys. Rev. B,* vol. no.33.6, March 1986, pp.4399-4401.

163. Maeng, S.L. Uchikoga, S. Clough, F.J. Tagliaferro, A. Flewitt, A.J. Robertson, J. Milne, W.I. A carbon based bottom gate thin film transistors material. *Diamond Rel. Mater*. vol. no.9.3, April 2000, pp.805-810.

164. Dimigen, H. Hübsch, H. and Memming, R. Tribological and electrical properties of metal-containing hydrogenated carbon films. *Appl. Phys. Lett*. Vol. no.50.16, April 1987, pp.1056-1058.

165. Pethica, J. B. Hutchings, R. Oliver, W. C. Hardness measurement at penetration depths as small as 20 nm. *Philos. Mag. A*, vol. no.48.4, Sept. 2006, pp. 593-606.

166. Oliver, W.C. and Pharr, G.M. An improved technique for determining hardness and elastic modulus using load and displacement sensing indentation experiments. *J. Mater. Res*., vol. no.7.6, June 1992, pp.1564-1583.

167. Beghi, M.G. Bottani, C.E. Ossi, P.M. Lafford, T.A. Tanner, B.K. Combined surface Brillouin scattering and X-ray reflectivity characterization of thin metallic films. *J. Appl. Phys*, vol. no.81.2, Jan. 1997, pp. 672-678.

168. Tabor, D. The hardness of solids. *Rev. Phys. Technol*, vol. no.1.3, 1970, pp. 145-179.

169. Instruction Manual of the Jobin-Yvon T64000 Raman spectrograph.

170. Instruction Manual of the HP 4140B p. A Meter/D.C Voltage Source.

171. Liu, A.M. and Cohen, M. Prediction of New Low Compressibility Solids. *Science*, vol. no.245.4920, Aug. 1989, pp. 841-442.

172. Meyerson, B. and Smith, F.W. Chemical modification of the electrical properties of hydrogenated amorphous carbon films. *Solid State Comm.* vol. no.34.7, May 1980, pp. 531-534

173. Meyerson, B. and Smith, F.W. Thermopower of doped semiconducting hydrogenated amorphous carbon films. *Solid State Commun*. vol. no.41.1, Jan. 1992, pp. 23-27.

174. Jones, D. I. and Stewart, A. D. Properties of hydrogenated amorphous carbon films and the effects of doping. *Philos. Mag*. B, vol. no.46.5, Aug. 2006, pp. 423-434.

175. Amir, O. and Kalish, R. Properties of nitrogen-doped amorphous hydrogenated carbon films. *J. Appl. Phys.* Vol. no. 70.9, Nov. 1991, pp.4958-4962.

176. Mansour, A. and Ugolini, D. Photoelectron-spectroscopy study of amorphous *a*-CN_x:H. *Phys. Rev.* B, vol. no.47.16, April 1993, pp.10201-10209.

177. Helmbold, A. Hammer, P. Thiele, J. U. Rohwer, K. and Meissner, D. Electrical conductivity of amorphous hydrogenated carbon. *Philos. Mag. B*, vol. no.72.3, Sept. 1995, pp. 335-350.

178. McCann, R. Roy, S. S. Papakonstantinou, P. McLaughlin, J. A. and Ray, S.C. Spectroscopic analysis of a-C and a-CNx films prepared by ultrafast high repetition rate pulsed laser deposition. *J. Appl. Phys.* vol. no. 97.7, March 2005, pp.073522 (1-11).

179. Robertson, J. Diamond-like amorphous carbon, *Materials Science and Engineering R*, vol. no. 37.4-6, May 2002, pp. 129-281.

180. Papakonstantinou, P.and Lemoine, P. Influence of nitrogen on the structure and nanomechanical properties of pulsed laser deposited tetrahedral amorphous carbon. *J. Phys.: Condens. Matter*. vol. no.13.13, April 2001, pp. 2971-2978.

181. Merel, P. Tabbal, M. Chaker, M. Moisa, S. and Margot, J. Direct evaluation of the sp^3 content in diamond-like-carbon films by XPS. .*Appl. Surf. Sci.* vol. no.136.1-2, Oct. 1998, pp. 105-110.

182. Hellgren, N. Guo, J. Sathe, C. Agui, A. Nordgren, J. Luo, Y. Àgren, H.and Sundgren, J. Nitrogen bonding structure in carbon nitride thin films studied by soft x-ray spectroscopy. *Appl. Phys. Lett.* vol. no.79.26, Dec. 2001, pp. 4348-4350.

183. Shi, J. R. Wang, J. P. Wee, A. T. S. Yeo, C. B. Cheng, C. T. Ueda, M. Tomioka, S. and Ohsako, J. Photoelectron emission and Raman scattering studies of nitrogenated tetrahedral amorphous carbon films. *J. Appl. Phys*. vol. no.92.10, Nov. 2002, pp. 5966-5970.

184. Gilkes, K. W. R. Prawer, S. Nugent, K. W. Robertson, J. Sands, H. S. Lifshitz, Y. and Shi, X. Direct quantitative detection of the sp^3 bonding in diamond-like carbon films using ultraviolet and visible Raman spectroscopy. *J. Appl. Phys*. vol. no.87.7, May 2000, pp.7283-1289.

185. Ferrari, A. C. Rodil, S. E. and Robertson, J. Interpretation of infrared and Raman spectra of amorphous carbon nitrides. *Phys. Rev.* B, vol. no.67.15, April 2003, pp.155306-155355.

186. Das, D. Chen, K. H. Chattopadhyay, S. and Chen, L. C. Spectroscopic studies of nitrogenated amorphous carbon films prepared by ion beam sputtering. *J. Appl. Phys*. vol. no.91.8, April 2002, pp.4944-4955.

187. Bhattacharyya, S. Vallee, C. Cardinaud, C. and Turban, G. Structure of nitrogenated carbon films prepared from acetylene and nitrogen mixture in electron cyclotron resonance plasma. J. Appl. Phys. vol. no. 87.10, May 2000, pp.7524-7255.

188. Ferreira, N.G. Abramof, E. Corat, E.J. Leite, N.F. Trava-Airoldi, V.J. Stress study of HFCVD boron-doped diamond films by X-ray diffraction measurements. *Diamond Relat. Mater.* vol. no.10.3-7, March - July 2001, pp. 750-754.

189. Shi, X. Fu, H. Shi, J.R. Cheah, L.K. Tay, B.K. Hui, P. Electronic transport properties of nitrogen doped amorphous carbon films deposited by the filtered cathodic vacuum arc technique. *J. Phys. Condens. Matter*. vol. no.10.41, Oct. 1998, pp. 9293-9302.

190. Kinoshita, H. Hando T. and Yoshida, M. Preparation of electrically conductive diamond-like carbon films using *i*-C_4H_{10}/N_2 supermagnetron plasma. *J. Appl. Phys*. vol. no.**89.5**, March 2001, pp.2737-2741.

191. Dillon, R. O. Woolam, J. A. and Katkanant, V. Use of Raman scattering to investigate disorder and crystallite formation in as-deposited and annealed carbon films. *Phys. Rev. B*, vol. no.29.6, March 1984, pp. 3482-3489.